SANDIA REPORT
SAND2007-8156
Unlimited Release
Printed January 2008

Precision Electron Flow Measurements in a Disk Transmission Line

Mark Savage, Jeremy Martin, Timothy Pointon, Clifford Mendel, Daniel Jackson, Waylon Clark, Brian Stoltzfus, Michael Pelock

Prepared by
Sandia National Laboratories
Albuquerque, New Mexico 87185 and Livermore, California 94550

Sandia is a multiprogram laboratory operated by Sandia Corporation,
a Lockheed Martin Company, for the United States Department of Energy's
National Nuclear Security Administration under Contract DE-AC04-94AL85000.

Issued by Sandia National Laboratories, operated for the United States Department of Energy by Sandia Corporation.

Available to DOE and DOE contractors from
U.S. Department of Energy
Office of Scientific and Technical Information
P.O. Box 62
Oak Ridge, TN 37831

Telephone: (865) 576-8401
Facsimile: (865) 576-5728
E-Mail: reports@adonis.osti.gov
Online ordering: http://www.osti.gov/bridge

Available to the public from
U.S. Department of Commerce
National Technical Information Service
5285 Port Royal Rd.
Springfield, VA 22161

Telephone: (800) 553-6847
Facsimile: (703) 605-6900
E-Mail: orders@ntis.fedworld.gov
Online order: http://www.ntis.gov/help/ordermethods.asp?loc=7-4-0#online

SAND2007-8156
Unlimited Release
Printed January 2008

Precision Electron Flow Measurements in a Disk Transmission Line

Mark Savage, Jeremy Martin, Timothy Pointon, Clifford Mendel, Daniel Jackson, Waylon Clark, Brian Stoltzfus, Michael Pelock

Organization 1671
Sandia National Laboratories
PO Box 5800
Albuquerque, NM 87185-1194

Abstract

An analytic model for electron flow in a system driving a fixed inductive load is described and evaluated with particle in cell simulations. The simple model allows determining the impedance profile for a magnetically insulated transmission line given the minimum gap desired, and the lumped inductance inside the transition to the minimum gap. The model allows specifying the relative electron flow along the power flow direction, including cases where the fractional electron flow decreases in the power flow direction. The electrons are able to return to the cathode because they gain energy from the temporally rising magnetic field. The simulations were done with small cell size to reduce numerical heating. An experiment to compare electron flow to the simulations was done. The measured electron flow is ~33% of the value from the simulations. The discrepency is assumed to be due to a reversed electric field at the cathode because of the inductive load and falling electron drift velocity in the power flow direction. The simulations constrain the cathode electric field to zero, which gives the highest possible electron flow.

Contents

Executive summary

The understanding of magnetic insulation in pulsed power devices is a major element in the success of many pulsed power systems. Magnetic insulation has been studied for many years and the experimental, theoretical, and computational results are impressive. As the application of magnetic insulation becomes more commonplace, there are still cases where optimization would be useful. For example, in very large pulsed power machines, small reductions in inductance can save substantial amounts of money. As pulsed power driven high-current z-pinches become more successful, it is useful to evaluate recent observations of simulations and experiments.

The work described here consists of a method for defining the impedance profile of a MITL driving an inductive load. The simple model described here requires the minimum gap desired in the MITL, the radius of that minimum gap, the inductance inside the minimum gap, and a parameter that describes the desired electron flow behavior with radius. The magnitude of the flow itself changes with the applied voltage of course, but the *relative* behavior with radius can be set arbitrarily. The result of a calculation is a calculated impedance (gap) profile versus radius, out to any desired radius. This simple model ignores gap closure and assumes applied voltage well above the rest mass of an electron (511 kV). Quicksilver simulations show that at voltages over 5 megavolts, the electron flow behavior can be prescribed with an easily calculated impedance profile. The model is in some ways a more general way to consider electron flow in an ideal MITL. If, for example, one assumes that electrons cannot return to the cathode and are prevented from reaching the anode by the magnetic field, the lowest inductance configuration would be one in which the insulation condition is the same throughout the line- higher impedance regions are inductive and lower impedance regions will increase the electron flow. Such a condition is readily calculated using the model. A constant-impedance MITL impedance profile *is not* one that gives constant electron flow unless the MITL is terminated in a resistor. An inductive load does not behave as a resistor.

The measured electron flow is lower than the flow predicted by the particle in cell model. Note that the ignored (in the simulations) effect of gap closure would tend to *increase* the measured electron flow as compared to the simulations. The particle in cell model uses a zero cathode electric field condition after a field threshold is exceeded. This gives the highest electron flow (a cathode field either parallel or anti-parallel to the vacuum field would reduce the electron flow). Non-uniform electron emission would cause an average cathode field to be non-zero and parallel to the anode electric field. Excess electron charge (electrons unable to return to the cathode) would create a cathode electric field anti-parallel to the anode field. Either one of these cases would result in less electron flow than zero cathode electric field. With the graphite suspension applied to the cathode surface (which lowers the threshold for cathode plasma formation) and the measured electron current lower than zero-cathode-field simulations, it is suspected that the electric field near the cathode is non-zero and actually reversed compared to the anode field.

This project also included building an experiment that would test experimentally the MITL design procedure. The relatively low voltage in the experiment (~500 kV) made the space charge correction voltage comparable to the line voltage, which was not considered in the analytic model. The electron flow did qualitatively behave as designed even at low voltage. The experimentally measured electron currents were below those calculated by the particle in cell model. This could be due to an electric field on the cathode, which the simulation model employed here constrains to zero. Zero cathode field will produce the highest possible electron flow. If the cathode field is reversed (compared to the vacuum field) there is more electron space charge in the line than is required to shield the cathode. The reversed field drives the $E \times B$ drift in the direction against the bulk power flow, reducing the net flow current. If the cathode field is the same direction as the applied electric field, the total number of electrons is less, and the electron current is subsequently lowered.

In the experiment, a concept for an electron collector system that would allow direct electron current measurement, instead of the more usual subtraction of cathode current from anode current, was tested. Mechanical alignment problems and pulser problems limited the amount of data available, but the existing data show that such a collector can work and provide more accurate measurements of flow in some situations.

The simulations included the current-measuring probe grooves. The simulation and experimental results show that a groove on the cathode of a MITL quickly fills with electrons and is non-perturbing to the system. This is important for large systems that have joints between pieces, grooves for monitors, or other features on the cathode.

Acronyms

MITL- magnetically insulated transmission line

PIC- particle-in-cell model of plasma systems

RC-integrator- passive device for integrating derivative signals with respect to time

Bdot- derivative responding flux meter for measuring current

Electron flow in z-pinch drivers

Magnetic insulation is vital for large pulsed power drivers, and has been studied in terms of behavior [1-8], stability[9-13], and application[2, 3, 14-37]. In a magnetically insulated system, the self-magnetic field of transmission line current inhibits electron current loss to the anode, even though the cathode conductor freely emits electrons above about 20 kV/mm. The suppression of electron loss allows building drivers that operate at 200 kV/mm or more. There is a considerable theoretical and computational basis for understanding the electron flow in such systems. Of particular interest are high current pulsers for z-pinch driven high energy density physics experiments. Such drivers are directly affected by electron flow behavior, because electron flow and the subsequent localized energy deposition largely sets the vacuum inductance of pulsed power drivers; vacuum inductance in turn largely determines the load energy efficiency. While there is good understanding of the flowing electrons, the particle-in-cell calculations that are used to model actual systems have fundamental difficulties with the electron flow in most z-pinch drivers. This is because of the thin (compared to the vacuum gap) electron sheaths at times near peak current. The thin sheaths require small cell sizes, which makes the calculations more computer-intensive. Inadequate resolution tends to cause energy increase to the electrons (numerical heating); small energy errors can significantly change the calculated electron behavior because the electrons are very close to the cathode for much of the times of interest. This project intends to make detailed measurements of electron flow in a low-impedance, high current disk transmission line. This system will be relevant to pulsed power systems driving low impedance loads, such as z-pinches. Such measurements have not been done in this geometry before, and accurate data are vital for benchmarking the widely used simulation techniques. Verification of algorithms is important as driver designs rely more on simulations to optimize large machines.

If electrons could never return to the cathode, the model used here would not be practical, except for the special case of constant electron flow. However, there is evidence based on simulations [22, 38] and experiments [17, 21, 30] that electrons might return to the cathode, at least under some conditions.

An experiment was fielded to study electron flow in a low impedance system driving an inductive load. For z-pinch systems, the load acts as a fixed inductor for the initial part of the drive pulse. This is desirable for efficiency; the load power must be higher to drive the pinch after it starts to move. The electron flow is important early in the pulse because the voltage is highest and the current is lowest at early times. Also, gas desorbed by the electrons striking the anode is more important early in the pulse since it has more time to expand if it's desorbed early in the pulse. For these reasons, we considered it a reasonable approximation to model a z-pinch system as a fixed inductor for electron flow considerations. There can be considerable electron flow as the z-pinch changes its inductance late in the implosion process, but at that time current is relatively high and the time for secondary plasma to affect the power is reduced.

Calculations

The desired outcome of the present work is to develop a systematic method for design of magnetically insulated transmission lines (MITL) for strongly insulated systems. The design of a MITL system is generally dictated by numerous concerns, many of them conflicting. For example, low inductance is generally desired to allow the most efficient delivery of energy from the driver to the load. This however generally increases the current flowing in electrons because lower impedance transmission lines have higher electric field. The electron current can cause anode plasma desorption if deposited in small areas, heating the anode metal [39]. MITL electrode gaps may be limited at small diameters by mechanical alignment limits or electrode plasma concerns.

The calculations below (in a radial disk geometry) describe a manner for calculating the MITL gaps given common parameters. The required parameters are the minimum gap, the radius of the minimum gap, the inductance inside the minimum gap radius, and the desired variation of electron current with radius. The variation of electron current with radius assumes that electrons are able to return to the cathode. For electrons to be able to return to the cathode, betatron acceleration (electron energy increase due to increasing magnetic field) must be at least as high as the rate of electron energy loss. Electrons can lose energy, for example, by synchrotron radiation, and collisions [40]. Classical collisions between electrons and gas ions are small in rate, and especially small in number for the tens of nanosecond pulses typical in present z-pinch drivers. Stygar has developed a model for magnetically insulated flow in cases where electrons lose energy due to electromagnetic field fluctuations [40].

The synchrotron energy loss rate can be calculated from the classical Larmor equation since the drifting electrons travel much slower than the speed of light [6]. The synchrotron power is

$$S = \frac{e^2}{6\pi\varepsilon_0 m_0 c^3}\left(\frac{dP}{dt}\right)^2 \tag{1}$$

where S is the radiated power, e is the electron charge, m_0 is the electron rest mass, ε_0 is the permittivity of space, c is the speed of light, and P is the electron momentum. For a particle gyrating in crossed electric and magnetic fields,

$$\frac{dP}{dt} = eE \tag{2}$$

where E is the electric field.

The energy loss to synchrotron radiation is

$$S = \frac{e^4}{6\pi\varepsilon_0 m_0^2 c^3}E^2 \tag{3}$$

which is $1.7 \cdot 10^{-15}$ Watts for each electron at 1 MV/cm. This is 10.5 keV/s, or $420 \cdot 10^{-6}$ eV over a 40 ns power pulse for each electron. This is negligible compared to the electron kinetic energy in typical systems.

Betatron acceleration is due to the changing magnetic field [41]. While current is rising, the electrons gain kinetic energy from the magnetic field. While current is falling, the electrons give energy to the magnetic field. For electrons drifting along the cathode at an average height h, the changing flux per unit length (induction) is

$$V_\beta = h\frac{\dot{I}\mu_0}{2\pi r} \tag{4}$$

where $\dot{I}$ is the time derivative of current, and r is the radius. For typical values in the experiment and simulations done here, $\dot{I}$ is about 10^{13} A/s until times close to peak current. At 0.2 m radius, an electron 1 mm average height above the cathode gains 100 electron volts per cm of drift. Electrons continually gaining total energy will return to the cathode [12]. Particle in cell simulation models don't typically have models for radiation or collisions, but magnetic induction is of course modeled self-consistently.

Because there is a mechanism for electrons to return to the cathode under some conditions, and because observations from particle modeling of magnetically insulated transmission lines [38] shows that the local electron flow tends to operate at the locally calculated value [26, 28] prompted a study to attempt exploiting that condition to design impedance profiles for MITLs. Impedance profiles for MITLs in large z-pinch drivers determine the inductance (which in turn affects total efficiency) of those drivers [42], and so can have appreciable cost implications. To the extent that electron flow is a primary consideration in large driver design, it would be useful to have tools to help constrain the mechanical design based on electron flow issues.

The model

The simple time-independent model of a magnetically insulated transmission line driving a low impedance load is shown in Figure 1.

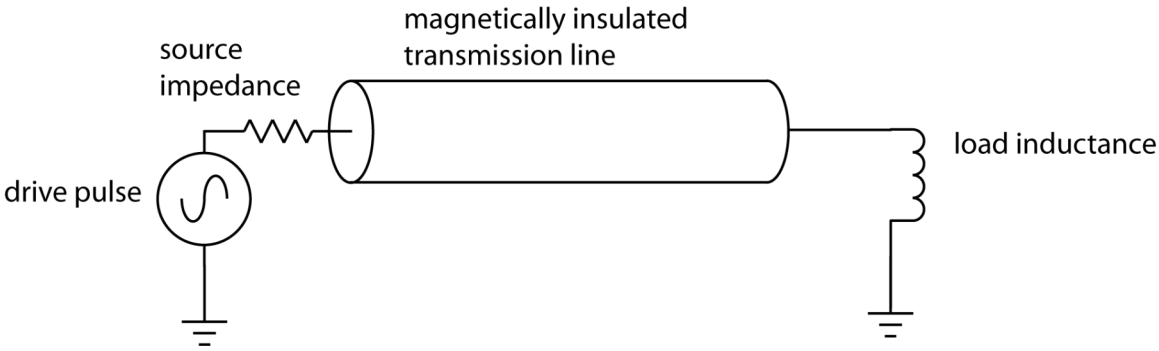

Figure 1. A simple model of a pulser and magnetically insulated transmission line driving a low impedance load. The load inductance is assumed to be unchanging. The magnetically insulated transmission line has a short transit time compared to the pulse length.

In the typical radial disk geometry, Figure 2 conceptually shows the magnetically insulated transmission line (MITL) system. Note that Figure 2 shows a radial disk feed transmission line, but the calculations to follow apply equally well to any inductive load with geometric corrections. At times before peak current, magnetic energy is flowing towards the load inductor. The radial location r_0 is the radius at which the gap becomes the minimum allowed (g_0); the vacuum impedance is minimum at the radius r_0. The impedance rises at smaller radius in a constant-gap configuration. The electron flow generally will become unstable near the point that the vacuum impedance starts to rise abruptly in the power flow direction. A key issue is the maximum *stable* change rate in equilibrium flow. It is known that the abrupt transition in the load region shown in Figure 2 will cause electron instability. We will consider all the inductance downstream of r_0 to be lumped together into the load inductance value L_0.

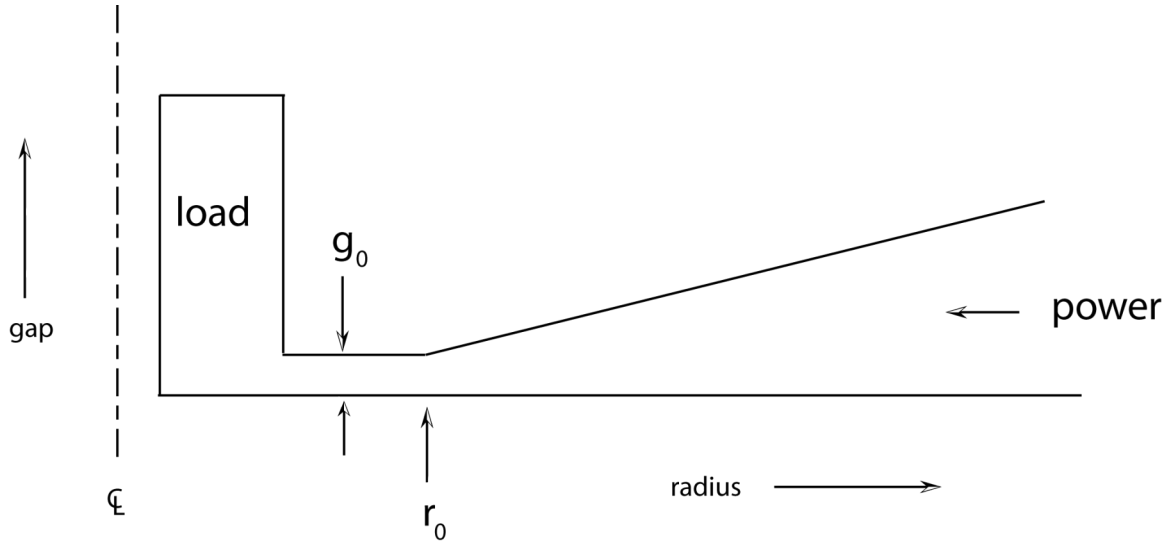

Figure 2. Schematic of the magnetically insulated transmission line and load profile.

The local electron flow current magnitude is readily calculated from analytic theory using [28]. In those calculations, for voltages above about 500 kV, the electron current is

$$V = Z\left(I_a^2 - I_c^2\right)^{\frac{1}{2}} - \frac{m_e c^2}{2e}\left(\left(\frac{I_a}{I_c}\right)^2 - 1\right) \tag{5}$$

where V is the potential difference between the anode and cathode, Z is the vacuum wave impedance, I_a is the anode current, I_c is the cathode current, m_e is the electron mass, and e is the electron charge. In situations where the electron current is much less than the anode current, a reasonable approximation to (5) is

$$I_e \approx \frac{V^2}{2I_a Z^2} \tag{6}$$

where I_e is the current in vacuum-flowing electrons. The voltage at a radial position is determined from the total inductance at that radius and the rate of change of current.

$$V = L(r)\dot{I}_a \tag{7}$$

where $L(r)$ is the total inductance inside the radius r and $\dot{I}_a$ is the time-derivative of the anode current. The inductance at a radial location is the sum of the lumped load inductance and the transmission line equivalent lumped inductance

$$L(r) = L_0 + \frac{1}{c}\int_{r_0}^{r} Z dr' \tag{8}$$

where c is the speed of electromagnetic waves in vacuum.

It is convenient to use inductance rather than impedance throughout. Define inductance (λ) and its derivatives with respect to radius (λ', λ'') as below

$$\begin{aligned} \lambda &= L_0 + \frac{1}{c}\int_{r_0}^{r} Z dr' \\ \lambda' &= \frac{Z}{c} \\ \lambda'' &= \frac{Z'}{c} \end{aligned} \tag{9}$$

The voltage as a function of radius is

$$V(r) = \dot{I}_a \lambda\,. \tag{10}$$

The electron flow as a function of radius is then

$$I_e(r) \approx \frac{\left(\dot{I}_a\right)^2}{2I_a}\frac{\lambda^2}{c^2\lambda'^2}\,. \tag{11}$$

Define $\chi = \dfrac{\left(\dot{I}_a\right)^2}{2I_a c^2}$, so that

$$I_e = \chi\left[\frac{\lambda}{\lambda'}\right]^2. \tag{12}$$

The voltage (if non-zero) changes with radial position. The change in electron flow current with radius is

$$\frac{\partial I_e}{\partial r} = 2\chi\left[\frac{\lambda}{\lambda'} - \frac{\lambda^2\lambda''}{\lambda'^3}\right]. \tag{13}$$

The fractional change in electron current with radius is defined as

$$\begin{aligned}\beta &= \frac{1}{I_e}\frac{\partial I_e}{\partial r} \\ &= 2\chi\left[\frac{\lambda}{\lambda'} - \frac{\lambda^2\lambda''}{\lambda'^3}\right]\frac{1}{\chi}\left[\frac{\lambda'}{\lambda}\right]^2\end{aligned} \tag{14}$$

so that the fractional change in electron flow with radius then becomes simply

$$\beta = 2\frac{\lambda'^2 - \lambda''\lambda}{\lambda\lambda'}. \tag{15}$$

If electron flow into the load is a constraint, and electrons do not reach the anode or return to the cathode, then the lowest inductance case must be constant electron flow over the radial extent. This is $\beta = 0$, or

$$\lambda'^2 = \lambda''\lambda. \tag{16}$$

This is solved by

$$\lambda = \lambda_0 \exp\left[\frac{r - r_0}{\gamma}\right] \tag{17}$$

where γ is a constant. To find γ, use the impedance at $r = r_0$:

$$\begin{aligned} \lambda' &= \frac{Z}{c} \\ \frac{\lambda_0}{\gamma} &= \frac{Z(r_0)}{c} \\ \gamma &= \frac{\lambda_0 c}{Z(r_0)} \\ &= \frac{L_0 c r_0}{60 g_0} \end{aligned} . \tag{18}$$

For constant electron flow versus radius, the impedance profile is

$$\begin{aligned} Z(r_0) &= \frac{c\lambda_0}{\gamma} \\ Z(r) &= \frac{c\lambda_0}{\gamma} \exp\left[\frac{r - r_0}{\gamma}\right] \end{aligned} \tag{19}$$

With the constants in (19), the impedance profile solution for constant electron flow is

$$Z(r) = \frac{60 g_0}{r_0} \exp\left[\frac{(r - r_0) g_0 60}{L_0 r_0 c}\right]. \tag{20}$$

For non-constant electron flow, we solve (15) numerically, although analytic solutions for a given value of β are possible. We have three sets of hardware designed- one calculated for constant electron flow versus radius, the other two designed to have appreciable change (β=1 and 3.7) in electron flow versus radius.

We replaced the magnetically insulated transmission line hardware on Tesla with the disk feed. The new hardware has four sets of anode and cathode current monitors, in addition to a load region electron collector. The collector is designed to exploit the electron turbulence in the increasing vacuum impedance of the load region. The collector has a separate floating electrode that encloses about 97% of the load inductance flux volume. Because this encloses essentially all of the load inductance flux, this additional electrode looks to a flowing electron like the anode surface. Simulations and experiments show that electrons reach the anode due to instabilities in an abrupt impedance transition. Briefly put, the mean electron drift velocity slows at an impedance increase because of the reduced electric field. Electrons must go to the collector can walls and do so by building up space charge to create enough electric field to allow crossing the magnetic flux to reach the anode.

Mechanical design

Functioning of the electron collector (verified by agreement with calculations and with the conventional current monitors) would allow an experiment on Saturn or Z to

directly measure the electron flow into the post-hole convolute region. For this reason, we consider the electron collector an important part of the proposal, and design work to make it reliable has been appreciable. Figure 3 shows the design of the MITL and electron collector hardware.

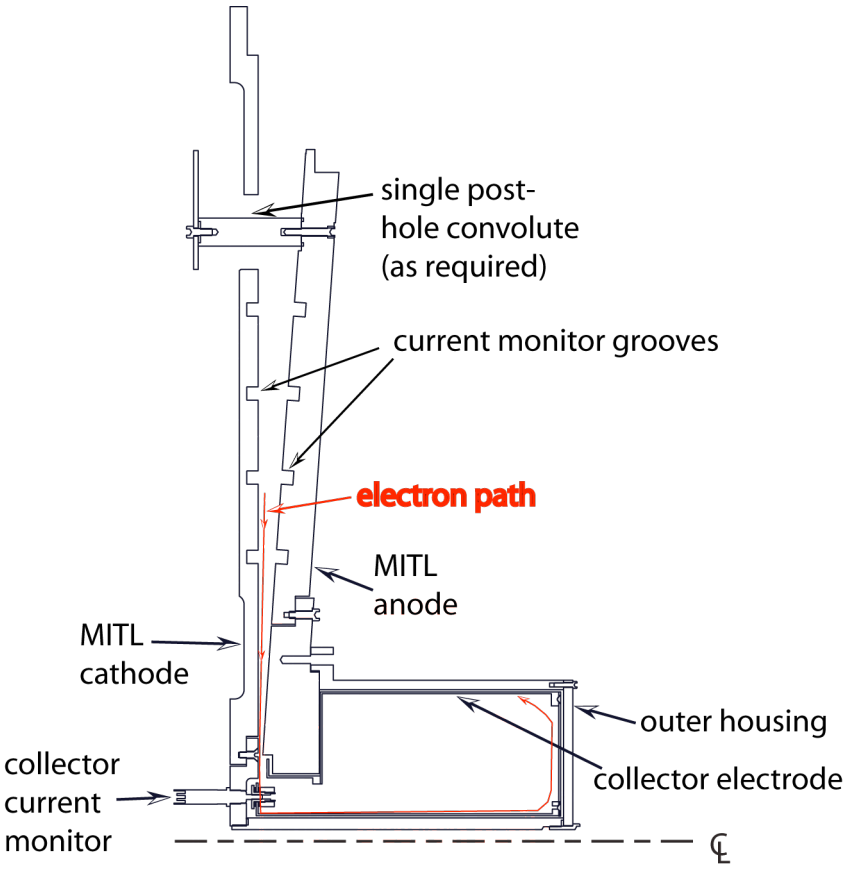

Figure 3. The disk MITL and electron collector design. The cathode outer radius is 0.56 meters. The pulser feed is double sided; convolute posts allow feeding energy from both sides of the oil-vacuum insulator if desired.

The calculated gaps for a constant electron current versus radius and for decreasing ($\beta = 1$) cases are shown in Figure 4. The calculated electron flow in Figure 4 comes from an evaluation of (5), and not the approximation of electron flow in (6). Both cases used an experimentally measured forward wave from the driver, and a calculated current and voltage from the forward wave, the source impedance, and the computed inductance. Such a calculation has excellent agreement with measured voltages and currents on Z and a variety of other experiments.

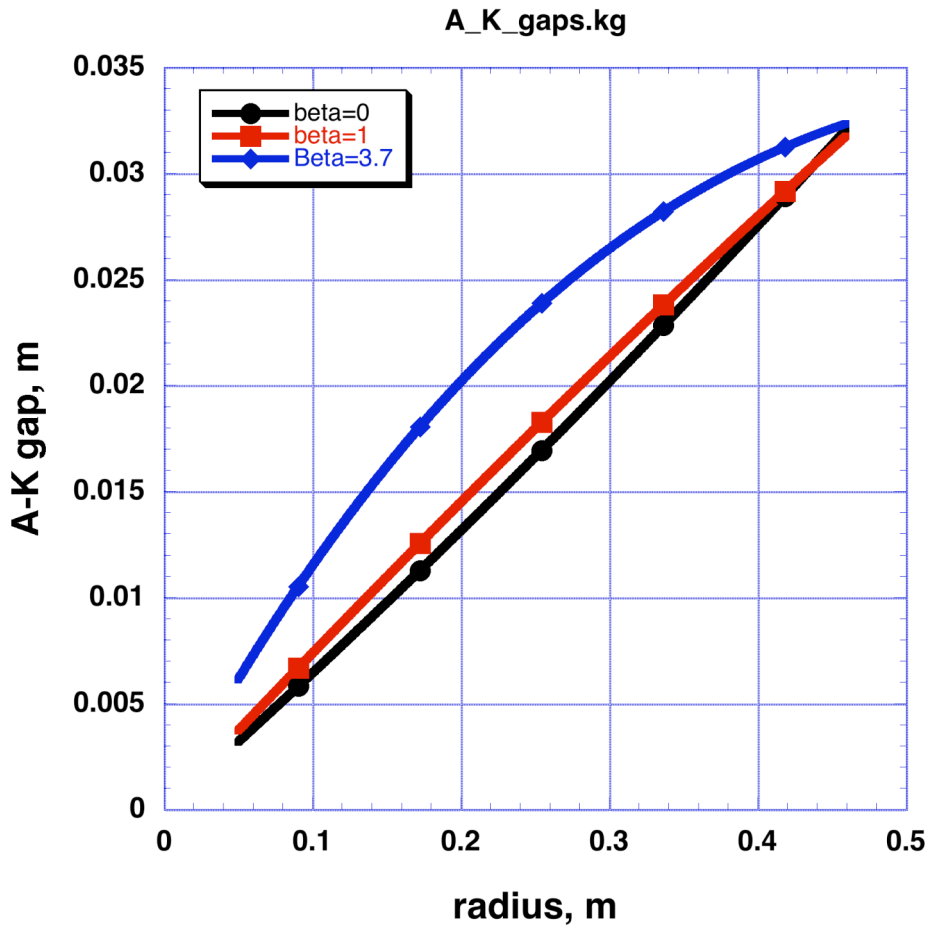

Figure 4. Calculated gap profiles for constant electron flow (beta=0), reducing flow (beta=1) and reducing flow (beta=3.7). These calculations constrained the gap at the outer part of the MITLs to be the same for the three beta values considered.

The feed inductances from the calculations in Figure 4 are 9.08 nH for the constant flow current geometry and 4.95 nH for the beta=1 reducing flow geometry, and 6.41 for the beta=3.7 reducing flow geometry. Figure 5 shows the calculated voltages and currents for the two geometries. Note that the total inductance is not changed significantly and so the feed voltages and current are essentially the same. The electron flow at the outer radius is the same as well since the gap, the voltage, and the currents are about the same. The difference is the electron flow at small radius.

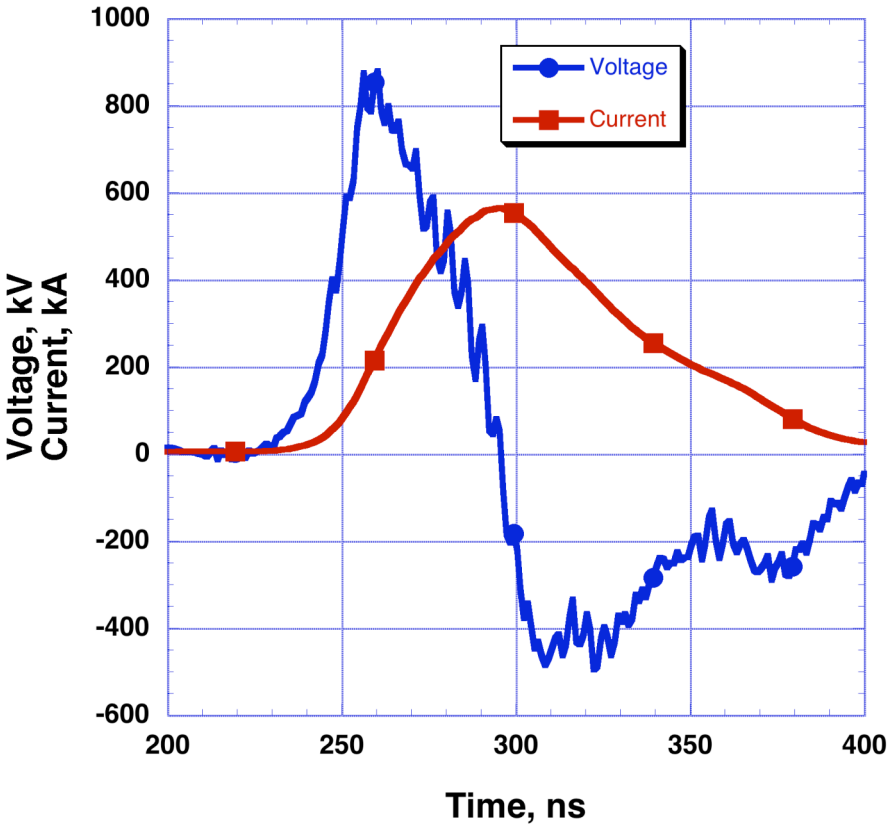

Figure 5. Voltage and total current for the disk MITL geometry. The calculation takes the measured forward-going waveform from the pulsed power driver, and calculates the voltage and current from an analytic model of the circuit.

The system is modeled with a known experimental forward-going waveform and the known source impedance of the pulsed power driver. The current in the (fixed) inductor is

$$i = \frac{2}{L}\exp\left[\frac{-R\tau}{L}\right]\int_{-\infty}^{t} V_{forward}\exp\left[\frac{r\tau}{L}\right]d\tau \tag{21}$$

where i is the inductor current, R is the driver impedance, $V_{forward}$ is the forward wave, and L is the inductance. This neglects displacement current (transit time effects) in the inductor. This allows simple analytic evaluation of current in the load inductor. The inductor voltage can be calculated in the same manner as the current;

$$i = 2V_{forward} - \frac{2R}{L}\exp\left[\frac{-R\tau}{L}\right]\int_{-\infty}^{t} V_{forward}\exp\left[\frac{r\tau}{L}\right]d\tau\,, \tag{22}$$

where v is the voltage. Using the current and voltage calculated in the preceding manner, it is straightforward to calculate electron flow in a created geometry. Code was written to generate MITL profiles given the minimum gap, the radius of the transition to minimum gap, the inductance inside the minimum gap, the outer radius, and the electron retrapping parameter as shown in Figure 4. Figure 5 shows typical voltage calculated from the measured forward wave and given inductance and gap profile parameters. Figure 7 shows electron flow calculated at different radii in a gap profile designed for constant flow versus radius. The calculated electron flows in Figure 6 and Figure 7 neglect transit time effects, and assume zero threshold for the cathode to become a space-charge limited source of electrons.

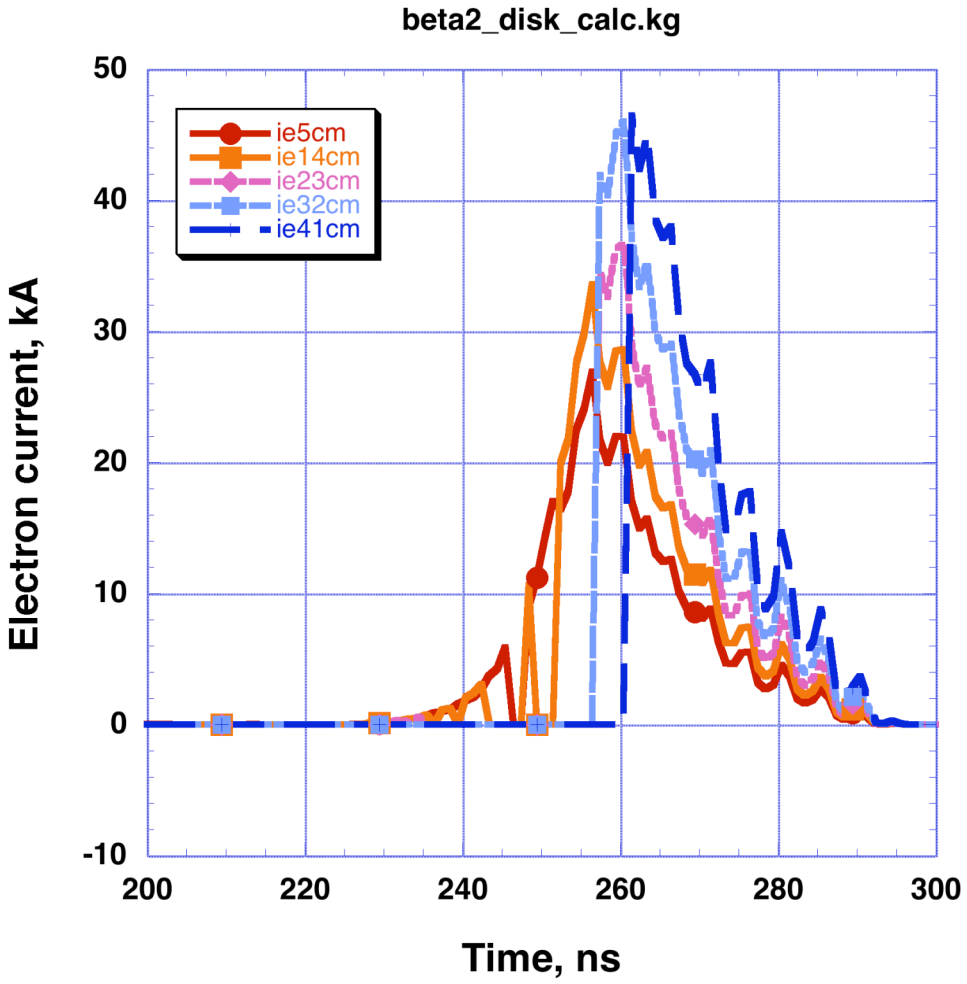

Figure 6. Calculated electron flow for 43 nH lumped central inductance and a gap profile designed to have a reducing electron flow with smaller radius.

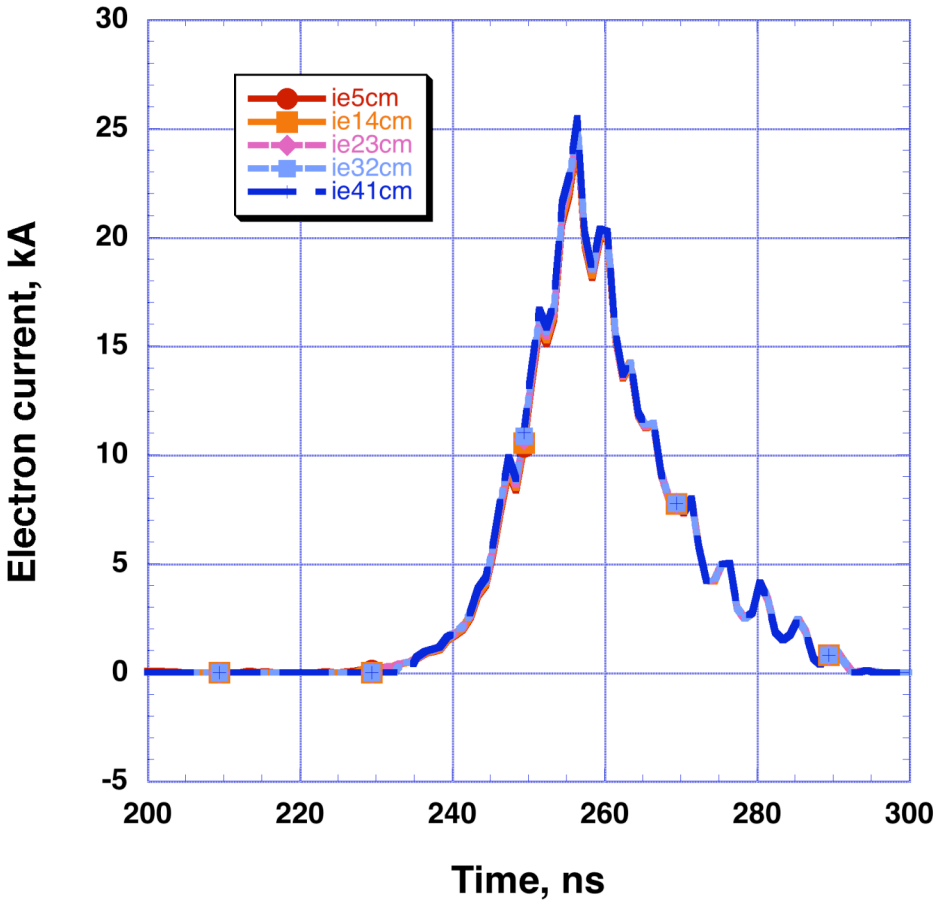

Figure 7. Electron flow calculated from the analytic form at different radii for a constant-flow profile, at a voltage over 1 MV. The electron flow current calculations overlay, as they should.

The time up to peak current is the most interesting in terms of delivering magnetic energy to the z-pinch. While current is rising, electrons gain energy from the rising magnetic field. Since the electrons gain energy, it is possible for them to return to the cathode if the charge density is high enough to maintain the space-charge limited (zero cathode electric field) condition. The model does not account for plasma on the cathode surface or gap closure. For short enough pulses, or large enough conductor spacing, the neglect of gap closure may be appropriate.

There is a substantial inductance reduction if electrons gain enough energy to return to the cathode and higher flow at large radius is acceptable. Note that the design here use a relatively large load inductance to enhance the flow current to levels that can be more easily measured with the anode and cathode current monitors. As the inductance of the load becomes higher, the variations with radius will be less. This is because the voltage variations along the radial feed line become less important.

The experimental configuration

The experiments were conducted on a relatively small pulsed power at Sandia National Laboratories. This driver can deliver 500- to 800- kV peak forward waves with ~30 ns full width at half-maximum. Figure 12 shows the driver. The driver consists of a 24-stage Marx generator charged to ~60 kV, which upon erection charges two 7.5 nF water capacitors in ~500 ns. The water capacitors are discharged by an electrically triggered gas switch into four water-insulated pulse-forming lines. The water-insulated pulse-forming lines are discharged by self-closing water switches. The energy flows past the self-closing water switches to charge four water-insulated pulse-forming lines. These lines have a second set of water switches for pre-pulse suppression. The system has a ~2Ω source impedance. The current risetime into an inductor is ~40 ns. The power from the water insulated lines flows through oil-water polyurethane barriers, and into the vacuum insulator stack region. This region is filled with transformer oil. The vacuum insulator stack itself is a balanced (ground-high voltage-ground) design. This experiment uses only one side of the insulator stack. The inductance between the water-insulated lines and the vacuum region is 10 nH. Using both sides of the insulator stack would reduce the inductance to 5 nH, but would require a vacuum convolute to add the currents into a common feed. Such a convolute is possible with this hardware but was not used because of the complication associated with power flow past a region with magnetic nulls. Future work should include tests with a convolute, if only to assess whether a region with magnetic nulls affects electron flow downstream. It is possible that the weakly-insulated regions around the nulls (which effectively have a very low impedance since impedance is a function of $\sqrt{\frac{E_{magnetic}}{E_{capacitive}}}$, where $E_{magnetic}$ is the local energy stored in magnetic field, and $E_{capacitive}$ is the local energy stored in electric field. Near a magnetic null, of course, the magnetic energy is very small and so the effective impedance is small. A region of low impedance could enhance the electron flow [24].

The electron current is diagnosed with conventional derivative-responding fluxmeter 'Bdots'. To avoid issues with magnetic flux penetration into metal surrounding Bdots in holes, the Bdots here are in grooves. The Bdot active loop is etched onto standard printed circuit board. The Bdot loops are photo-etched, and have calibration constants within two percent. Twelve monitors are on the anode, and twelve on the cathode. The monitors are at the same radial distances from the center, but the anode loops are staggered in azimuth by ten degrees.

The monitors were calibrated in place with a 40 ns risetime, 3 kV pulser connected via coaxial cables to the water lines. Figure 8 shows a view of the Bdot monitor.

The calibration factor for the Bdots is within 5% of the value expected from the nominal loop dimensions. The monitors were calibrated against a .005Ω current viewing resistor in the center of the disk MITL hardware. This monitor was only used for the calibrations. The average relative standard deviations (rms deviation over all waveform points divided by the peak) of the waveform comparisons between the Bdot and the reference resistor was 0.4%. The comparison was actually done between the integrated current viewing resistor signal and the Bdot signals integrated twice. This was necessary to improve the accuracy of the comparisons because of the small but noticeable displacement current flowing in the transmission line. The transit time of the disk MITL

hardware is 1.7 ns. Compared to the 40 ns calibration pulser risetime the transit time is small but enough to cause a noticeable difference between the outer Bdots and the reference monitor on the center of the MITL disks.

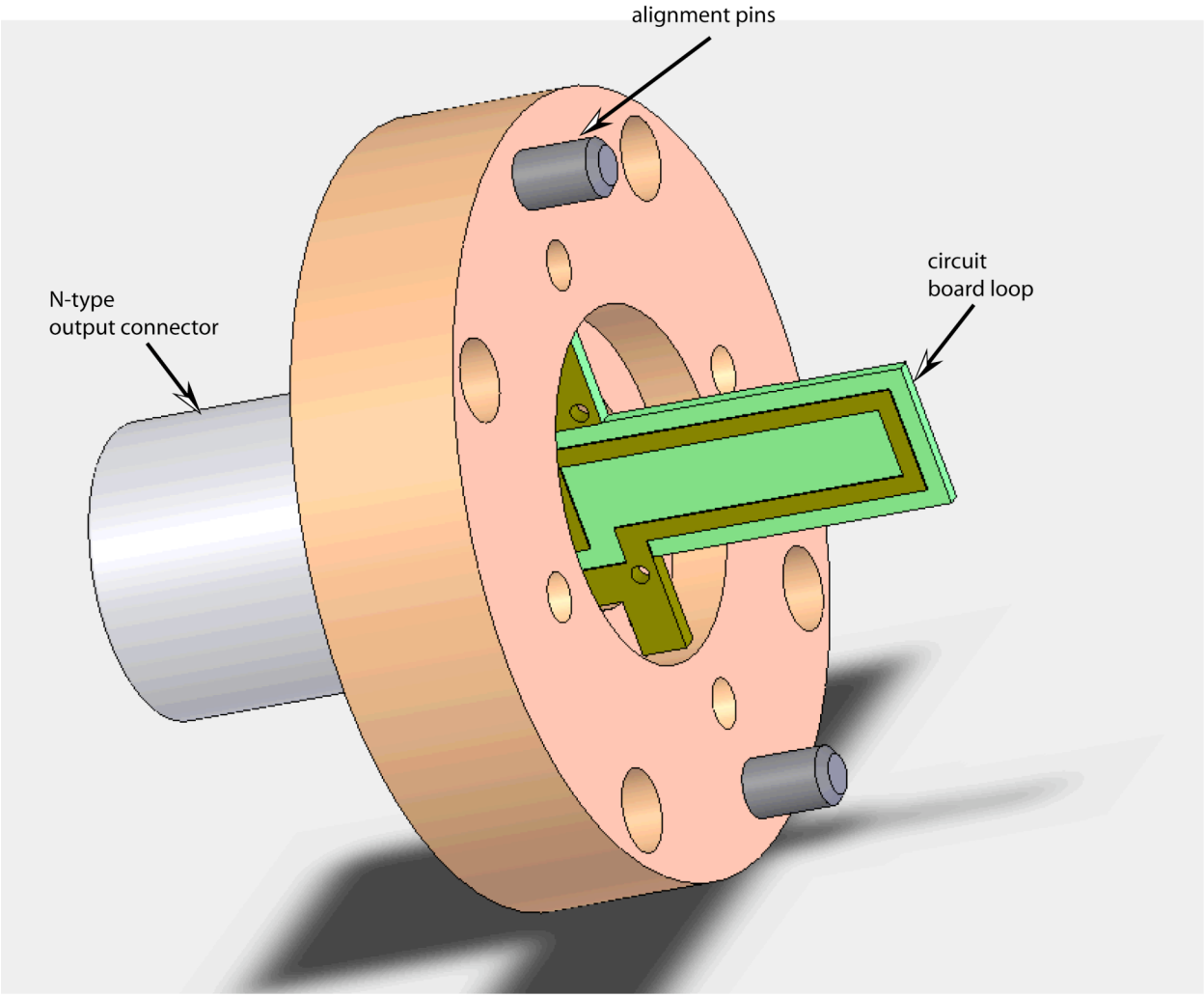

Figure 8. The Bdot monitor used on the disk MITL hardware.

The calibration factors varied by about 0.4% (one-sigma) over tens of calibration tests. The average factor from all the tests was used for the Bdots. Figure 11 shows calibration factors for three Bdots over a calibration set. All the gauge factors on one monitor are averaged and applied to that monitors. The Bdots were calibrated on the digitizer channel on which the shot data were acquired. The digitizers used were Tektronix TDS654C and TDS684C digitizers acquiring at 200 ps/point. The accuracy of the digitizers is expected to be 7 seven bits. The timing accuracy of the channels (triggered from a common fast-rise trigger pulser) is expected to be $\frac{\tau_{sample}}{\sqrt{2}}$, where τ_{sample} is the sample time. A test showed 145 ps (one-sigma) deviation between units sampling

at 200 ps. The bandwidth of the TDS654C is 500 MHz; the TDS684 bandwidth is 1 GHz. The cable runs from the monitors to the digitizers are identical; 5.5 m of RG-142, 7.6 m of half0inch Heliax, and 3.6 m of quarter-inch Heliax. The 10-90 risetime of the cable system is 900 ps.

The signals are acquired in a quadruple-shielded screen box with copper sheet and steel sheet walls for fast and slow magnetic field penetration resistance. The noise level inside the screen box during a shot is well below one millivolt. Figure 11 shows the screen box.

Low inductance passive (RC) integrators were used to integrate the signals. The integrators allow accurate response at the one-nanosecond timescale. The integrators also attenuate the signals (the integrator time constants was ~2.3 μs) so attenuators were not needed. The integrators were calibrated as described in the Appendix to about 0.5% accuracy in time constant. This time constant was applied to the calibration gauge factors (calibration was done without integrators by numerically integrating the derivative signals). The average integrator time constant value was used in a droop-correction routine, also described in the Appendix. The droop was of order 2% at the end of the voltage pulse. Figure 11 shows a picture of the integrators inside the screen box.

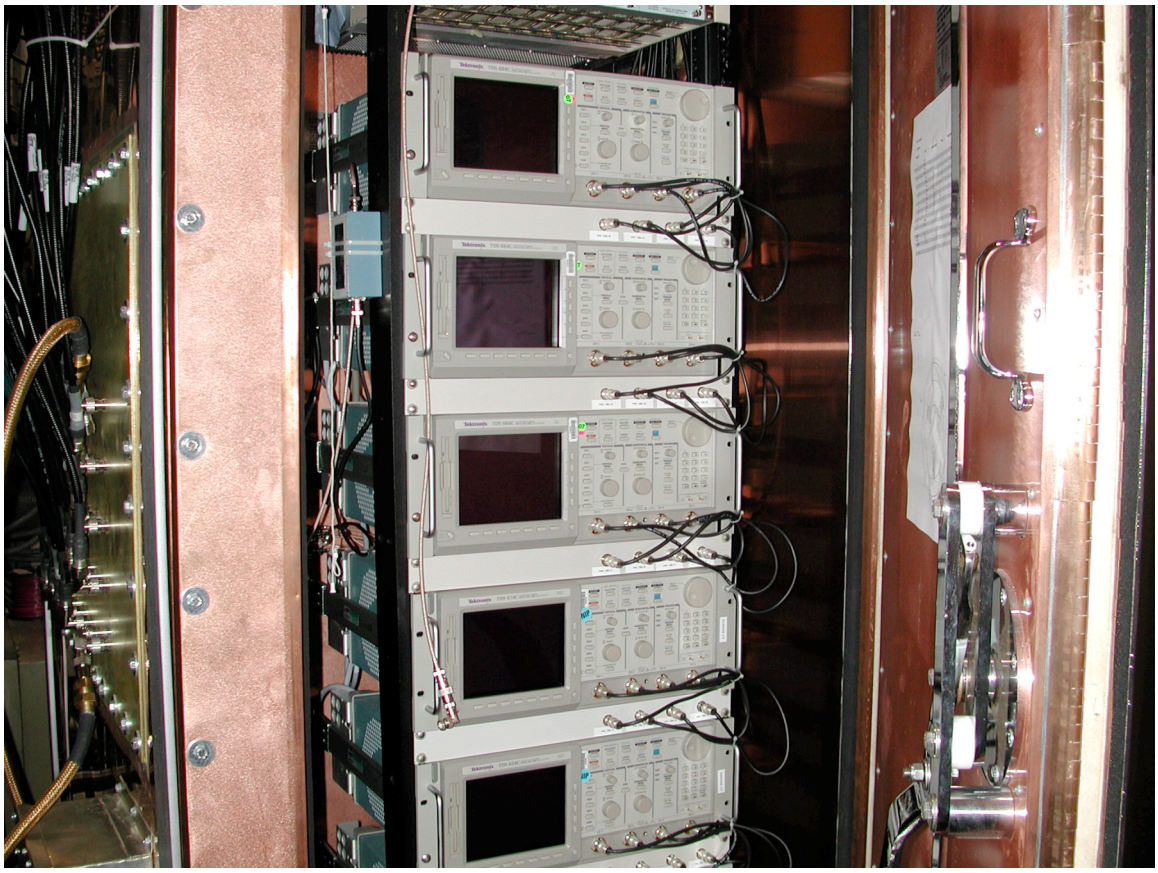

Figure 9. Screen box holding seven digitizers for acquiring 28 signals.

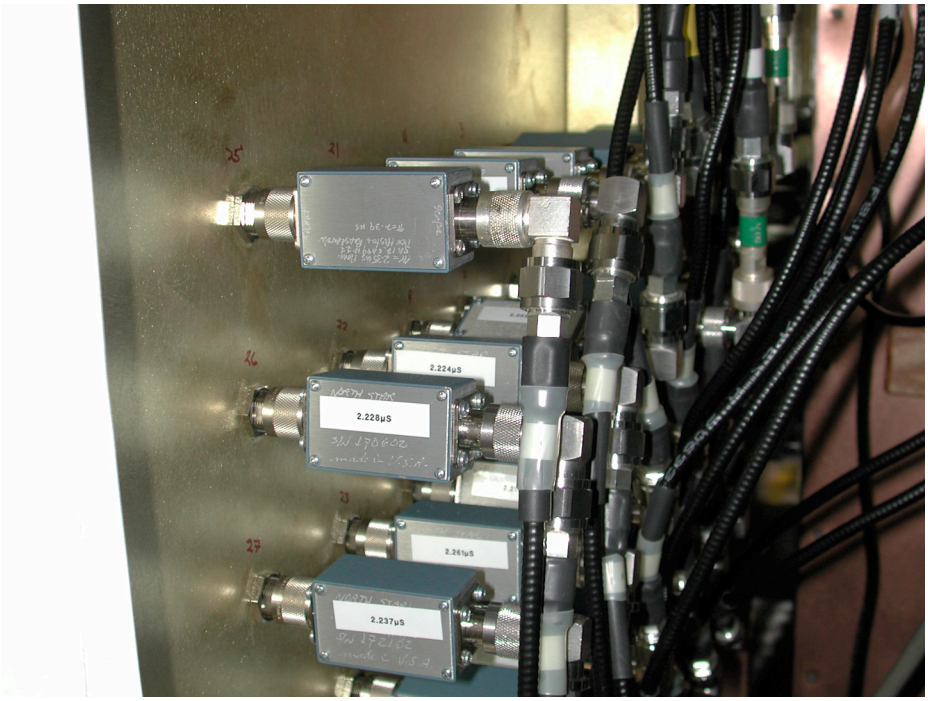

Figure 10. Passive integrators inside the screen box.

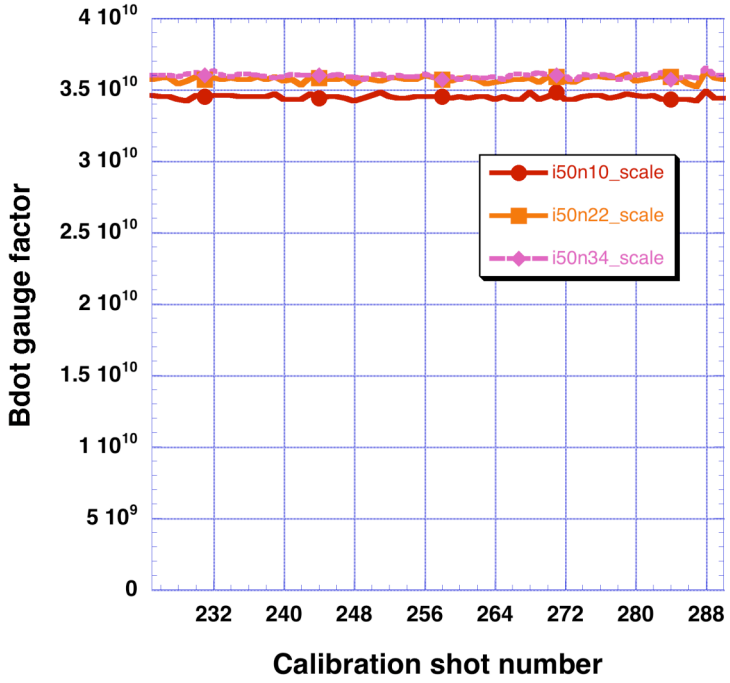

Figure 11. Calibration factors for three individual Bdots over a number of calibration tests. The relative standard deviation of the individual fits and the relative standard deviation of the gauge factors over the shots is about 0.4% (one-sigma).

Figure 12 shows a view of the pulsed power driver on which the experiment was conducted. Figure 13 shows a cross-sectional view of the disk MITL hardware tested. Figure 14 shows a picture of the MITL cathode. Figure 15 shows the center region of the MITL hardware and the electron collector. The electron collector was designed to be a complete can inside the outer central inductor. Mechanical tolerances made it difficult to maintain alignment with the entire collector can. A partial can still measures electron current, though the collected current is related to the image charge drawn to the collector parts (which is measured) relative to the total image charge.

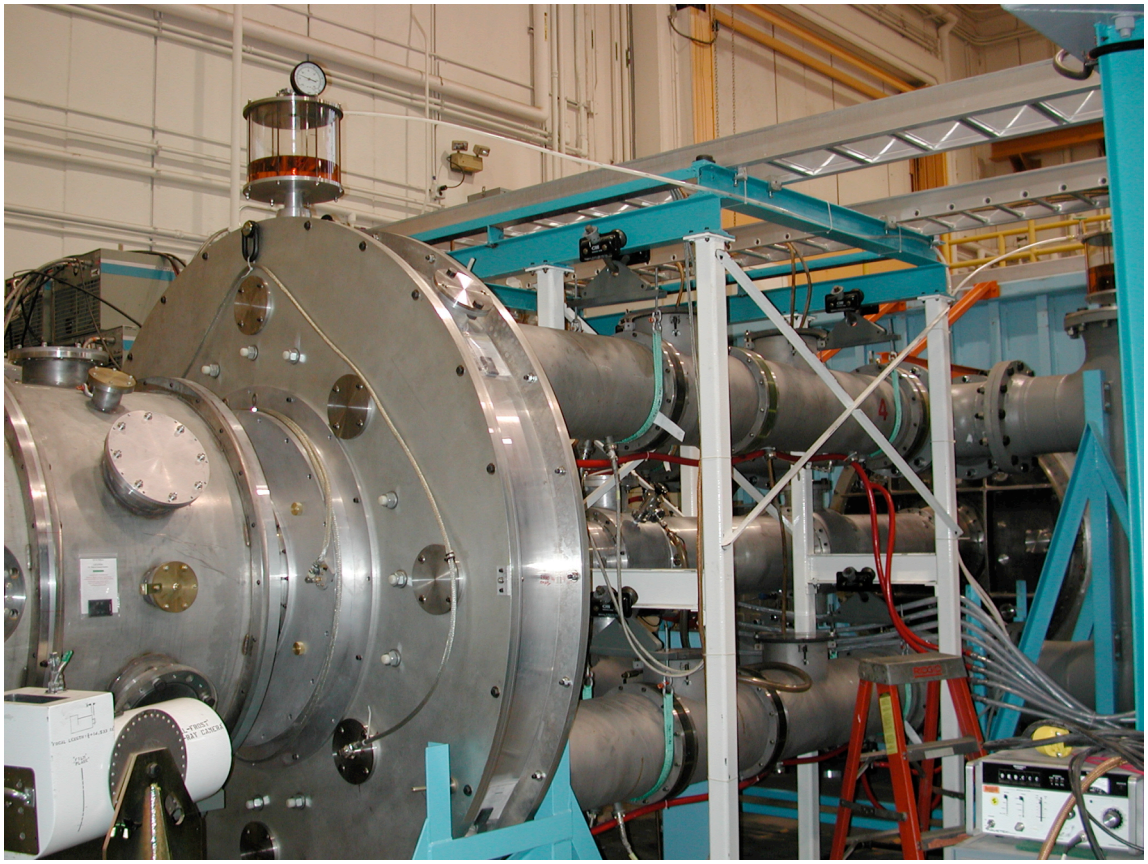

Figure 12. The pulsed power driver on which the experiments were conducted.

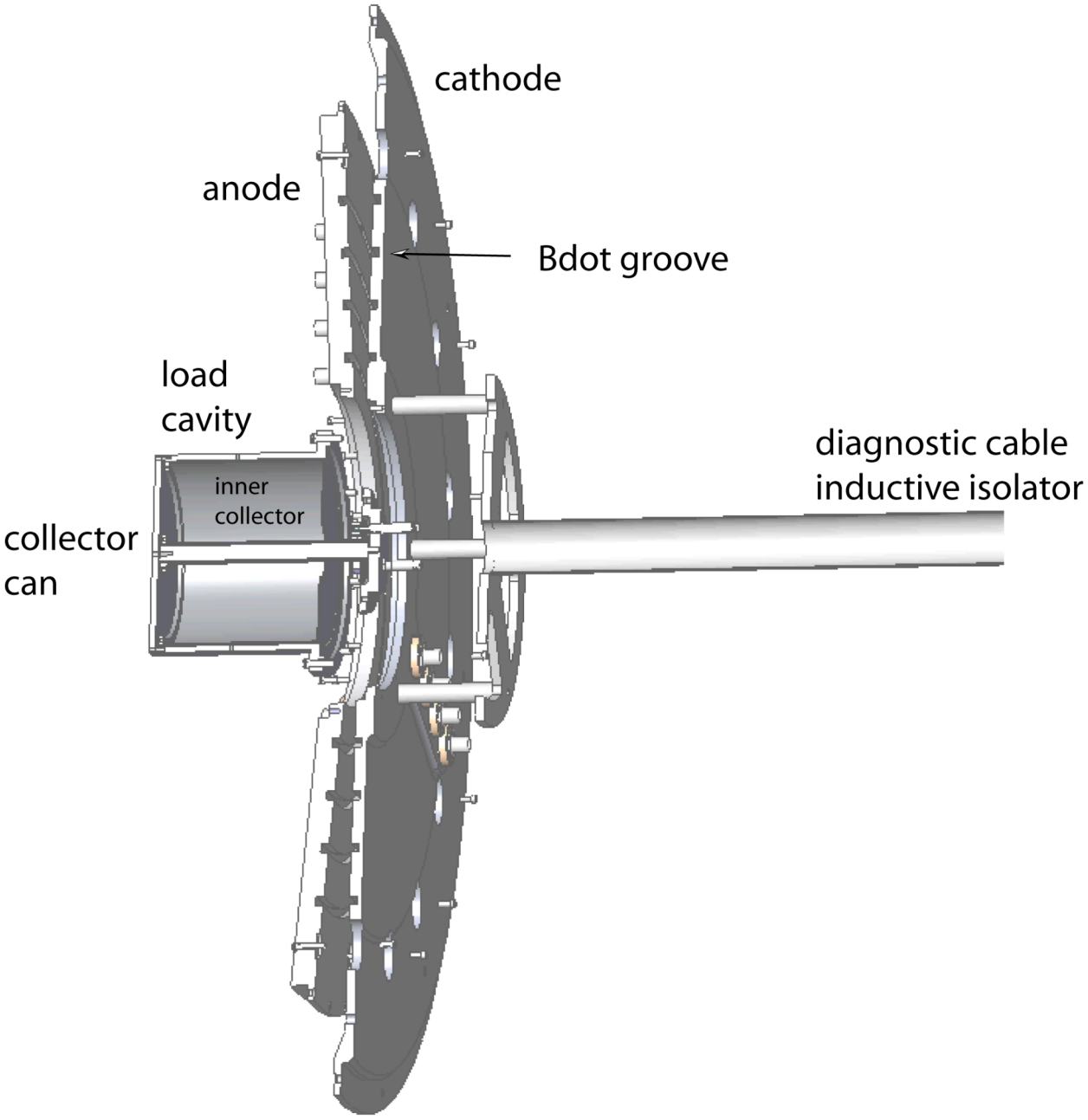

Figure 13. Cross-section of the disk MITL and electron collector hardware. The outer MITL anode radius is 46 cm.

Figure 14 shows the disk MITL cathode. The three current viewing resistor terminals can be seen in the picture. The cathode conductor is flat (except for the Bdot grooves) to simplify the simulation setup and interpretation. Figure 15 shows the inner electron collector can center spool and the collector can lid. The collector can parts are 1.5 mm thick stainless steel. Figure 16 shows the cathode Bdots with the polyamide tape covering the Bdots themselves. The tape cannot of course change the field on the Bdot loop until it emits enough electrons to reduce the field appreciably. If the cathode were

covered in flowing electrons at all times, large fields at the Bdot loop would not be expected. For that reason, we conclude that in this system, even with the cathode covered in a carbon coating, the electron emission is not uniform. Figure 17 shows the MITL anode pulled away from the cathode.

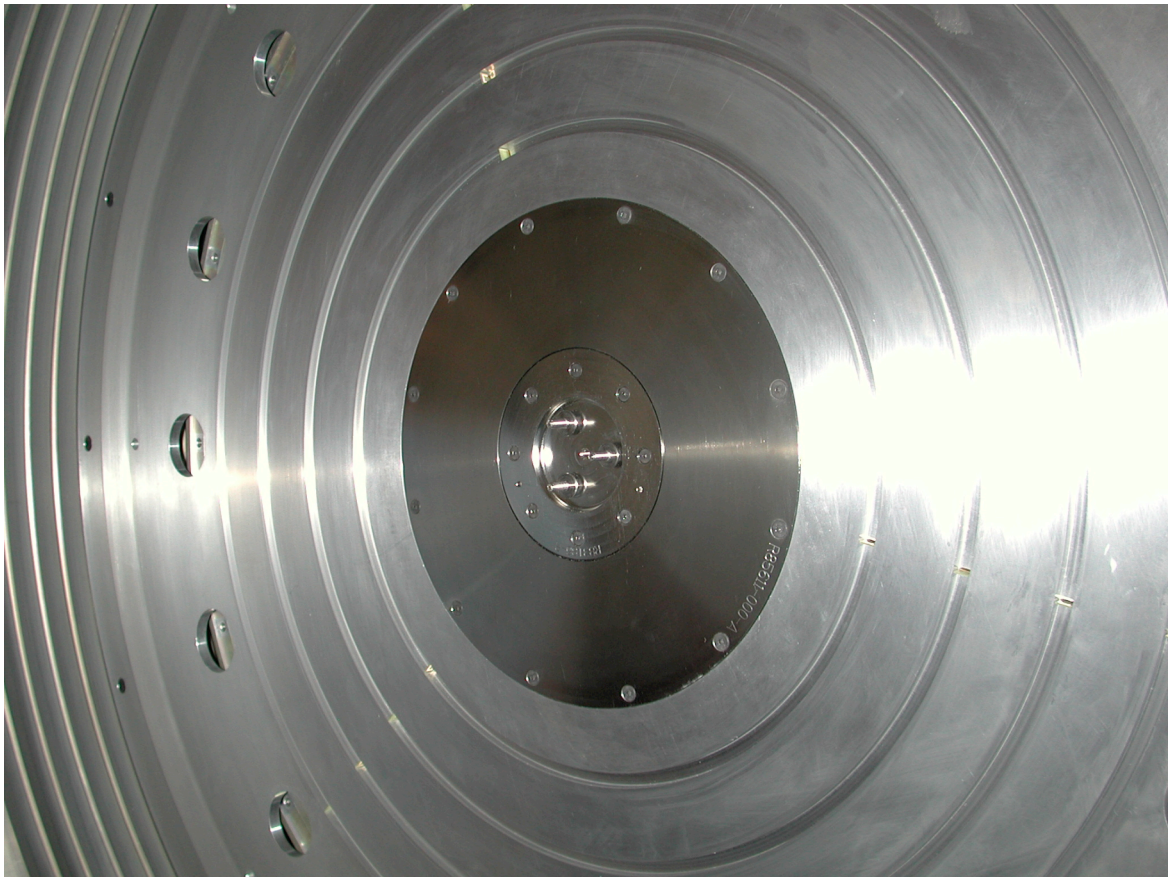

Figure 14. Cathode of the disk MITL hardware. The Bdot grooves are 1 cm deep and 1 cm in radial width.

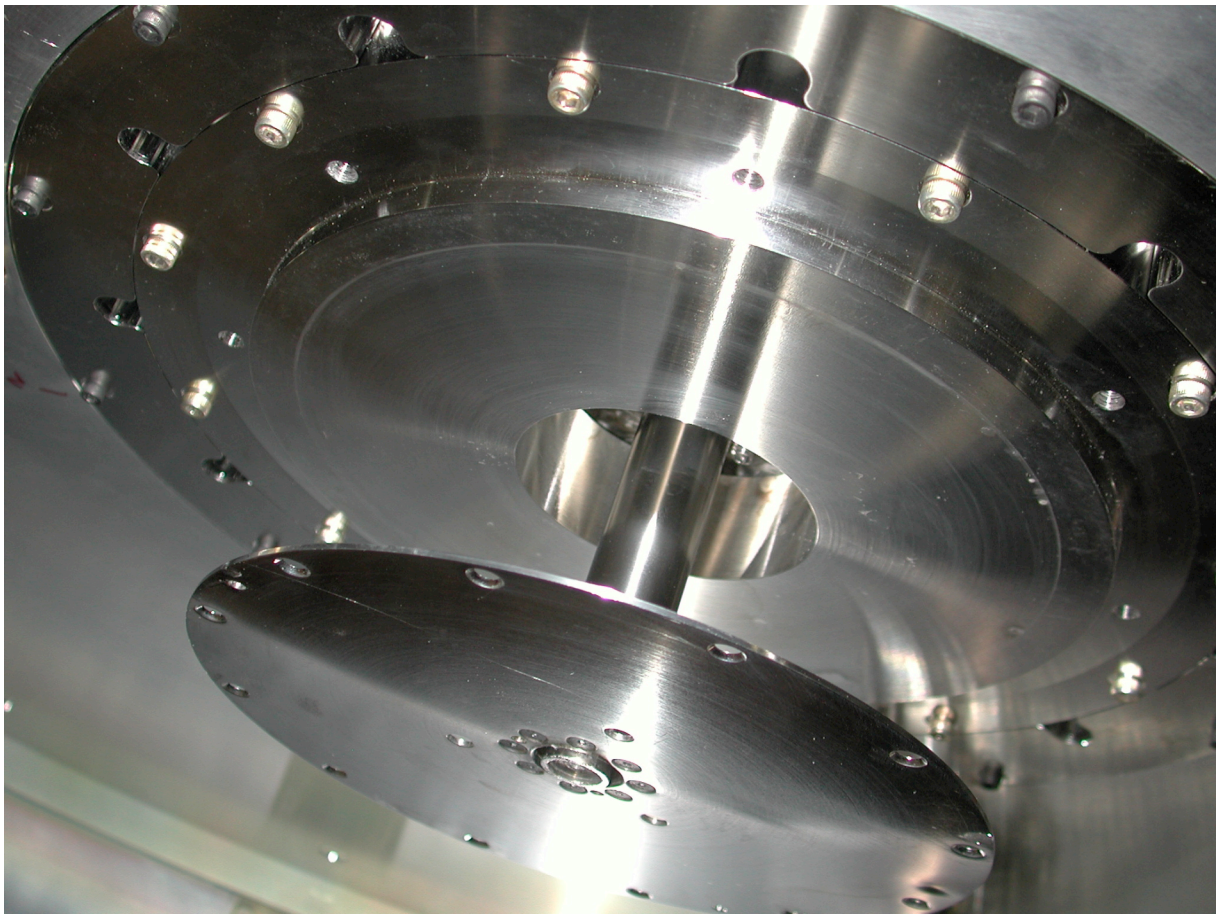

Figure 15. View showing inner electron collector center spool and lid. This is the configuration most often used because of the reduced mechanical alignment problems.

There were problems with the Bdots on the cathode. The monitors emitted electrons from the Bdot loop conductor itself. In an attempt to solve this problem, the Bdots were installed into a new cathode plate in which the Bdots were recessed into holes instead of grooves. The problem of electron current emission was reduced slightly, however the actual signal was reduced about an order of magnitude. The net 'signal-to-noise' ratio was substantially worse with the Bdots in holes. However, placing Kapton tape over the Bdots on the cathode eliminated electron emission from the Bdots. This is because the Kapton quickly builds up a surface charge that reduces the electric field on the Bdot itself. The cathode with Kapton tape over the Bdot holes is shown in Figure 16. Figure 16 also shows the graphite coating applied to the cathode surface to insure electrons were emitted. Because the electron flow measured was lower than expected from the particle simulations, an attempt was made to reduce the voltage threshold for cathode plasma formation and electron emission. For pulses of 40 ns duration, cathode plasma formation is usually observed at fields lower than the 400 kV/cm seen in this experiment [43]. A layer of graphite applied to the cathode surface will reduce the threshold for plasma formation and electron emission. Presumably, the rough microscopic surface of carbon with the entrained water vapor has a lower threshold for gas emission and ionization. Low electrical conductivity materials such as carbon (velvet cloth is also commonly

used) have much lower thresholds for electron emission when used as electron gun cathodes.

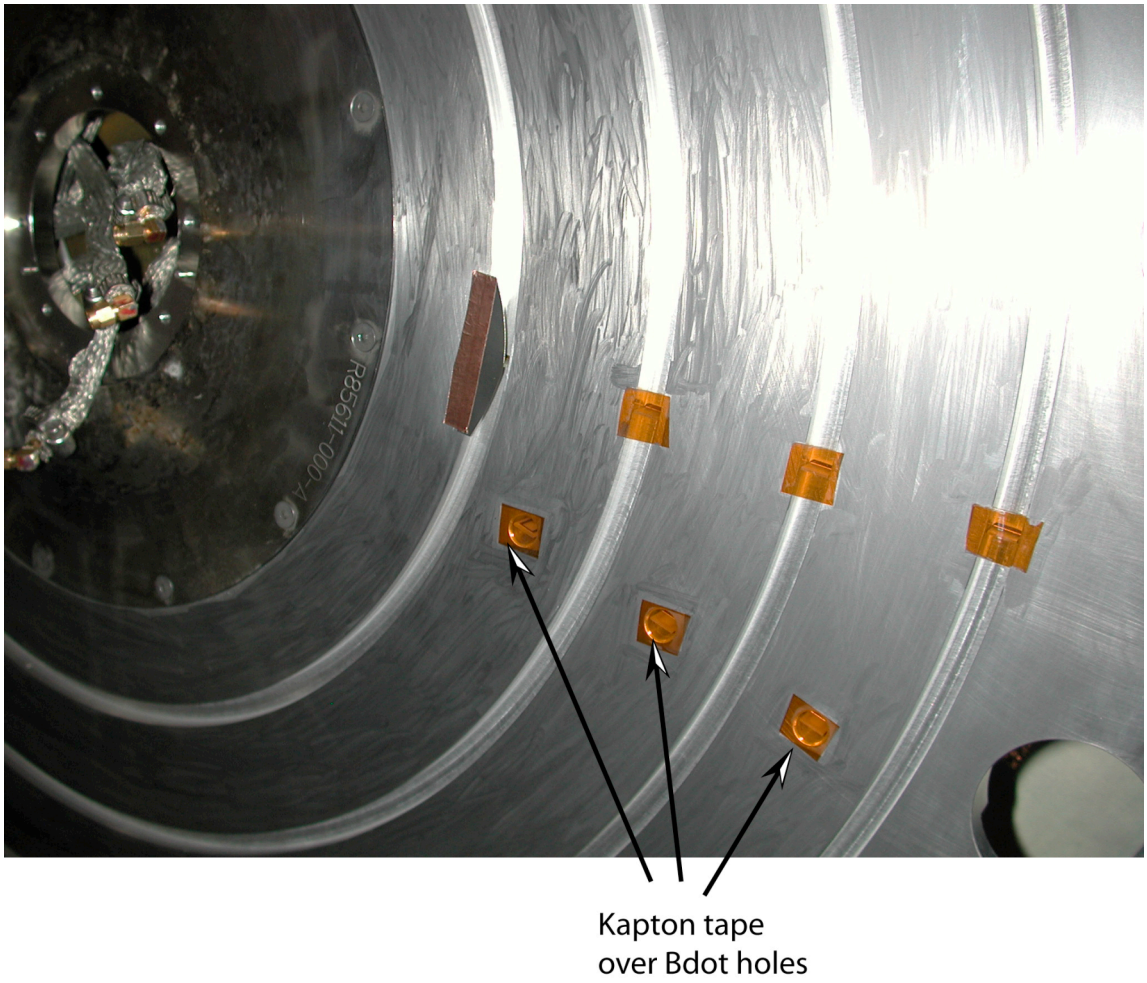

Figure 16. Cathode Bdots showing polyamide tape over Bdots to reduce the electric field at the Bdot itself.

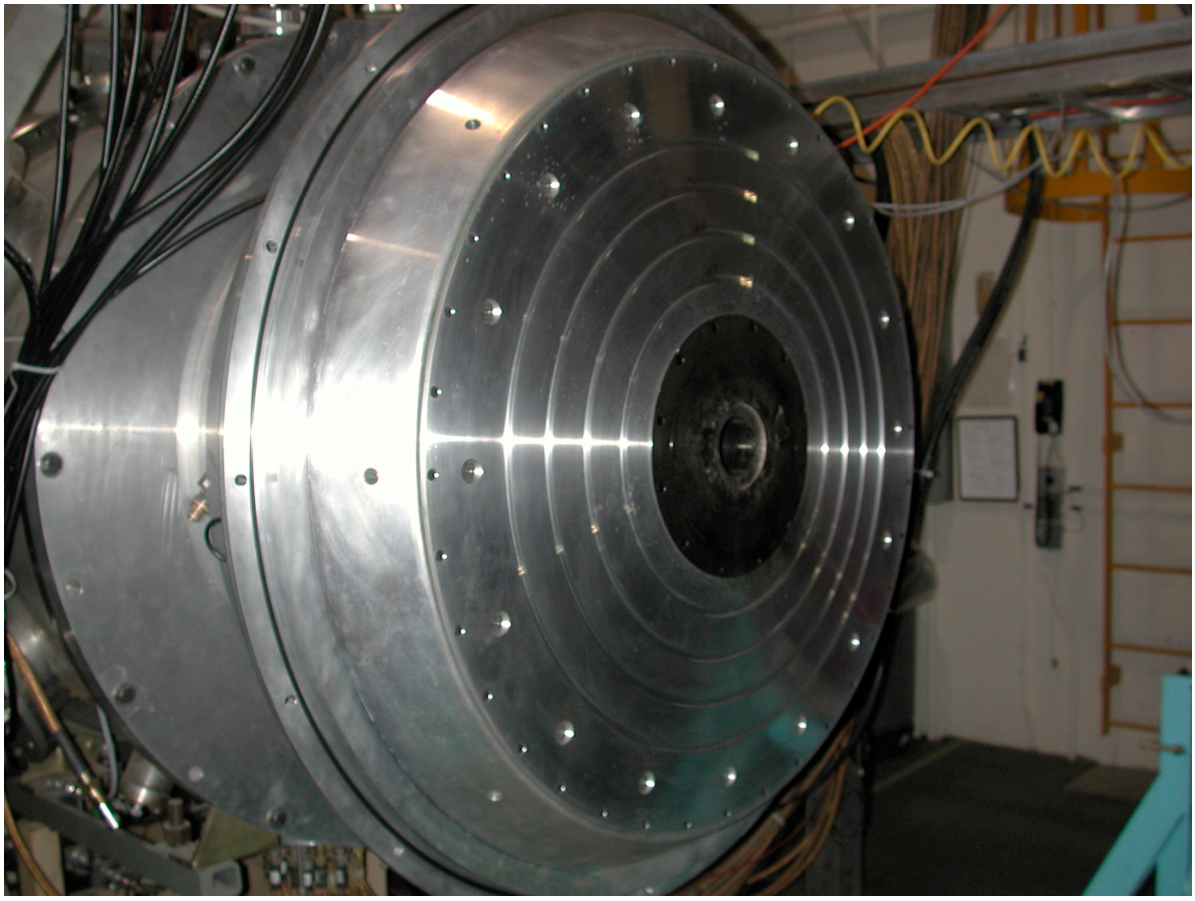

Figure 17. The anode of the disk MITL.

Experimental data

The experimental data for this system is limited because of a failure of the vacuum insulator stack. This limited the number of experiments on the MITL system. The anode and cathode currents for an experiment are shown in Figure 18 and Figure 19 for shot 558. The monitors are labeled by inductance from the axis. The monitor I60p is an anode monitor in the outermost groove (60 nH from the center of the machine). The cathode monitor I59n is located in the outermost cathode hole radius. The signals shown are the average of three monitors equally spaced at the same radius.

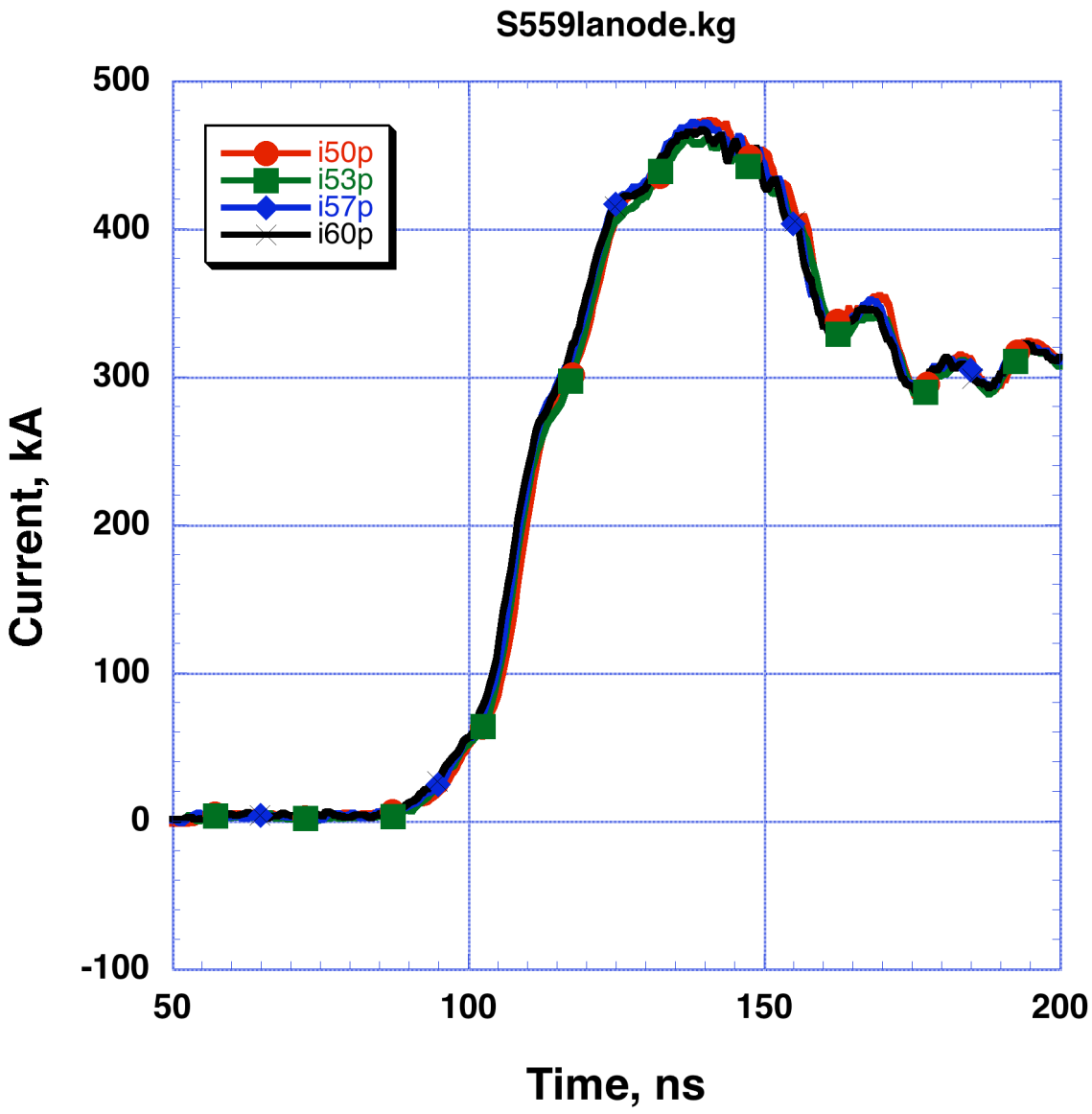

Figure 18. Anode current measured in disk MITL on shot 559. Each signal shown is an average of three monitors equally spaced in azimuth, individually recorded and numerically averaged. Alternating monitors are oriented differently (with positive and negative scale factors) so that common-mode noise would be evident.

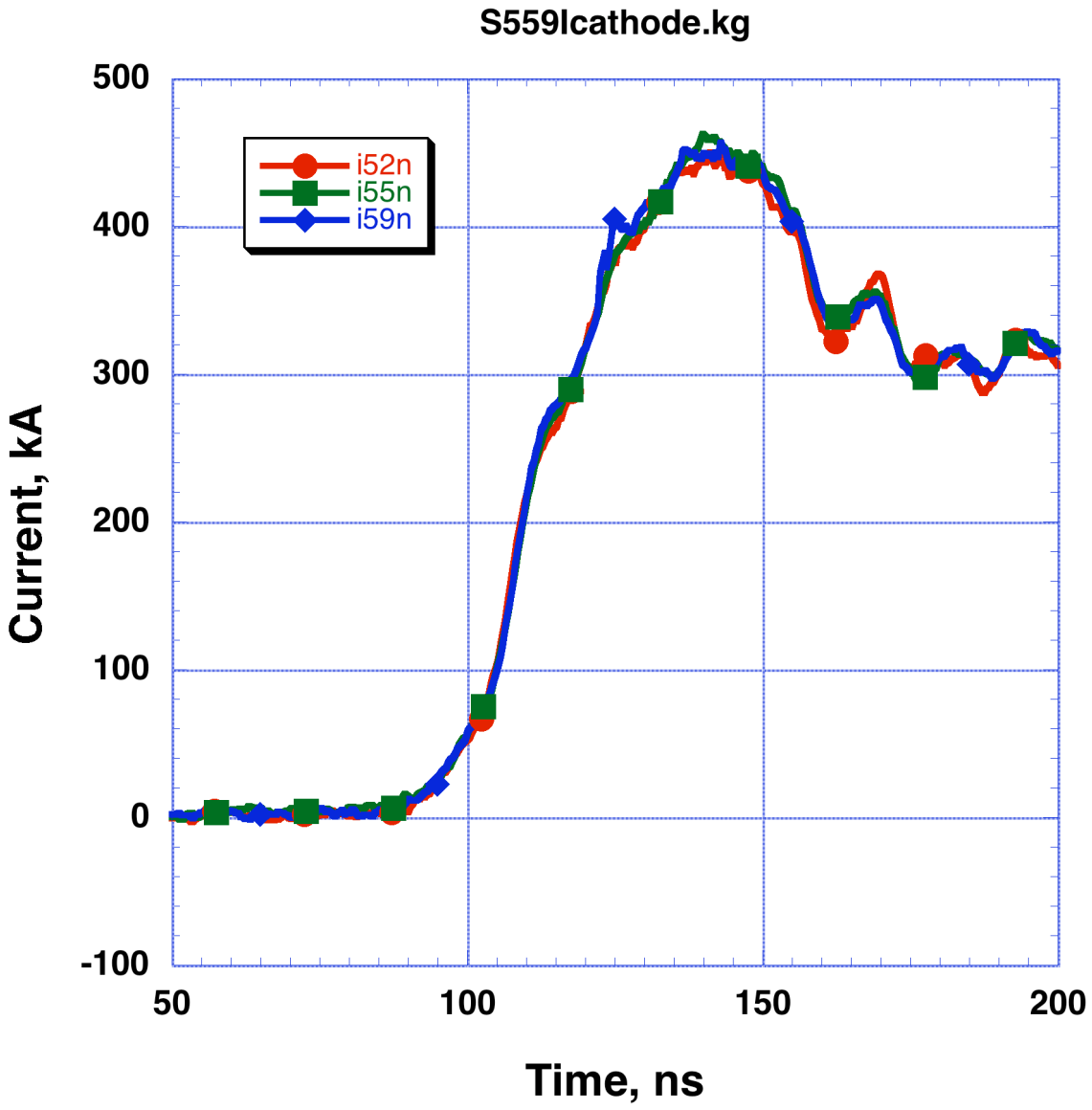

Figure 19. Typical cathode current measured at three radial locations in the disk MITL on shot 559. Each curve shows the average of three equally spaced (in azimuth) monitors recorded individually and averaged numerically.

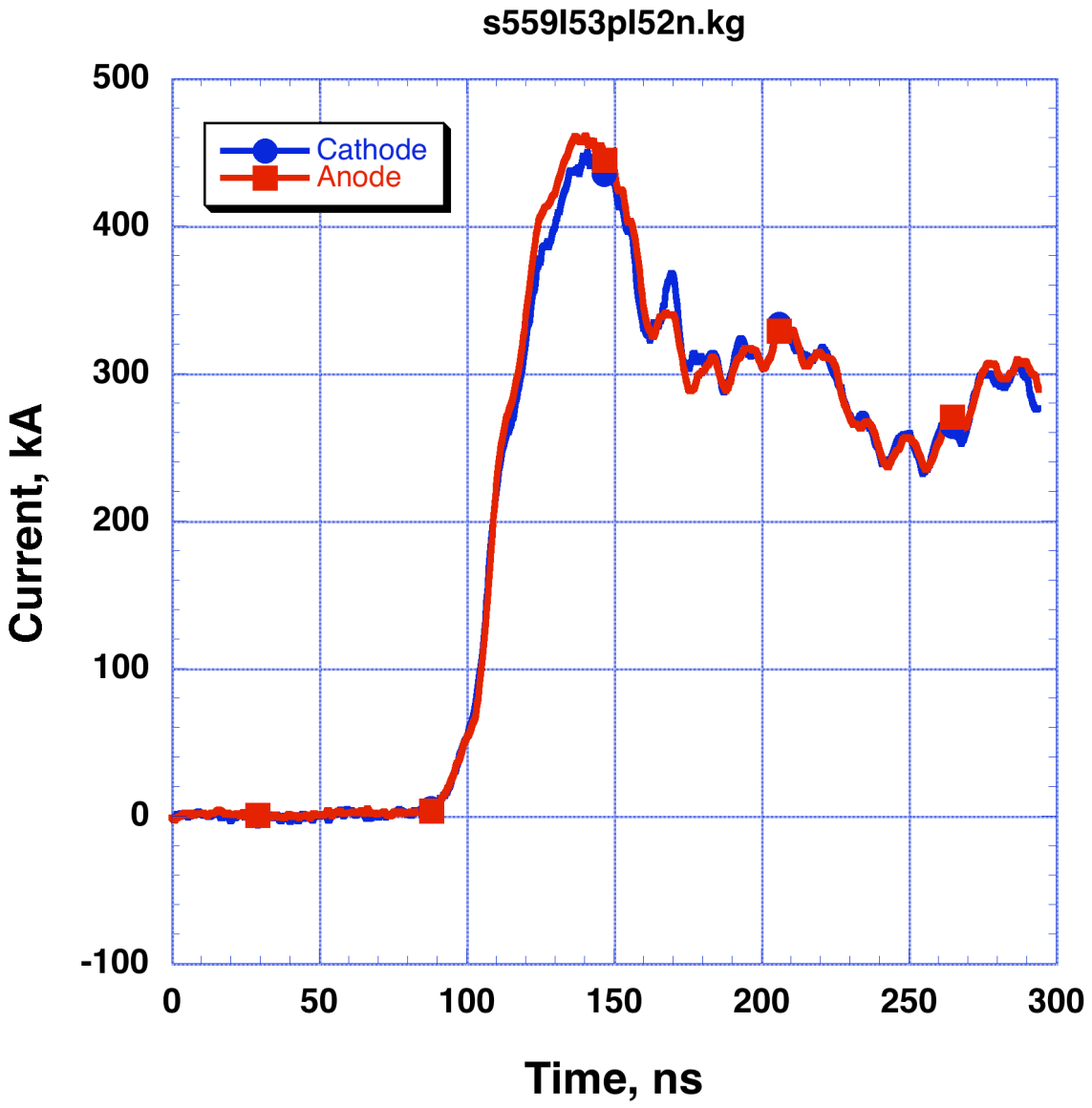

Figure 20. Anode and cathode currents on shot 559. The agreement between the measured currents early in time and late in time when electron flow is known to be small shows the accuracy of the measurements.

The electron current can be calculated from subtraction of the cathode current from the anode current at a given radius. Figure 20 shows anode and cathode current measured at the same radial location. Each is an average of three equally spaced monitors. The agreement between anode and cathode current at times when the electron flow is known to be small (for example, late in time when voltage is low) demonstrates the accuarcy of the measurements. The late-time difference in anode and cathode current is ~5 kA peak. At that time, the total current is ~300 kA. This gives an expected accuracy of 1.7%. The effects of common mode shield current increases relative to the inductive time constant of the cable ground system, so that earlier in the pulse, the accuracy is better. Such a number is reasonable for the digitizers used, noise effects, and calibration and time shift errors.

The electron current may also be measured by the electron collector system. The collector can is a floating electrode supported by three current viewing resistor terminals. The electron collector has some similarities to a 'Faraday' charge collector, but in the electron collector the total machine current flows in the outer collector can walls. The collector works because the electron flow becomes unstable when entering the large diameter can. The reason the electron becomes unstable is because the electrons must slow because of the increased wave impedance (reduced electric field and increased magnetic field). The electron drift velocity scales as $\frac{E}{B}$ and the reduced drift velocity at small radius causes bunching of electrons flowing from larger radius. The original intention was to build a collector that was enclosed except at the entrance to the can. This is shown in Figure 21. The electrons draw an image charge to the inner collector can when an electron enters the inner can. Electrons will strike the inner can when their space charge overcomes the magnetic field. The gap between the outer and inner can is 1.5 mm. This small gap was chosen to maximize the number of electrons that go inside the inner collector. However, alignment issues with the driver and flexing of the collector itself made shorting between the inner and outer can (even during the machine pre-pulse) common. For this reason, later experiments were done with only a partial can. This is shown in Figure 22. The collector indicates the fraction of image charge drawn on the inner collector parts. To estimate the fraction of image charge measured, an electrostatic model was studied. The electron collector monitor will register image charge when an electron enters the collector can region. If the electron reaches the anode by striking the collector itself, the monitor won't change since the image charge has already been 'counted.' However, if the electron leaves the region and reaches the anode at a place other than the can, the image current will invert and be 'subtracted' from the collector can signal. Thus, electrons will be counted if they enter the can and flow to the collector, or if they enter the can and stay in space. If the electrons leave the collector region they will cause no net current signal on the collector monitor.

The collector can is connected to the MITL cathode near its current-viewing resistors. If the can electrically contacts the MITL at another point (due to mechanical mis-alignment or gap closure due to plasma) the collector signal will be opposite polarity from electron collection. This is important for distinguishing between electron collection and alignment problems.

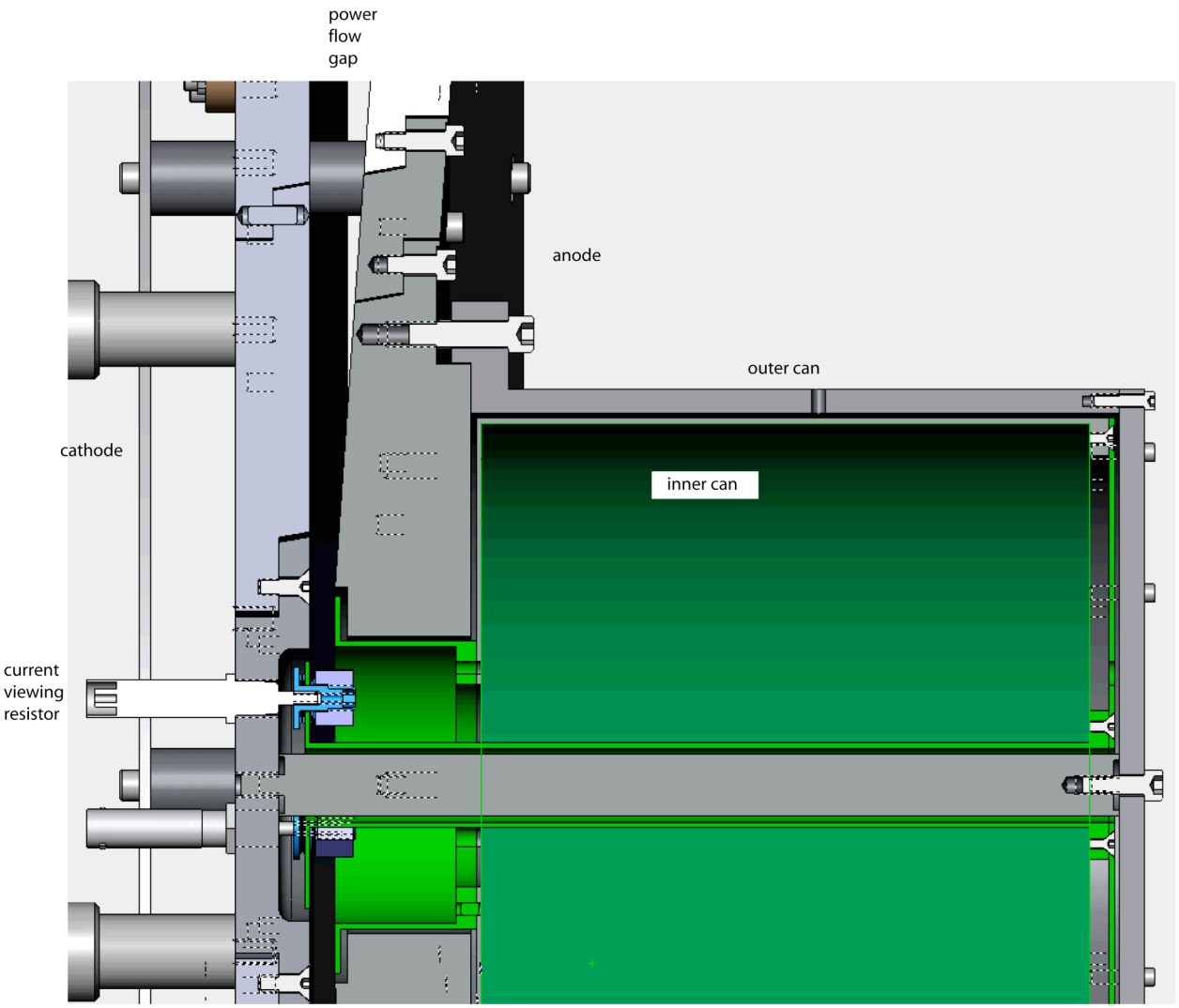

Figure 21. The electron collector. The full collector (green) is shown. Electrons strike the inner can. The current viewing resistors indicate image current once an electron enters the can. Electrons do not need to strike the can to be measured, but large space charge fields exist if the electrons do not reach the anode. The gap between the outer and inner can is 1.5 mm. Full machine current flows in the center rod while electrons are collected by the can and their current flows through the current viewing resistors.

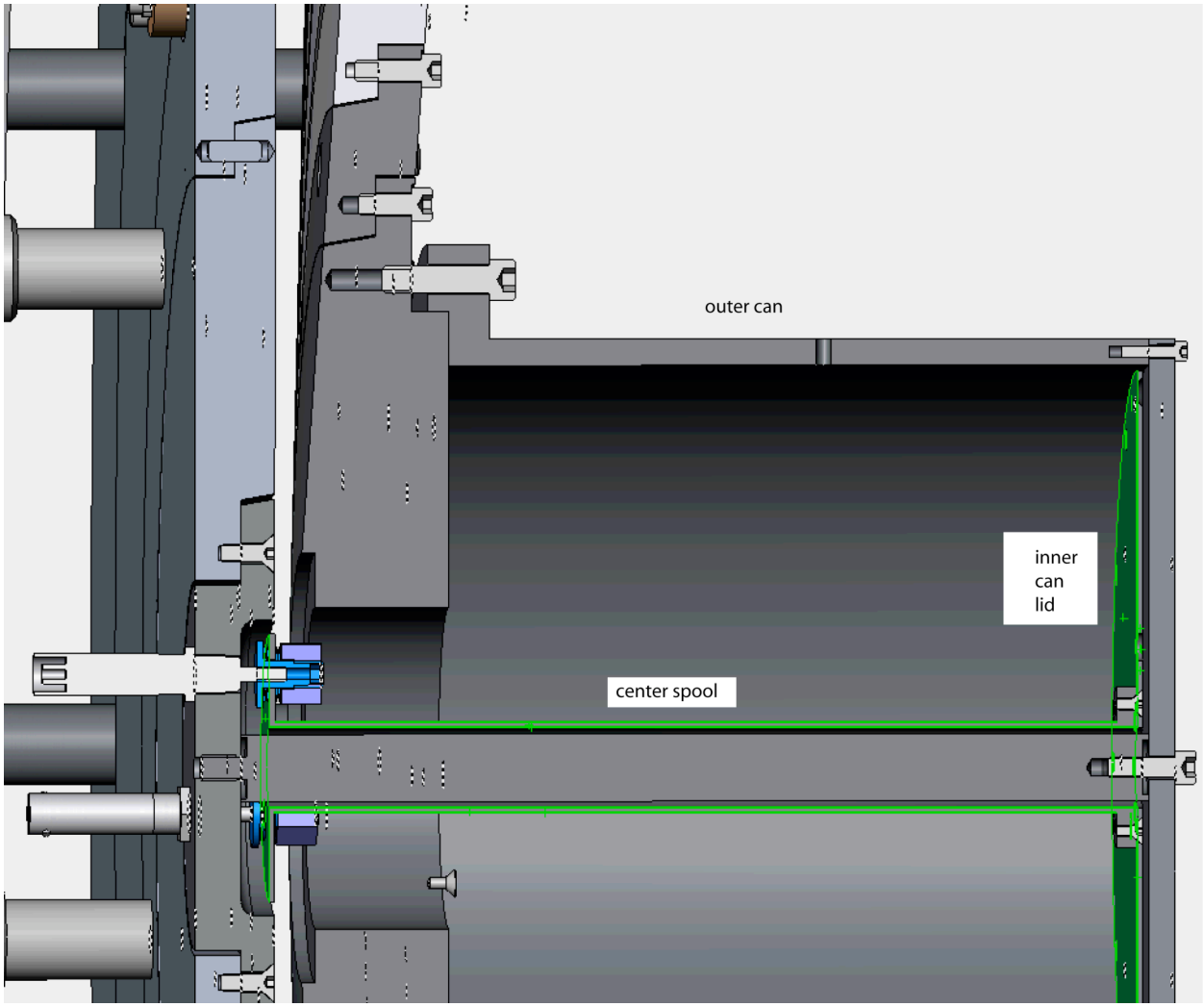

Figure 22. The partial electron collector used. The collector (green) carries image current for electron space charge in the region. This configuration simplifies can alignment. The gap between the outer and inner collector is 1.5 mm on radius.

An electrostatic simulation will accurately indicate the effect of electron space charge in the can region since the dimensions of the can are small compared to the pulse length divided by the speed of power flow. The location of the space charge was taken from data obtained in the particle in cell simulations at peak voltage (Figure 23).

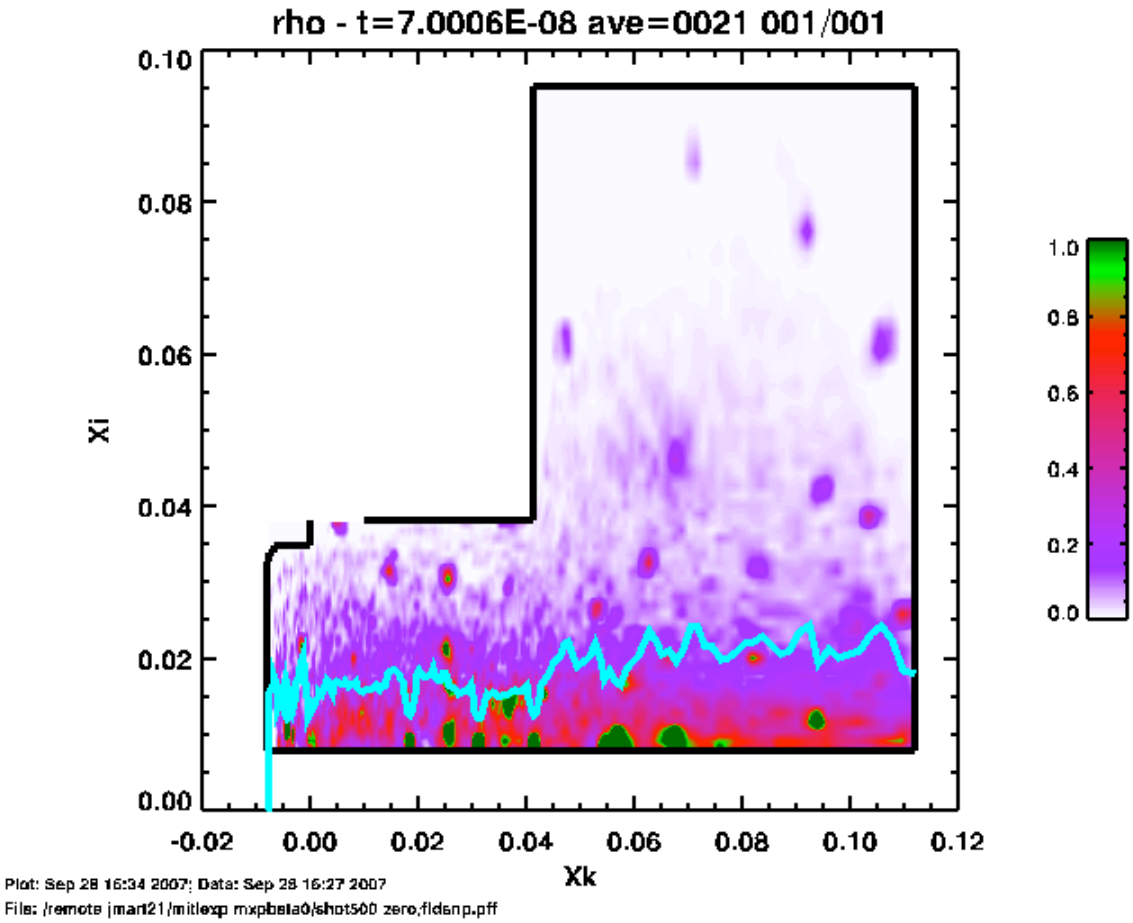

Figure 23. The charge density in the collector can region at 70 ns for a low voltage simulation. The cyan line is the charge centroid.

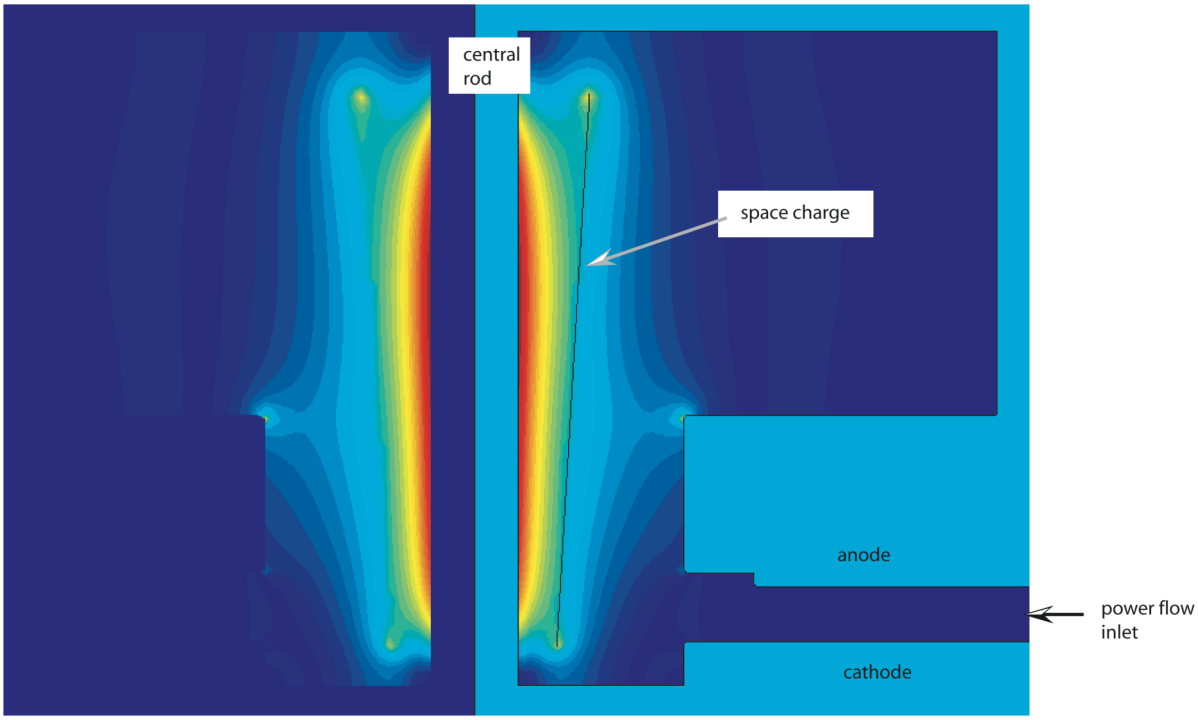

Figure 24. The electrostatic simulation geometry. The regions with the partial inner collector will measure 75% of the image charge for space charge located as shown. Note the Figure is rotated compared to the simulation geometry.

The data from an experiment with the partial inner collector are shown in Figure 25 and Figure 26. The collector can current as well as the difference of anode and cathode currents is shown. The anode-cathode current differences indicate excess electron flow late in the pulse (when voltage is essentially zero) presumably due to plasma carrying current on the surface of the polyamide tape covering the cathode Bdots. The collector can current in the Figure is not corrected for the incomplete image current collection. The scaling of the current by 1.3 raises the indicated peak current to 37 kA. This agrees reasonably well with the indicated anode-cathode difference at the time of peak voltage.

The peak of the electron collector current is delayed with respect to the voltage pulse. The timing accuracy is of order 1 ns due to cable measurement errors. The drift velocity of the vacuum flowing electrons in the load region is about one tenth the speed of light. This would account for several nanoseconds (the distance from the anode and cathode Bdots to the collector can shown is 20 cm, or 700 ps at light speed). With the reduced drift velocity, 5 to 7 ns could be expected for electron transit time [6].

While the amount of experimental data is less than desired, it appears that the current monitors and the electron collector indicate reasonable electron currents.

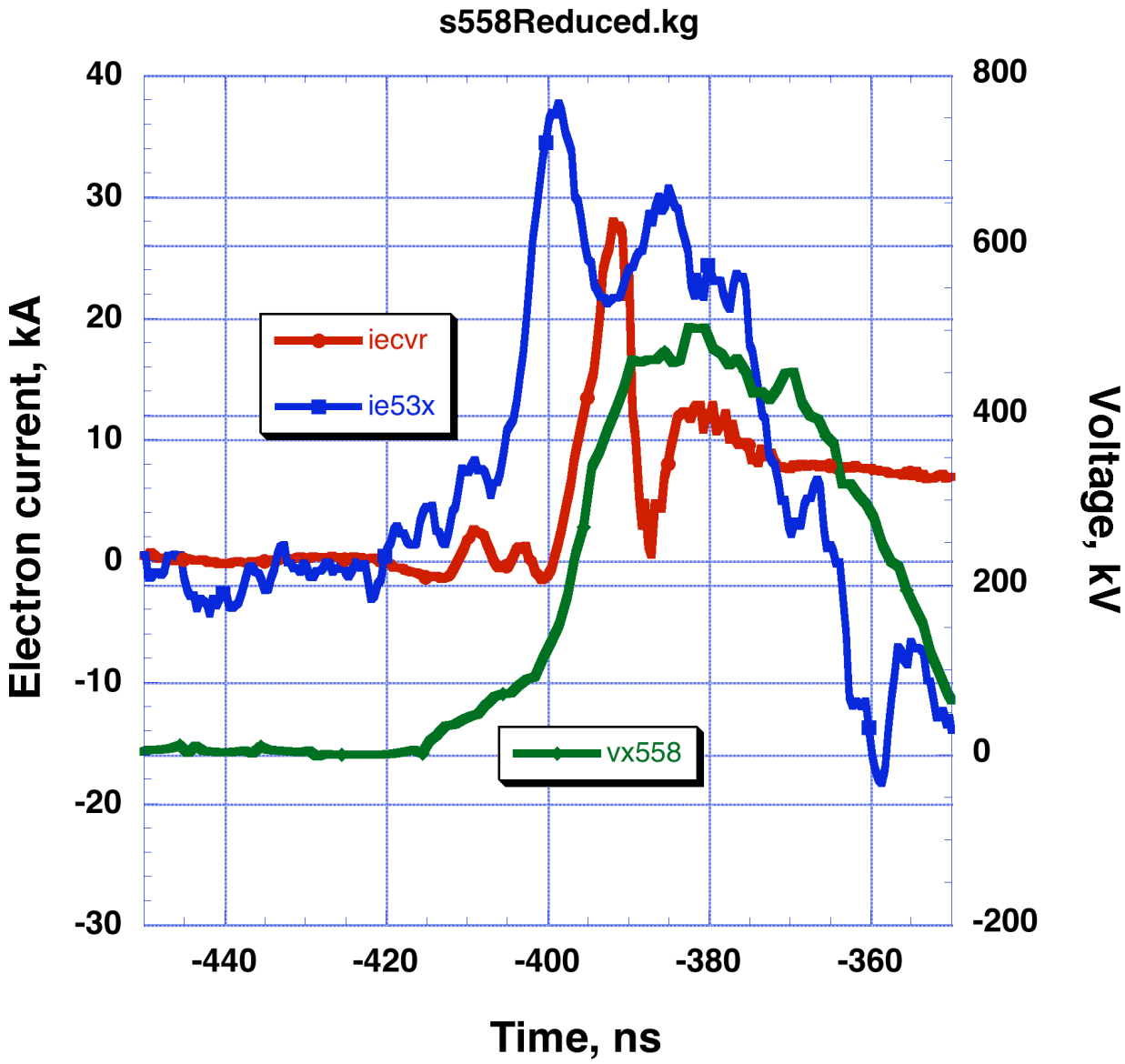

Figure 25. The collected electron current (red, circles) and the difference of anode and cathode current (blue, squares). The voltage (green, diamonds) is also shown. The data are from shot 558. The MITL configuration is the constant-flow (beta=0) geometry.

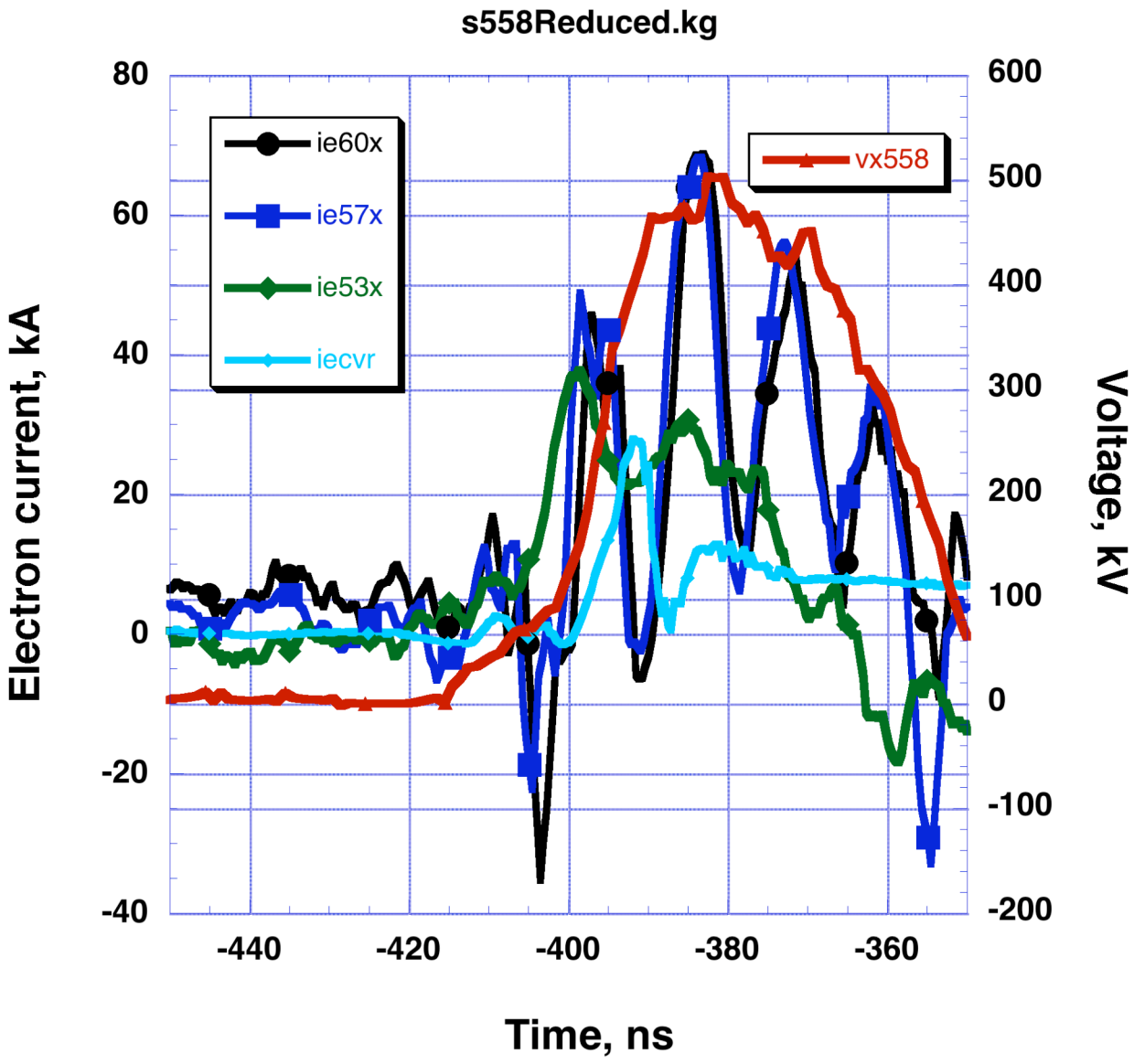

Figure 26. The four radial current monitor positions anode-cathode current differences (ie60 is the outermost set; ie53 is the innermost set). The collector can current (iecvr) is also shown. The ringing on the current monitors is a result of voltage variations (vx is the voltage signal) from timing differences in the four drive lines feeding the transmission line.

Simulations

Particle in cell simulations were done to complement the experimental data. The simulations have the advantage of much more access to behavior of the system. The simulations of course only include the physics set up in the modeling software. The models used here did not include electrode plasma (and therefore not gap closure). The simulations were done with Quicksilver [44]. The geometry was imported from CAD drawings of the hardware.

The simulations were done in both time-accurate mode (with a forward wave from the experiment) and static mode. Static mode has the advantage of being equilibrated so time averaging can be done to improve the resolution of some effects.

The simulations were run on a computer cluster at Sandia National Laboratories in Albuquerque. The simulations were usually run on 16 processors. The simulations used cell sizes of 200 μm near the cathode. The time step was 625 fs. The peak number of particles in a simulation was about 250 thousand for the low voltage runs, and about 100 thousand for the higher voltage simulations.

Static simulations

The electron flow current in the initial simulations of the MITL experiment showed significant discrepancy with local application of the 1-D pressure balance model. With the full inductive load, it is difficult to determine whether this is a due to a numerical problem. To address this issue, we have performed simulations with a resistive load, driven with a voltage pulse that smoothly ramps up to a final value and is then held constant. We run the simulations out far enough in time to have a long period (at least 20 ns) at the final operating point. We then analyze the final state with time-averaging over a range of time windows. The static geometry is shown in Figure 27. The inner end of the MITL at r = 4.4 cm is connected to a 1-D transmission line, terminated with a resistor.

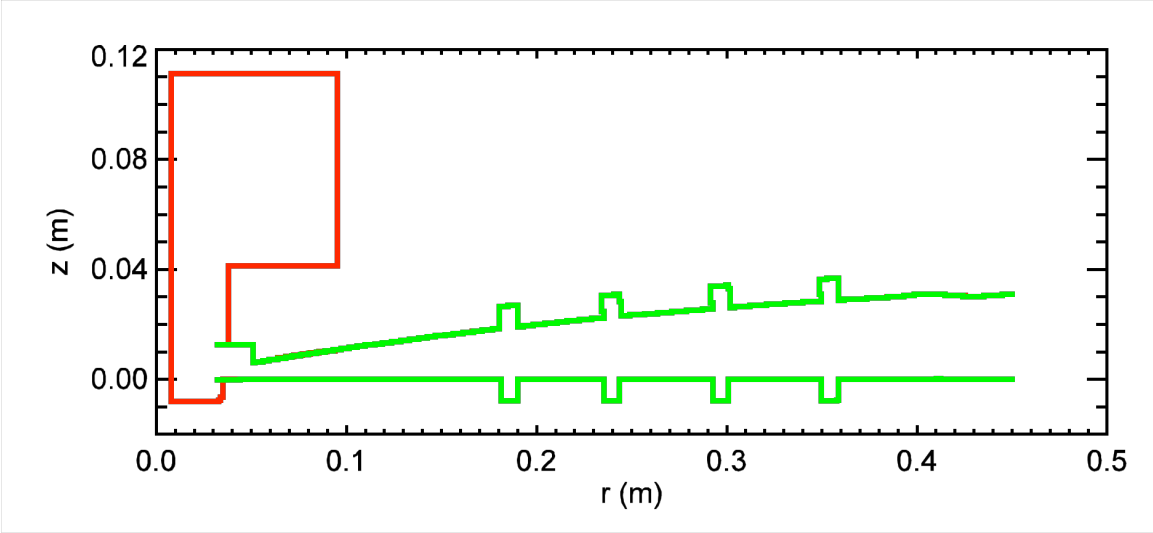

Figure 27. Comparison of the full inductive load (red) and static (green) simulation geometry.

The baseline run for this setup uses an operating point of V ~ 400 kV, and I ~ 170 kA. At this low voltage, there are issues with the QUICKSILVER field emission model. In this model, emission cells are initially non-emitting, and turn on only when the normal electric field exceeds a threshold value. We have typically used E_{thr} = 200 kV/cm. For a high voltage MITL, $(V/d)/E_{thr} >> 1$, the results are insensitive to this parameter. Here, the

electric field at the outer radius of the MITL is marginally high enough to turn on the emission cells. We have done simulations with threshold values of 200 and 50 kV/cm. The late-time voltage for these simulations is 386 and 358 kV respectively.

Results of the flow current profile, time-averaged over a 20 ns time window, are shown in Figure 28. In the 200 kV/cm case, the only emission for r > ~0.2 m is off the corners of the cathode grooves. Thus the flow is much lower than the theoretical value. These results are qualitatively similar to the inductive load runs. In the 50 kV/cm case, the flow exceeds the theoretical value because electrons emitted at outer radius are able to flow downstream without being retrapped back to the cathode. This is illustrated in Figure 29. Note the very low electron density at the cathode for 0.18 < r < 0.32 m. The upstream electrons flowing into this region suppress emission, and so the electron density profile as a function of z is very different from the assumptions used for the 1-D pressure balance equation.

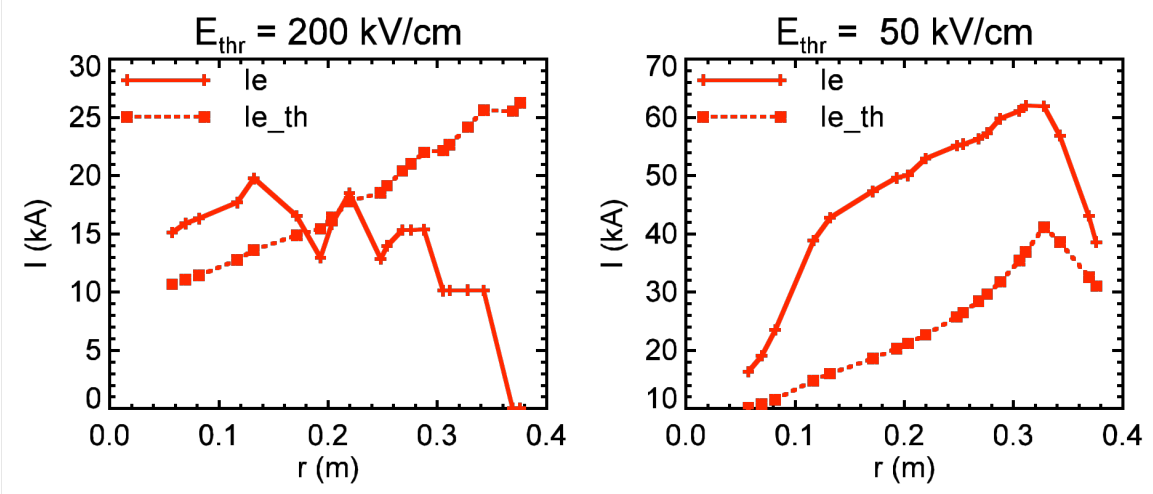

Figure 28. Comparison of the time-averaged electron flow current profile with the theoretical prediction for two emission threshold electric field values.

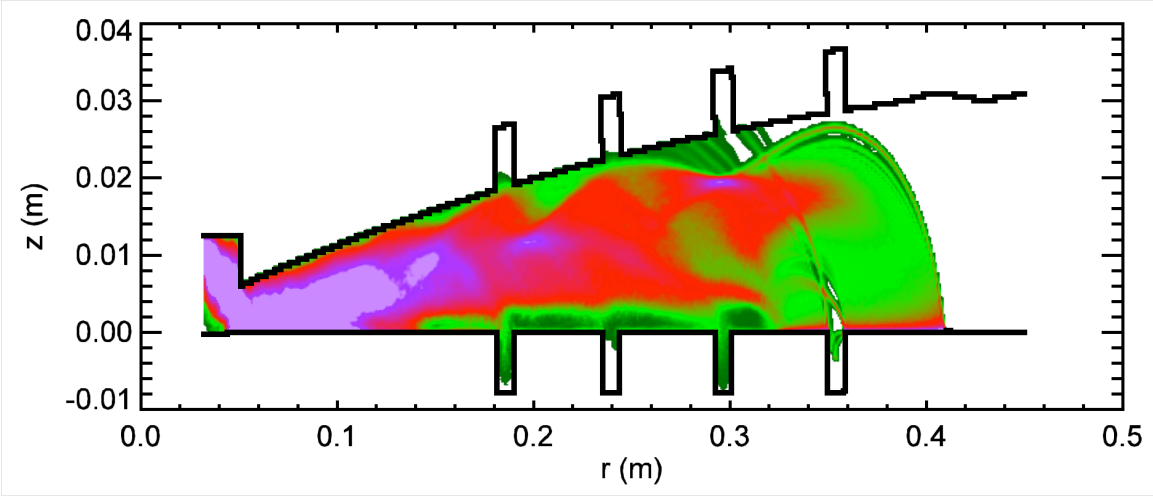

Figure 29. Electron charge density for the 50 kV/cm case, averaged over the same 20 ns time window used for the flow profile in Fig. 2.

It is reasonable to question whether the cathode grooves are contributing to the launching of the upstream flow far out into the gap. We also did simulations without the cathode grooves, i.e. a perfectly flat cathode. The flow current profiles are shown in Figure 30, compared with the grooved case. The agreement in the 50 kV/cm case is excellent. For the 200 kV/cm case, agreement is also good at small radius. At large radius, the field emission threshold is never exceeded with the flat cathode. We thus conclude that the cathode grooves have very little effect on the electron flow in the MITL.

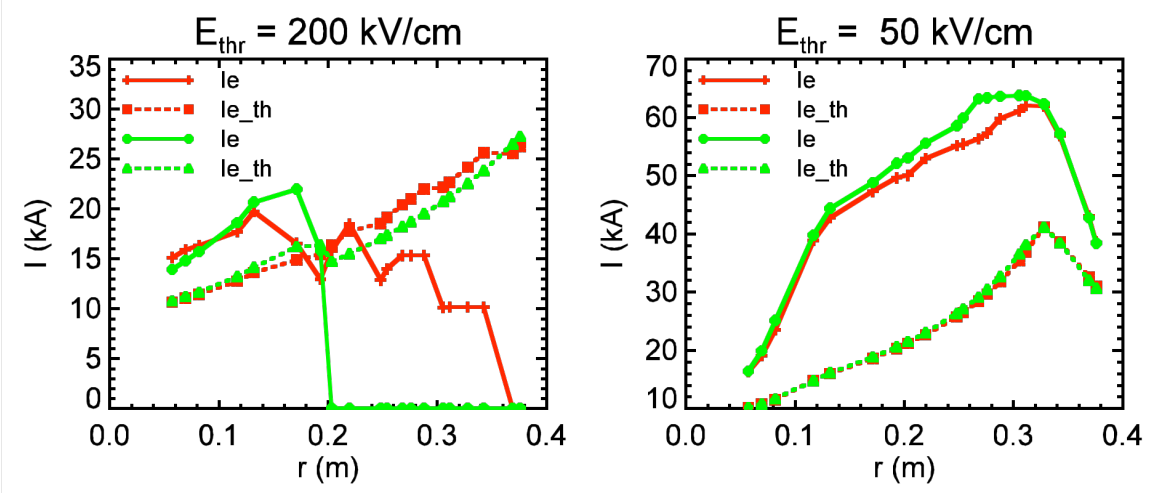

Figure 30. Time-averaged electron flow current profile for the grooved and flat cathode simulations. Red curves are for the grooved setup, green curves for the flat setup; solid curves are the simulation flow current, and dotted curves are the theoretical flow.

The electron flow current in the Z MITL simulations agrees very well with 1-D pressure balance model (provided the spatial resolution at the cathode is adequate). To

reconcile those results with the discrepancy observed with this setup, we are finally lead to suspect that operating at low voltage is the problem. We thus ran new flat cathode simulations at higher voltage.

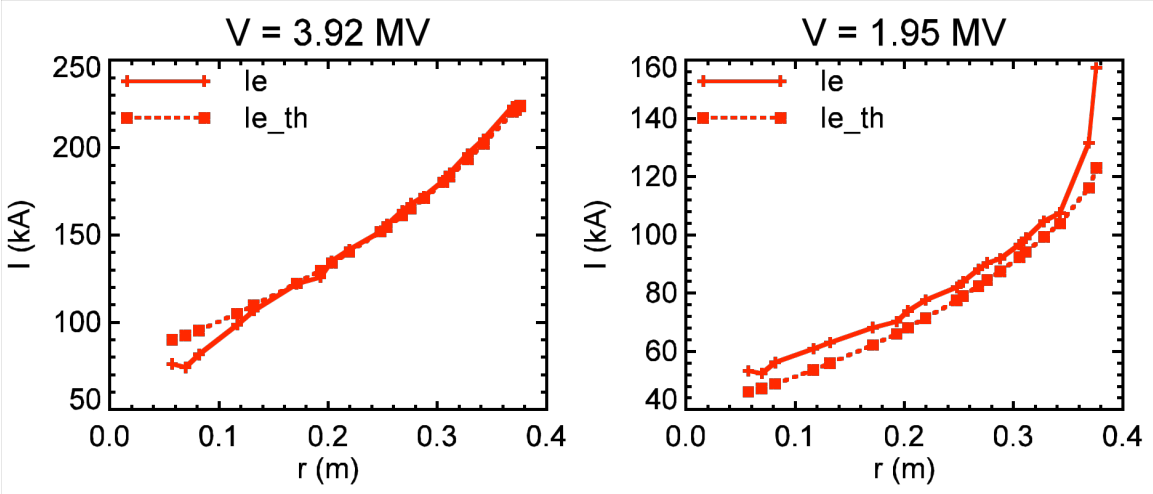

Figure 31. Time-averaged electron flow current profile for flat cathode simulations at higher voltage.

The results of two runs are shown in Figure 31. At the higher voltage, the agreement is excellent. The discrepancy at small radius is almost certainly due to the fact that we need finer spatial resolution to more accurately resolve the thin electron sheath here. For the second case, the simulation flow exceeds the theoretical value. The reason for this is exactly the same as for low voltage run with E_{thr} = 50 kV/cm, namely that electrons emitted upstream are not being retrapped to the cathode. Plots of the electron charge density analogous to Figure 30 show the same qualitative features.

In summary, the major points are:

- There are no apparent problems with the simulations, and the spatial resolution is adequate for the low voltage case.
- The cathode grooves do not greatly affect the electron flow, except that when using large values of E_{thr}, emission is possible at the cathode groove corners.
- At high enough voltage, we do in fact get excellent agreement between the simulated flow current and the 1-D pressure balance model.

Time-accurate simulations

The time-accurate simulations used a similar setup to the static simulations, except the input boundary condition was generated from an experimental forward-going

waveform, and the load was not resistive but inductive. Static simulations cannot be done with an inductive load.

The simulation geometry is shown in Figure 32, Figure 33, and Figure 34. The cell size near the cathode is 200 μm. The simulation time step is 625 fs. Several hundred thousand particles are tracked in the simulation. The simulations run in about an hour on 16 processors of a large computer cluster.

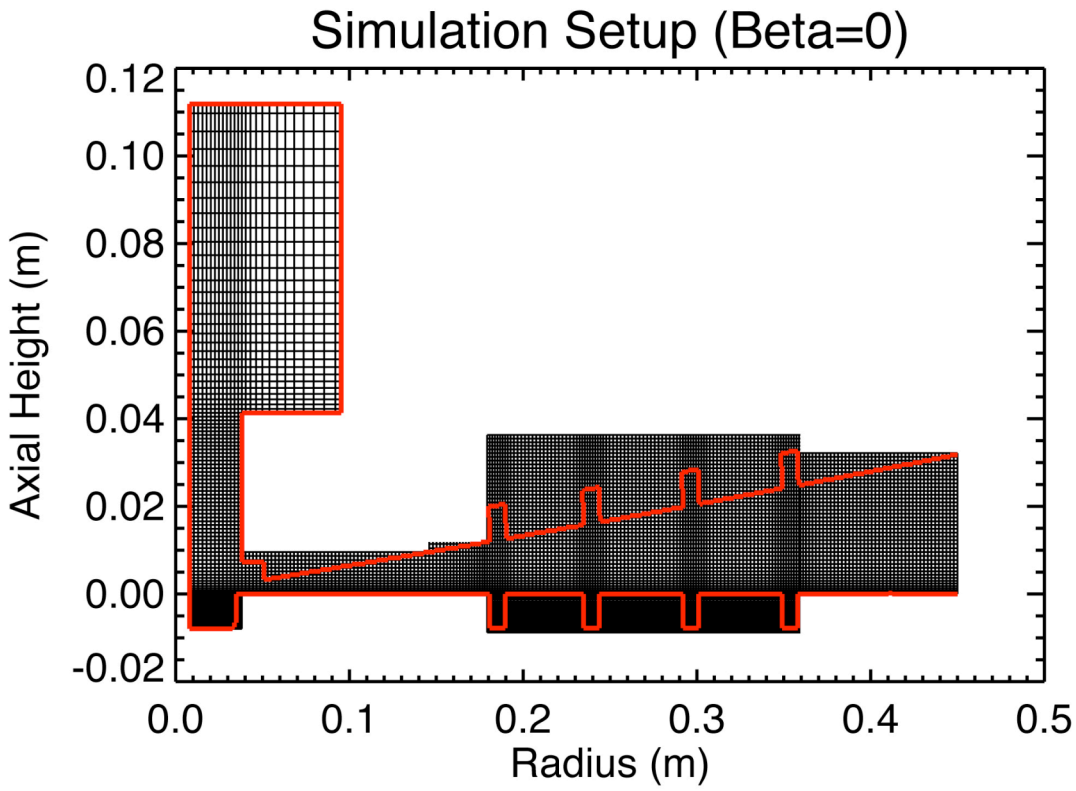

Figure 32. Simulation setup for the constant-flow (beta=0) geometry.

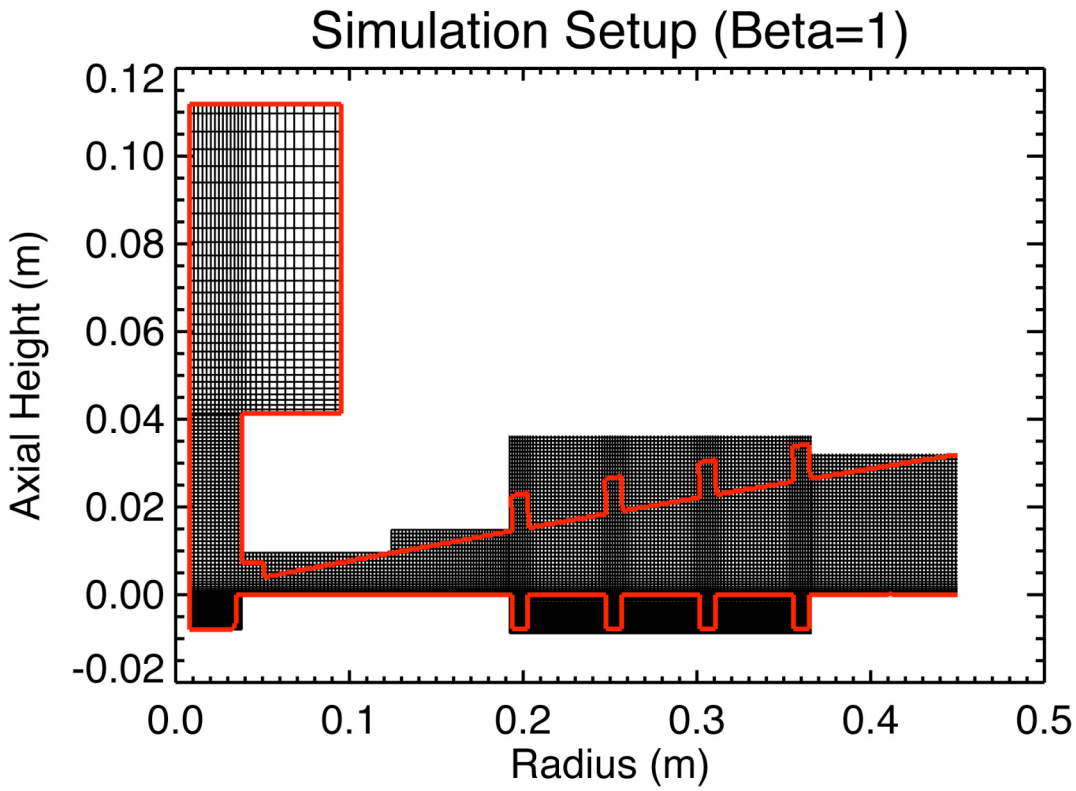

Figure 33. Simulation setup for the reducing flow (beta=1) geometry.

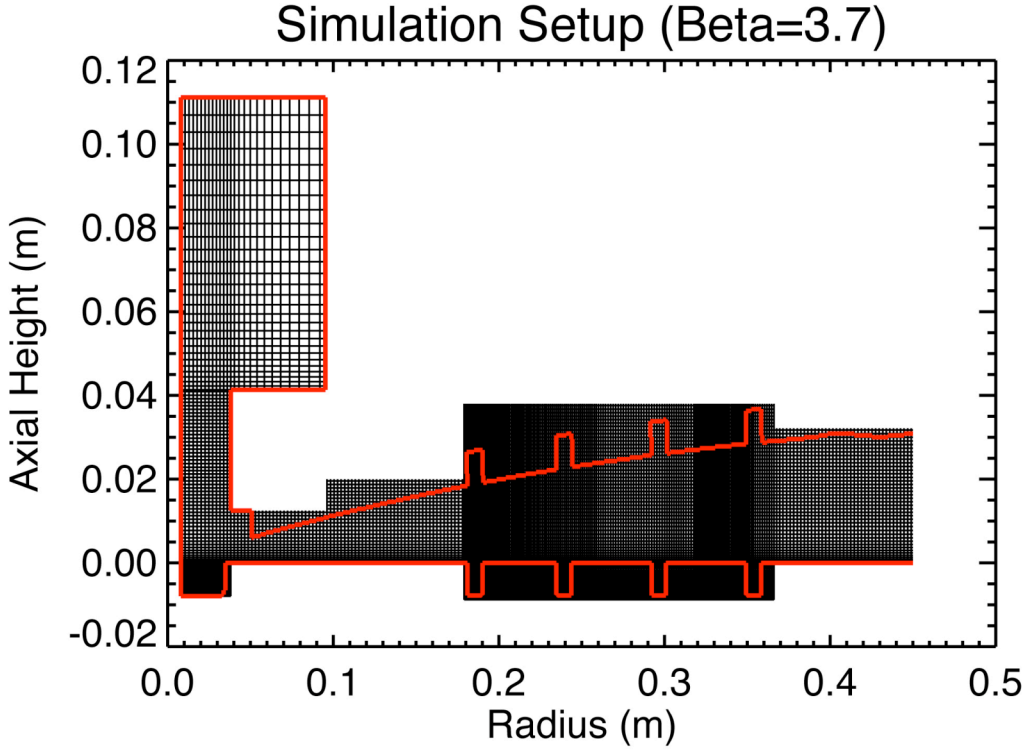

Figure 34. Simulation setup for the reducing-flow (beta=3.7) geometry.

The voltage for one of the simulations is shown in Figure 35 for the experimental voltage of ~500 kV and the higher voltage case in Figure 36. The simulations were also done with the forward wave artificially increased to about 10 MV to reduce the effect of space charge on the simulations. This was done because the model for generating the geometry was developed assuming the space charge correction of the electrons [6] was much less than the line voltage. This is not strictly true for the conditions of the experiment. The higher voltage simulations also are much less affected by the exact value of the electron emission threshold.

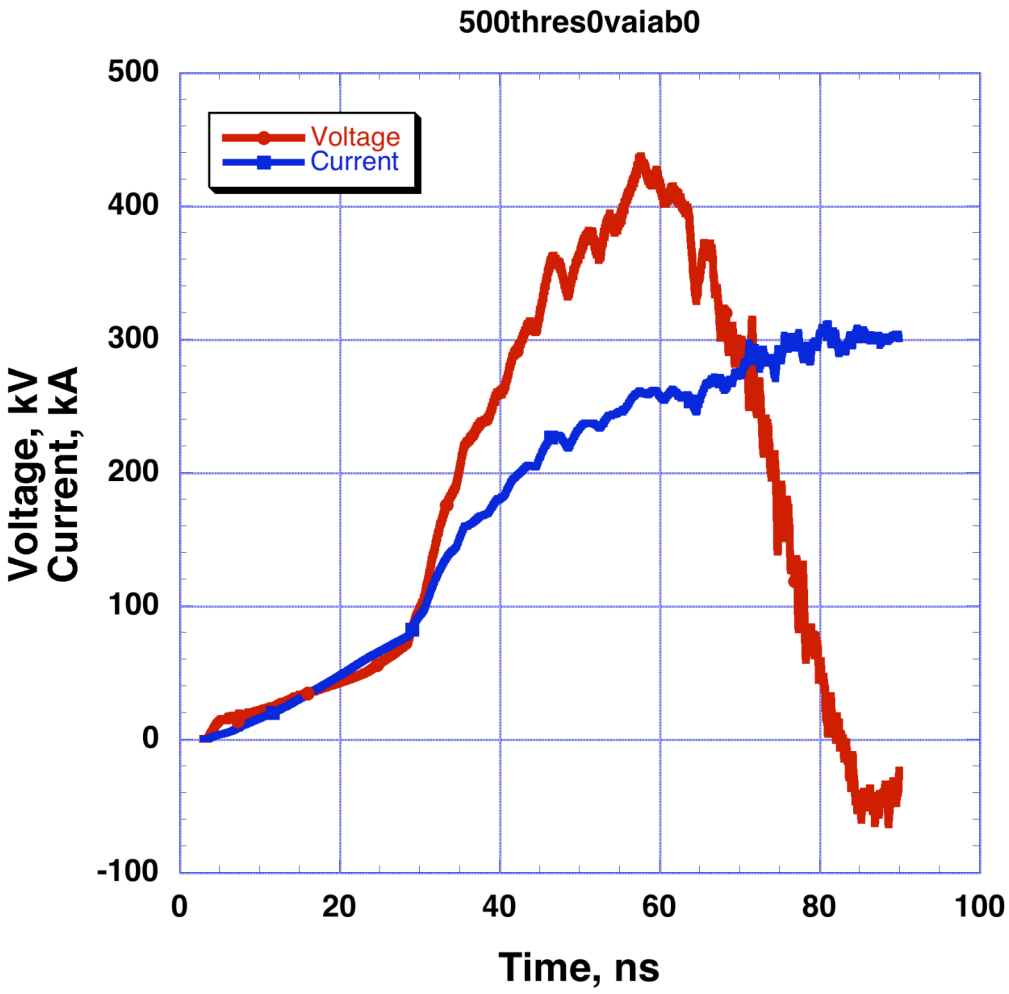

Figure 35. Simulation voltage and current at the outer edge of the MITL for the low voltage (experimental waveform) case.

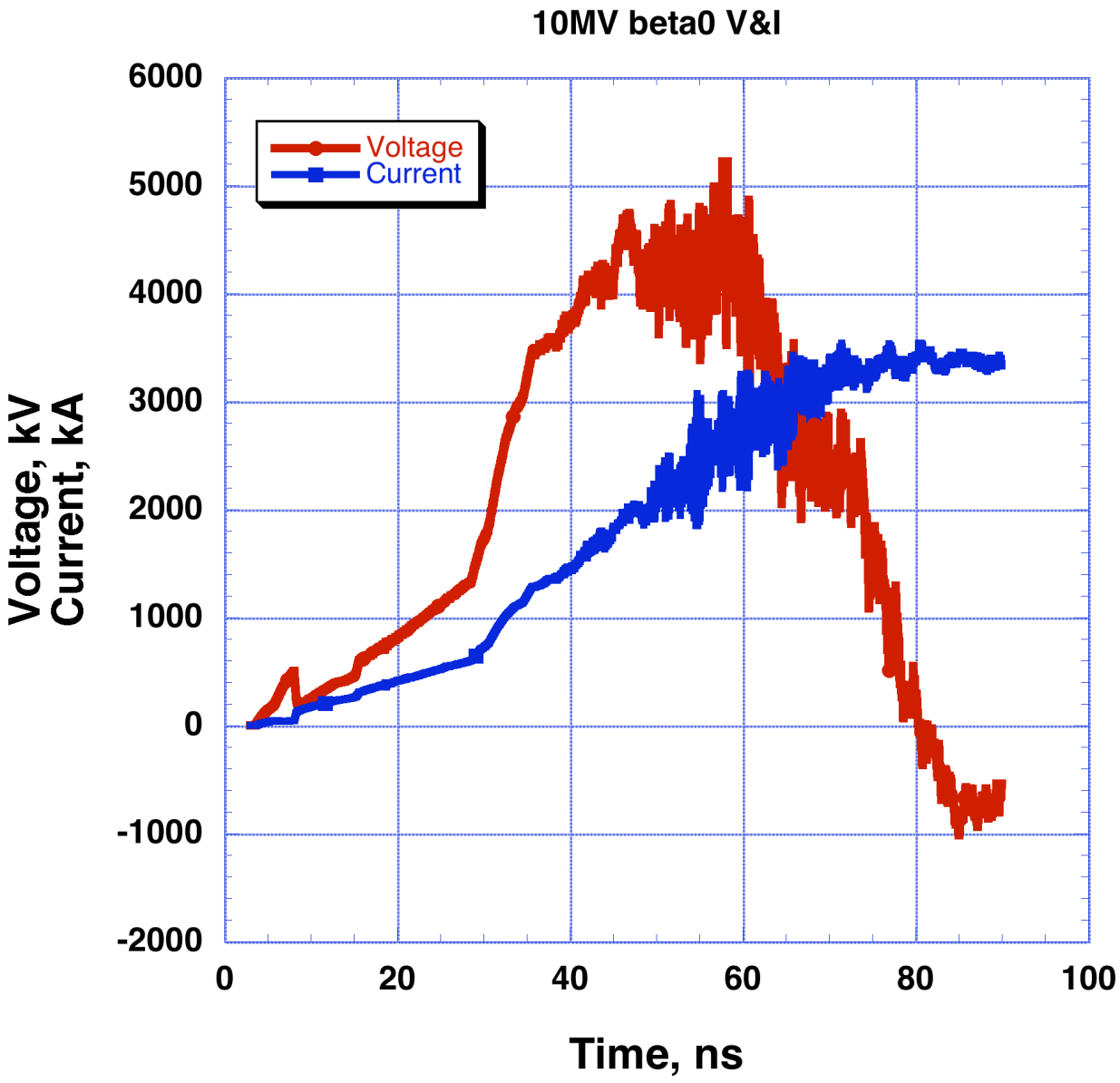

Figure 36. Simulation voltage and current at the outer edge of the MITL for the high voltage case. The oscillations on the waveform are physical electron instabilities and are observed in both experiments and simulations.

The space charge correction is much more significant for the lower voltage simulations. This is shown in Figure 37 and Figure 38. The space charge correction is [28]

$$V_{scc} = \frac{m_e c^2}{2e}\left[\frac{I_a^2}{I_c^2} - 1\right] \cong 255 \cdot 10^3 \left[\frac{I_a^2}{I_c^2} - 1\right] \tag{23}$$

where V_{scc} is the space charge correction, m_e is the electron rest mass, c is the speed of light, e is the electron charge, I_a is the anode current, and I_c is the cathode current. The space charge correction voltage is about the same for the two simulations at peak voltage (~200 kV) but that voltage is much less significant compared to the ~4 MV total voltage in the high voltage setup.

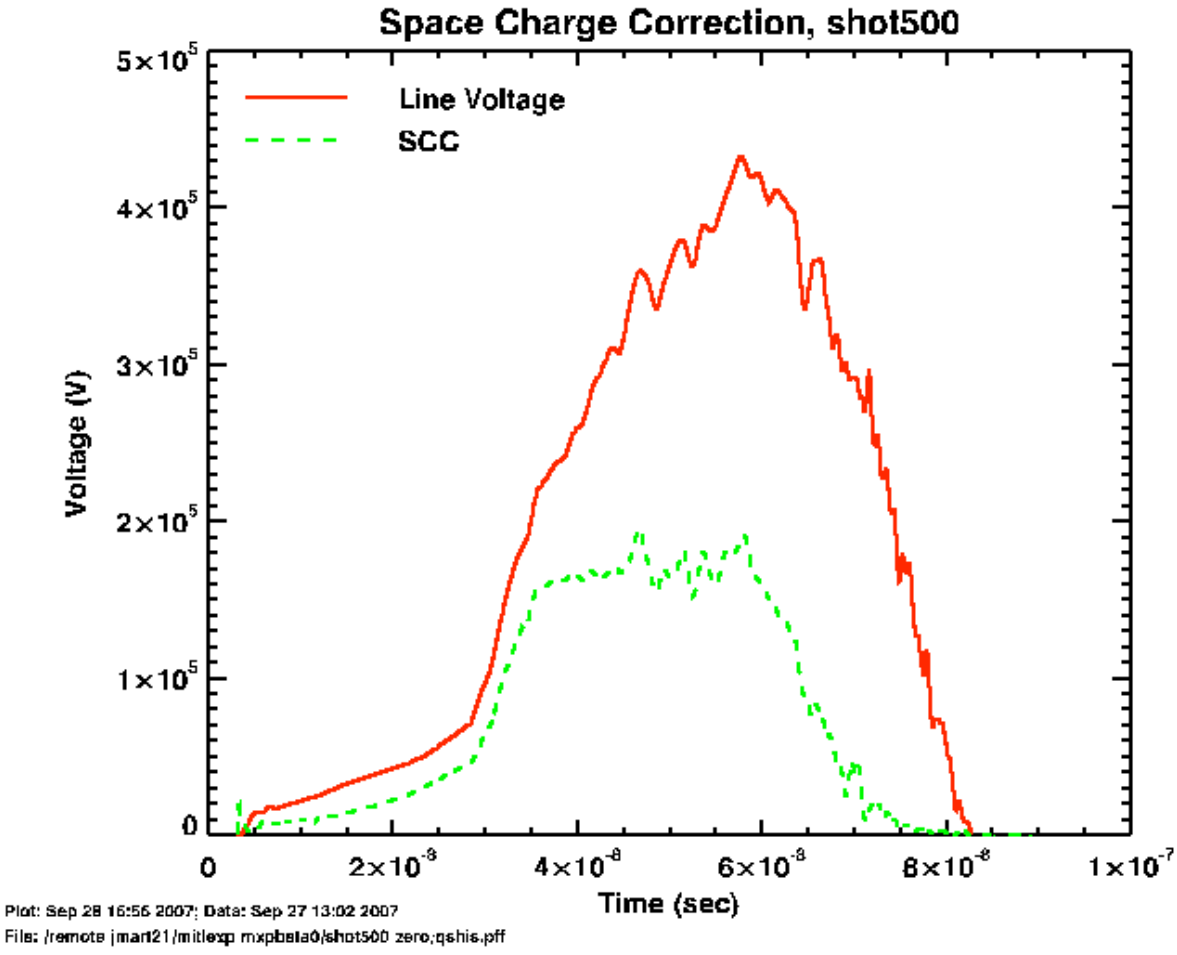

Figure 37. Total voltage and space charge correction for the lower voltage simulations.

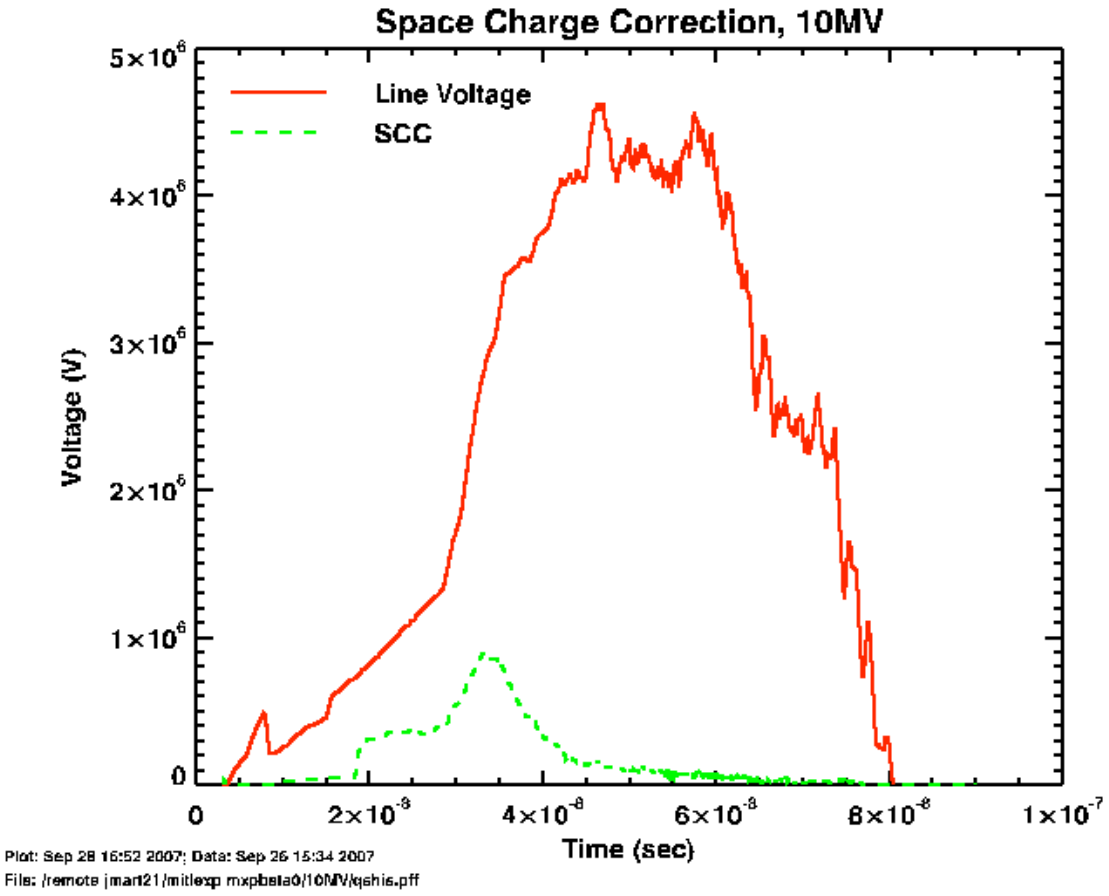

Figure 38. Total voltage and space charge correction for the high voltage simulation. The lower voltage simulation has a more significant space charge correction.

The space charge correction is a far smaller fraction of the total voltage on the high voltage simulations. This more closely fits the assumptions in the simple model, so it is useful to look at both cases. The charge density at a time near peak voltage is shown in Figure 40 for the high voltage simulation. Figure 39 shows the electron charge density at the time of peak voltage for the lower voltage simulation. Figure 40 shows the electron charge density at the time of peak voltage for the high voltage simulation. Note the charge density centroid shown in the Figures is much closer to the cathode in the higher voltage simulation.

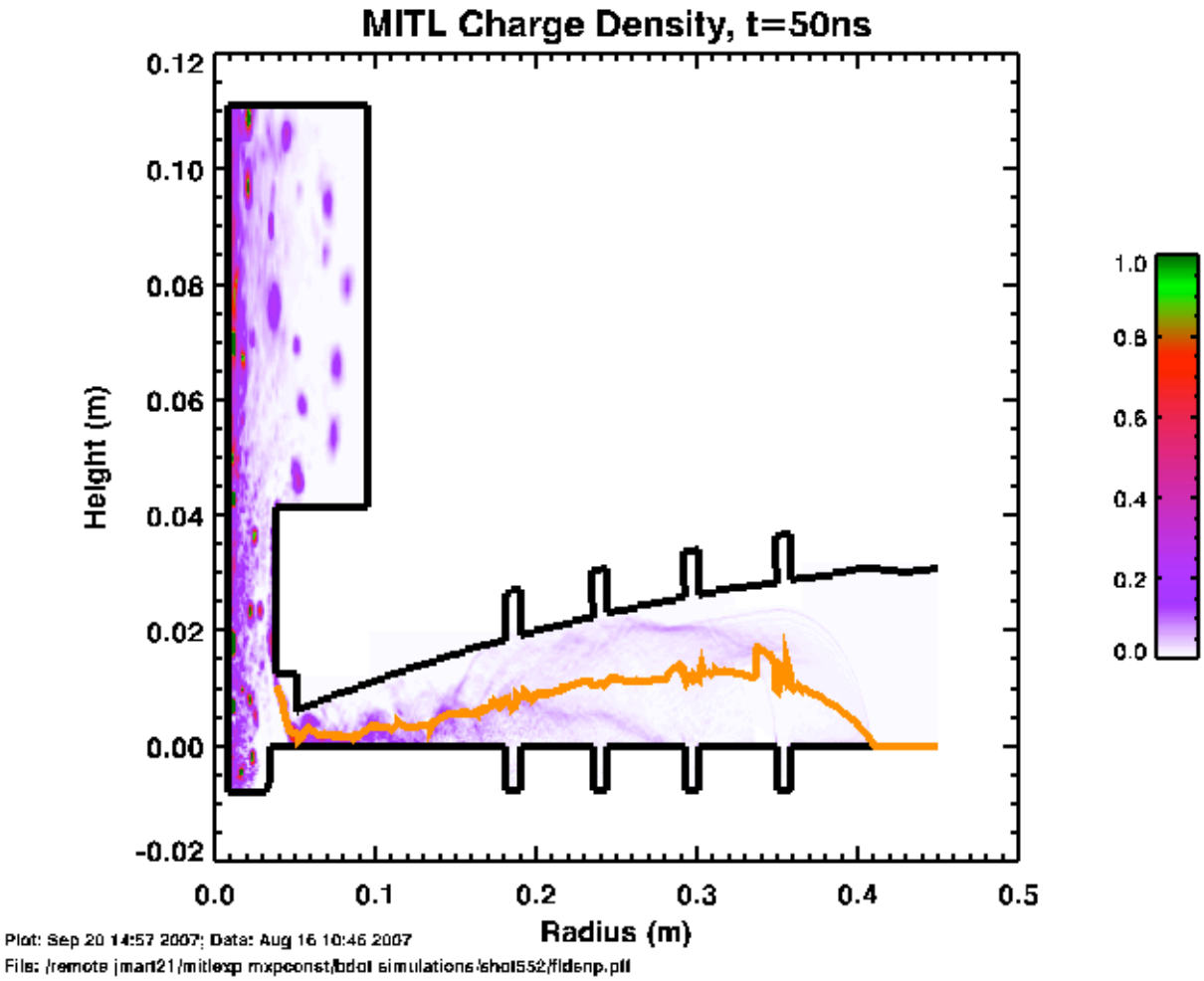

Figure 39. Electron charge density and the electron charge centroid of the lower voltage simulation, at the time of peak voltage. The geometry shown is the beta=3.7 setup.

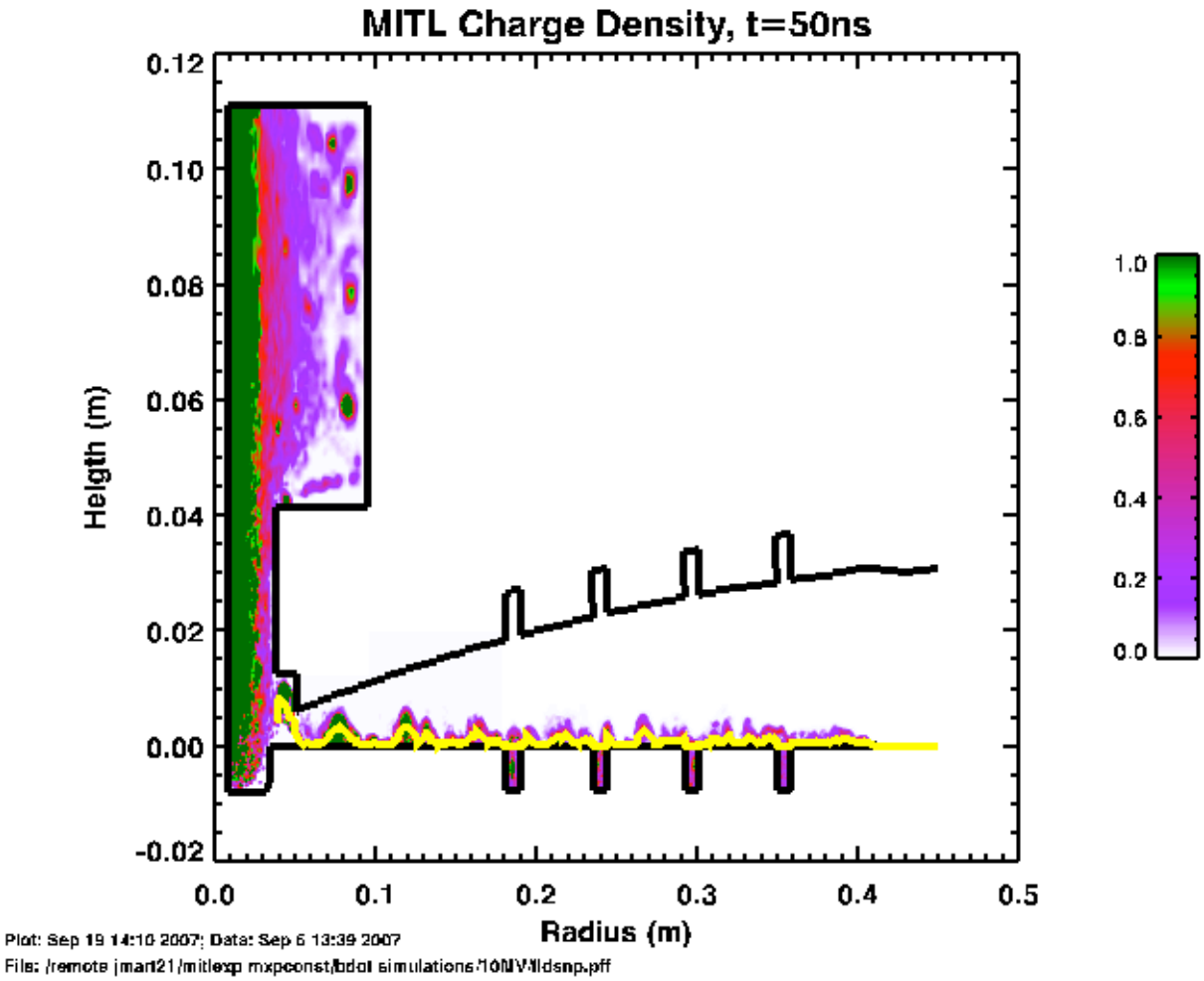

Figure 40. Charge density and electron charge centroid for the high voltage simulation, at the time of peak voltage. Note that the charge centroid is much closer to the cathode than in the 500 kV simulation. The geometry shown is the beta=3.7 setup.

The flow impedance is a measure of the position of the electron sheath. Electric flow impedance is a measure of the centroid of the electron charge density, and the magnetic flow impedance is a measure of the centroid of the electron current density [26, 27, 45, 46].

Electric and magnetic flow impedance

Figure 41 to Figure 44 show the effect of the electron emission threshold applied in the simulation. Shown in each Figure is the theoretical flow [28] calculated from the local voltage, gap, and electrode current. The theoretical model essentially assumes a zero threshold; the theoretical line is the same in all the Figures below.

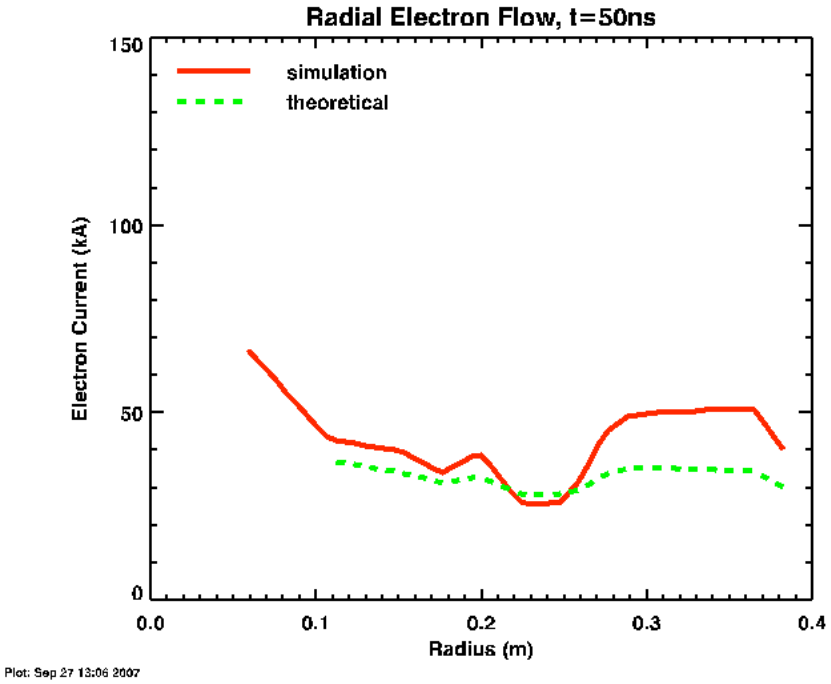

Figure 41. Electron flow versus radius for the low voltage simulation with a zero threshold for cathode electron emission.

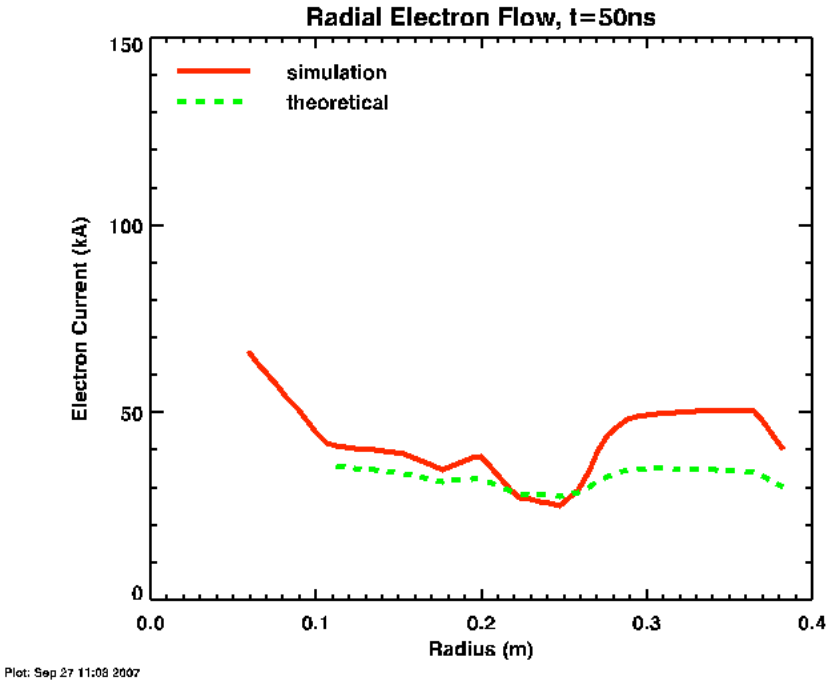

Figure 42. Electron flow versus radius for the low voltage simulation with a 50 kV/cm threshold for the cathode surface to begin freely emitting electrons.

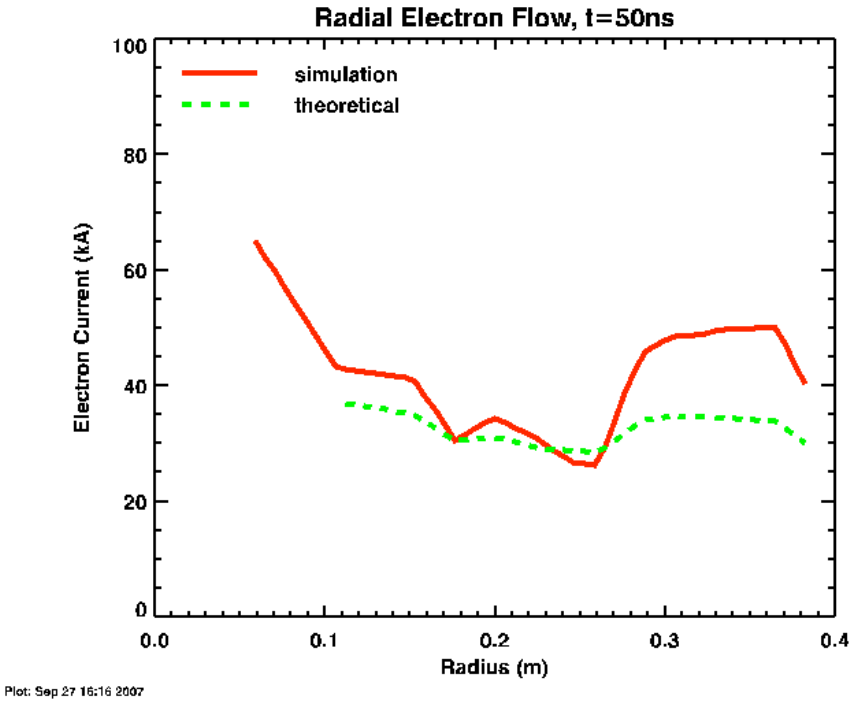

Figure 43. Electron flow versus radius for the low voltage simulation with a 100 kV/cm threshold for the cathode surface to begin freely emitting electrons.

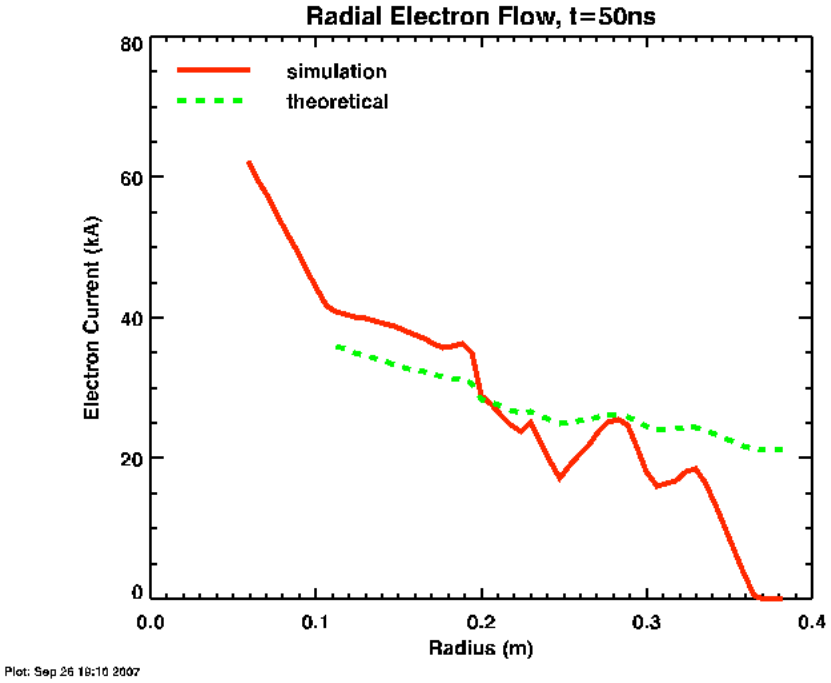

Figure 44. Electron flow versus radius for the low voltage simulation with a 200 kV/cm threshold for the cathode surface to begin freely emitting electrons. The large diameter region of the simulation is not emitting electrons because of the larger gaps and resulting lower field.

Figure 45 shows electric and magnetic flow impedance (charge and current centroid position [26]) for a low voltage simulation at time of peak voltage, for the constant flow geometry. Figure 46 shows electric and magnetic flow impedance (charge and current centroid position [26]) for a low voltage simulation at time of peak voltage, for the reducing (beta=1) flow geometry.

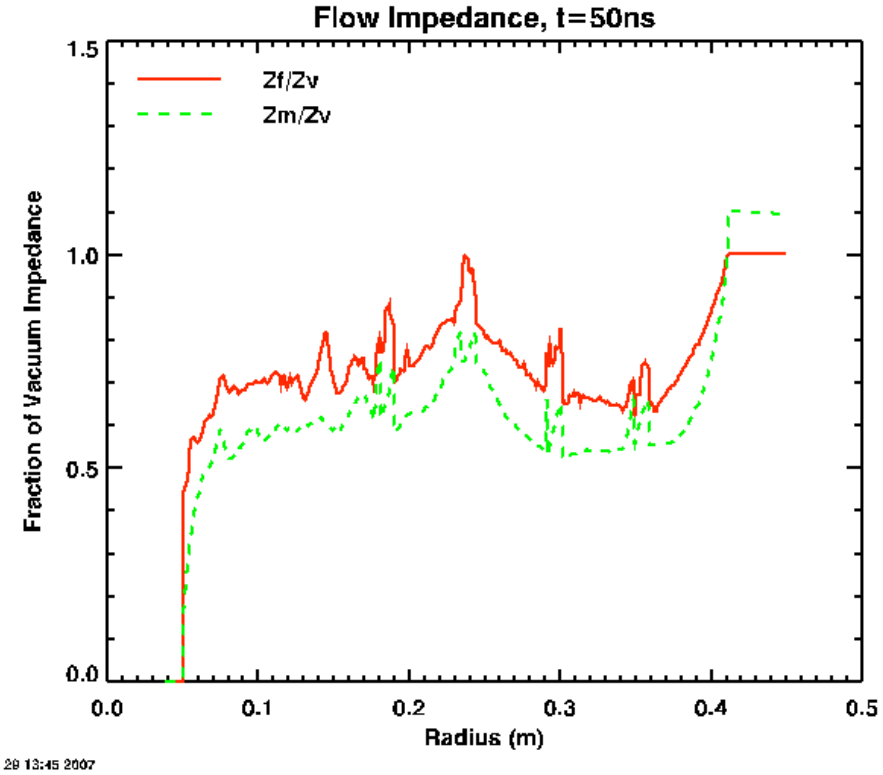

Figure 45. Electric (Z_f) and magnetic (Z_m) flow impedance as a fraction of vacuum impedance, for the constant flow (beta=0) geometry.

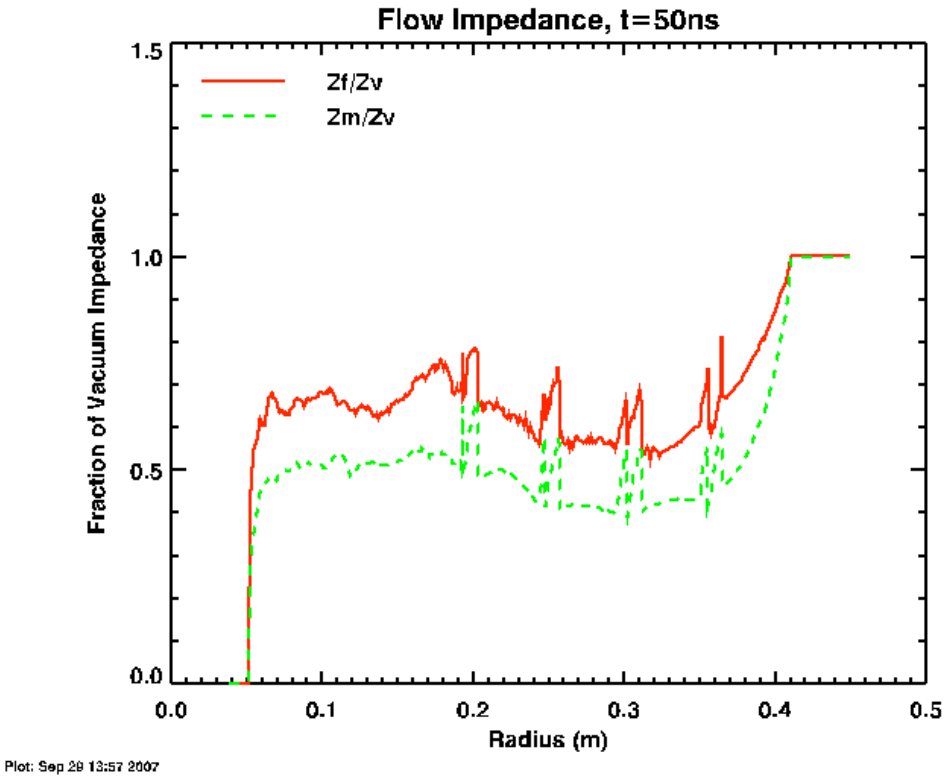

Figure 46. Electric (Z_f) and magnetic (Z_m) flow impedance as a fraction of vacuum impedance, for the reducing (beta=1) geometry.

Simulation results

The simulations show several important features.

The behavior of the electron flow in the simulations follows the local theoretical values. For this to happen when impedance is increasing in the power flow direction, the electrons must gain energy. In low-resolution numerical simulations, numerical heating is a significant source of (artificial) electron energy gain. However, in the high-resolution simulations described here numerical heating is less than the betatron acceleration rate. Retrapping of electron flow has been observed experimentally in varied systems [17, 21, 30]. If the electron flow becomes unstable, electron energy loss will rise dramatically [22, 40]. It was not known what 'programmed' rate of retrapping would be stable in this system. Clearly, large impedance increases in the power flow direction will cause the formation of electron vortices [10, 11, 47] because constant-gap radial transmission lines on Z clearly show ~1 GHz microwave formation while voltage is highest and for most of the voltage collapse. The purpose of the present work was to design, analytically, an impedance profile for a magnetically insulated transmission line that could be programmed with a specific expected rate of retrapping. This is a somewhat different approach to MITL design than was used when Z was designed [42, 48, 49]. For simplicity, the model used here does not include changing inductance, but in an efficient system, a large fraction of the energy is delivered before the inductance changes greatly [50]. The model used here does not consider gap closure. Within those constraints, the simple analytic model does a reasonable job of describing the behavior

observed in the simulations. The simple model might provide a reasonable starting point for more complicated considerations.

Simulations were run at ~500 kV and ~10 MV to study the effects of space charge which is more significant at lower voltage. Most large z-pinch drivers operate at voltages well over one megavolt. For example, the refurbished Z driver will have an insulator stack voltage of about 4.5 MV. The simulations designed to model the experiment suffered from large space charge effects and as seen above, effects of electron emission threshold [43, 51]. For that reason, we will look first to the higher voltage simulations of three different geometries with different 'programmed' retrapping rates. Figure 47 shows simulation results for three retrapping rates (the retrapping constant has units of inverse length): 0, 1/m, and 3.7/m. If the simple model applied exactly, the electron flow would follow:

$$I_e = I_{e:r\max} \exp\left(-\beta\left(r_{\max} - r\right)\right) \tag{24}$$

where I_e is the electron current at some radius, $I_{e:r\max}$ is the electron flow at the outer edge of the MITL, β is the retrapping rate, and r_0 is the radius at which the system transitions to constant gap (Figure 2). The simulations are time accurate, but the electron flow is averaged over a two-nanosecond window to reduce displayed fluctuations.

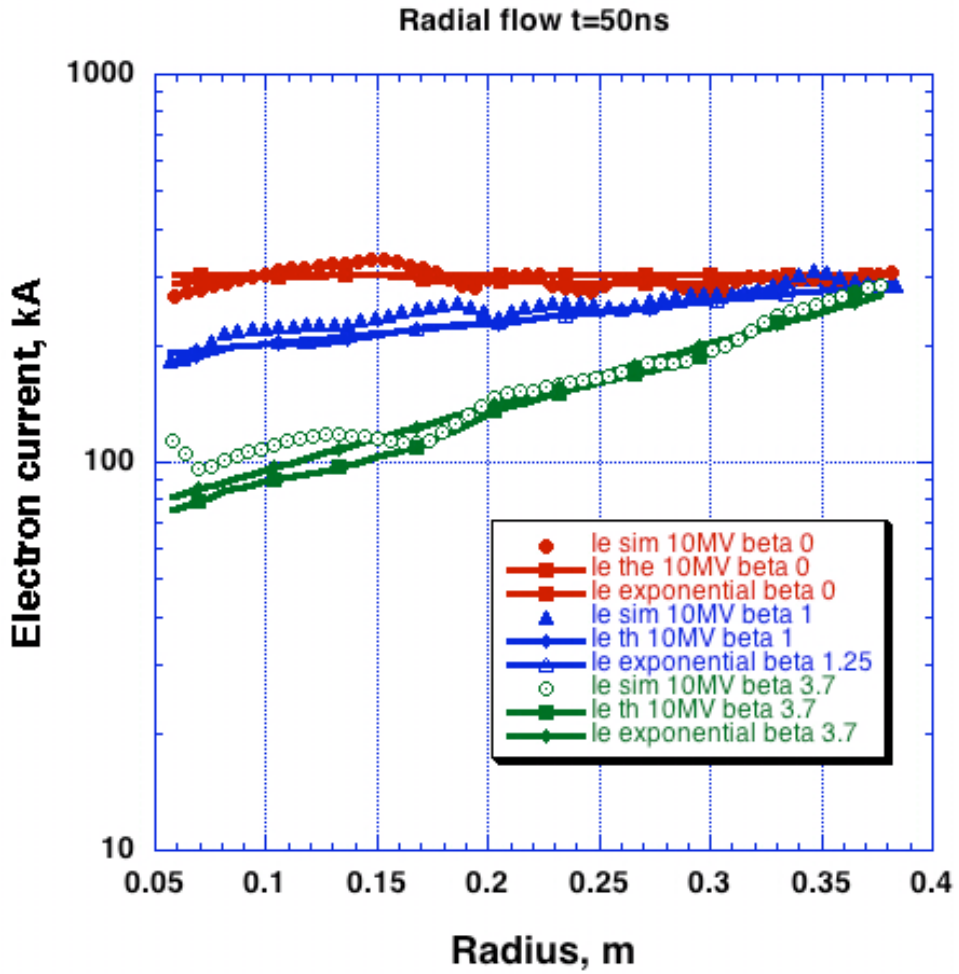

Figure 47. Simulation electron flow (high voltage simulation) for three programmed retrapping rates (0- red; 1- blue; 3.7- green). The simulation data are shown as unconnected symbols; the analytic model and simple exponential are shown as lines. The beta=0 should be constant electron flow, and the beta=1/m should e-fold every meter. The beta=3.7/meter should (and does) have the highest retrapping rate.

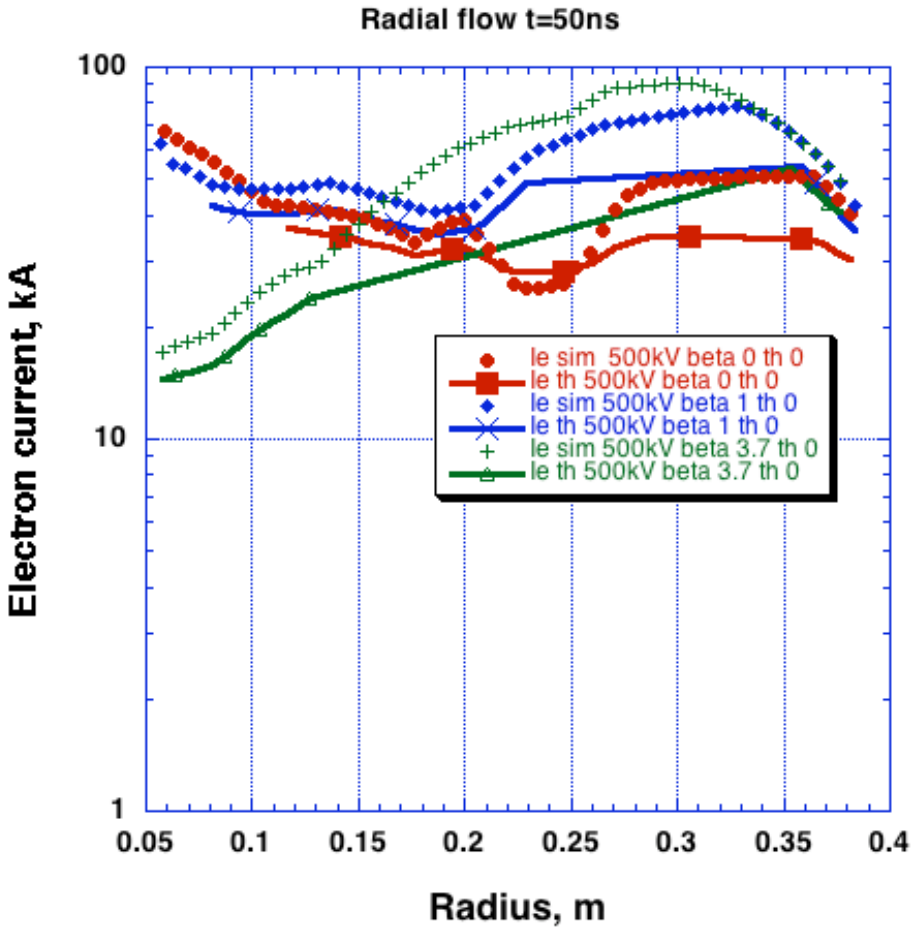

Figure 48. Simulations of the three different geometries at lower voltage (0- red; 1- blue; 3.7- green). This does not specifically meet the assumptions of the model because of the low voltage, and so variations are not surprising. Still, the highest retrapping parameter predicts lower flow at small radius.

The measured electron flow is lower than that predicted by the particle in cell simulations. Figure 49 and Figure 50 show both the measured and simulated electron flow for the constant flow and reducing flow geometries. The reducing flow geometry

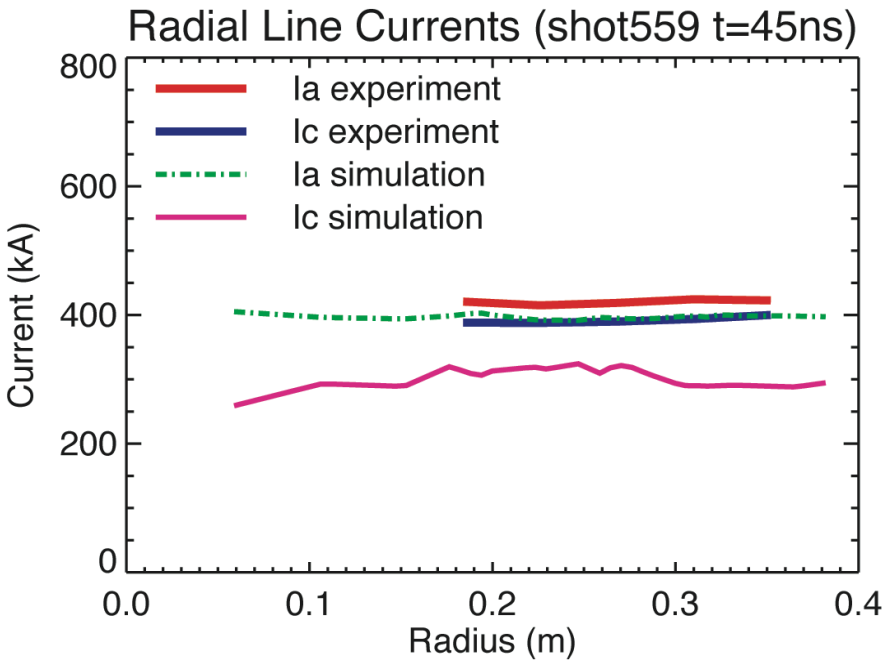

Figure 49. Measured and simulated anode and cathode currents at 45 ns for the constant-electron flow geometry.

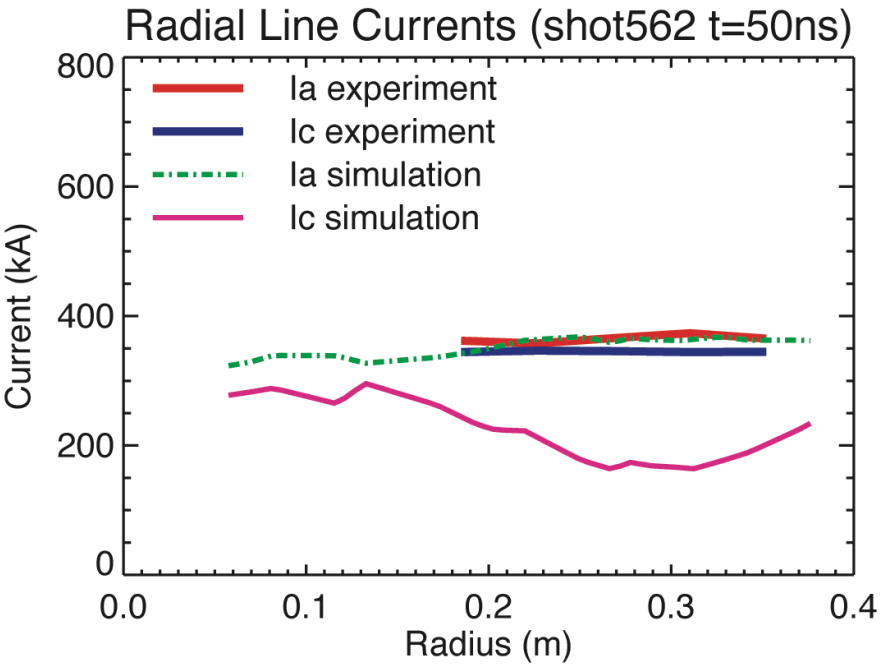

Figure 50. Measured and simulated anode and cathode currents for the reducing flow geometry. The simulated anode current matches the experimental value, but the simulated cathode current is lower than the experimentally measured value.

The benefit of lower electron flow at small radius is often cited to be less energy for anode plasma creation. The Quicksilver system allows calculation of anode temperature from electron energy deposition. Results of that calculation are shown in Figure 51 and Figure 52.

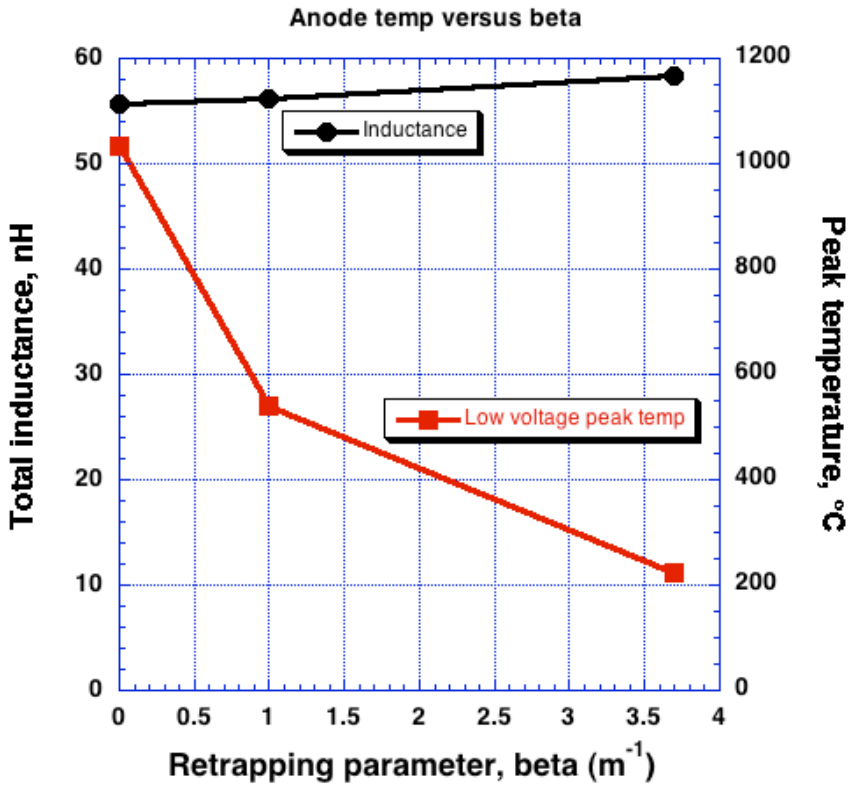

Figure 51. Calculated peak anode temperature for the low voltage Quicksilver simulations. The electron emission threshold is set to zero and the temperature data are taken at the end of the pulse. Also shown is the total inductance, including the 50 nH center can. Stainless steel is assumed.

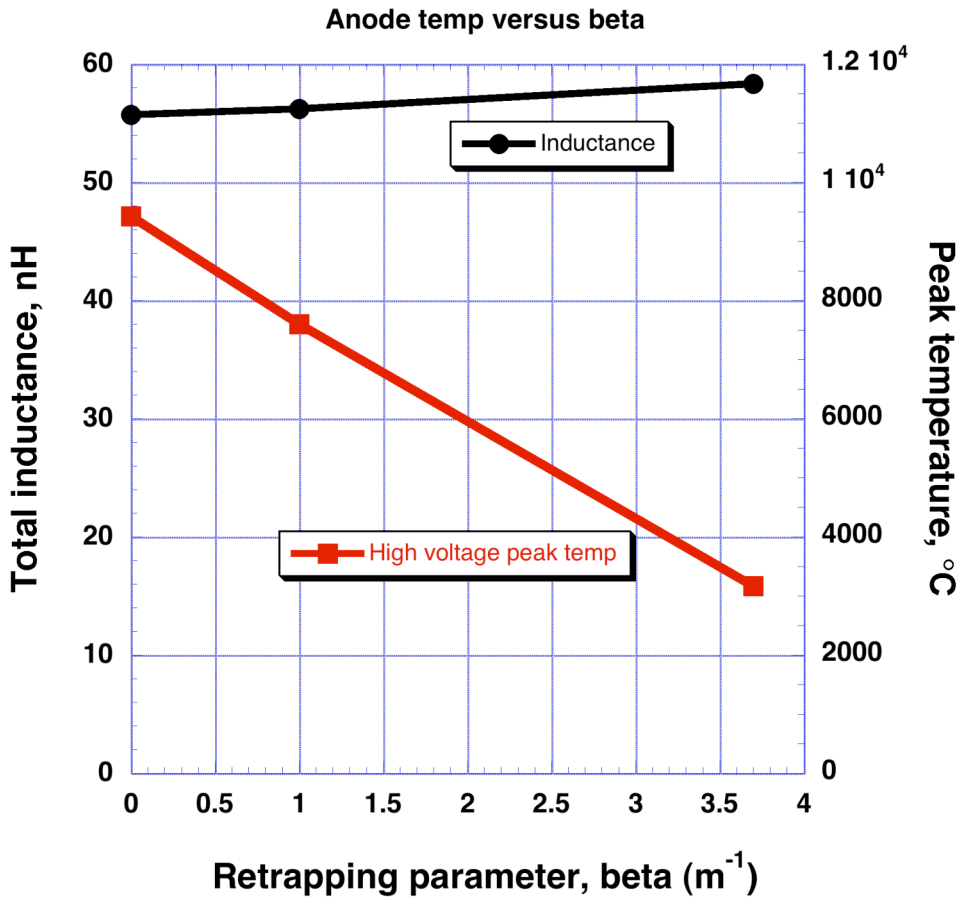

Figure 52. Calculated peak anode temperature for the high voltage Quicksilver simulations. The electron emission threshold is set to 200 kV/cm (which is low in this case) and the temperature data are taken at the end of the pulse. Also shown is the total inductance, including the 50 nH center can. Stainless steel is assumed.

The region of electron anode heating is shown in Figure 53 and Figure 54. The heating is confined to small radius. The higher voltage simulations shows heating at smaller radius. A temperature rise of 400 °C is assumed to be benign in most cases [39].

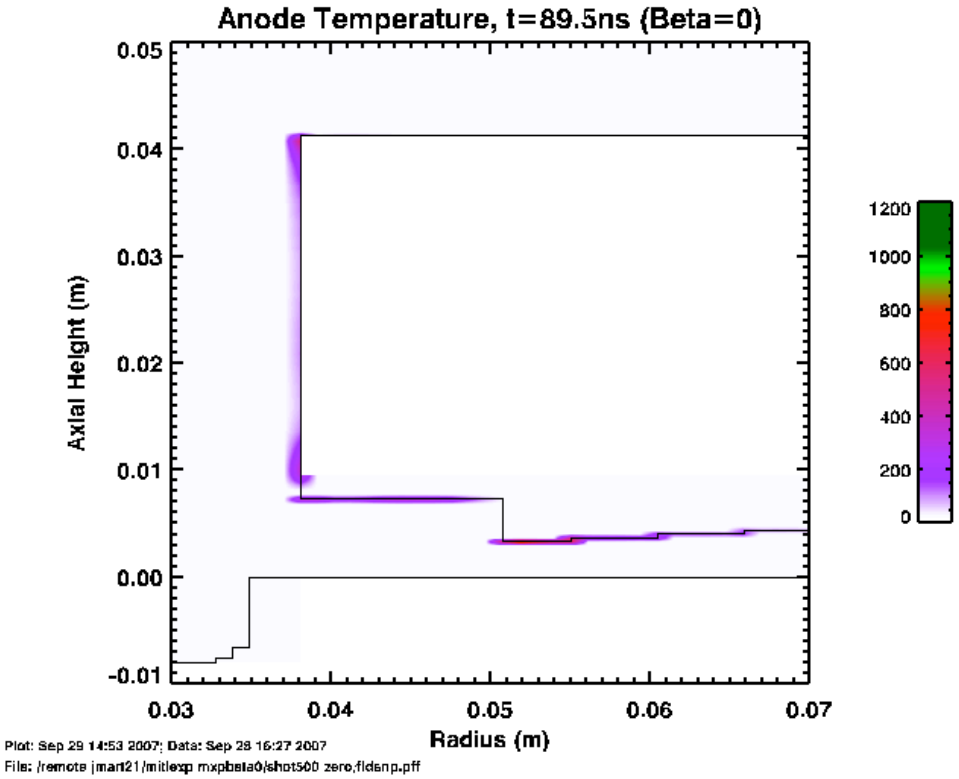

Figure 53. Anode heating results for beta=0 low voltage simulations. The area where significant heating occurs is shown in red.

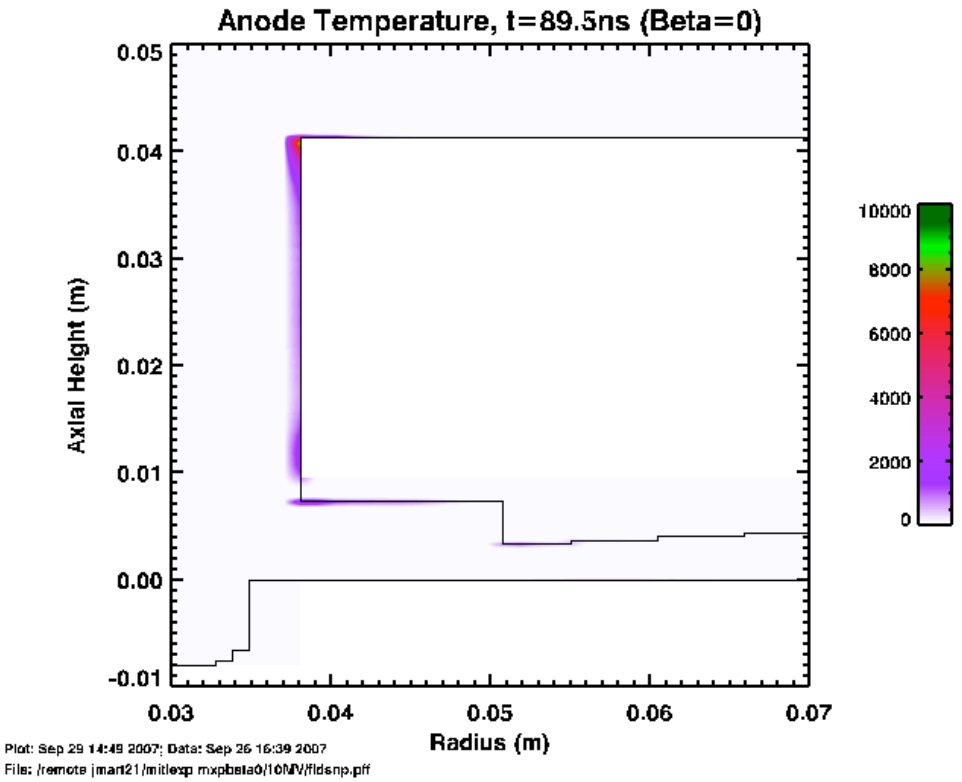

Figure 54. Anode heating results for beta=0 high voltage simulations. The area where heating occurs is shown.

A simulation region near a cathode groove is shown in Figure 55 and Figure 56. The perturbation to the magnetic field is small. It is likely that the groove fills with electrons on a fast time scale. If we assume the electrons flow in the $E \times B$ direction, then the electron filling will happen on the time scale that the magnetic field fills the groove. This is determined by the groove inductance and the impedance of the electron flow above the groove. This can be estimated from

$$\begin{aligned} V_g &= L_g \dot{I}_c \\ R &= \frac{V_g}{I_e} \\ \tau &= \frac{L_g}{R} \\ &= \frac{I_e}{\dot{I}_c} \end{aligned} \tag{25}$$

where L_g is the inductance of the groove, $\dot{I}_c$ is the time derivative of the MITL cathode current, V_g is the voltage across the mouth of the groove, and τ is the time constant for magnetic field to fill the groove. This time is about 2.7 ns for typical low voltage simulation and experimental conditions; the filling time is slightly longer (~4 ns) for the high voltage simulations. The simulations of the groove show the rotating electrons

('eddy') in the groove don't change the local magnetic field appreciably, thus a cathode current measurement in a groove can be accurate.

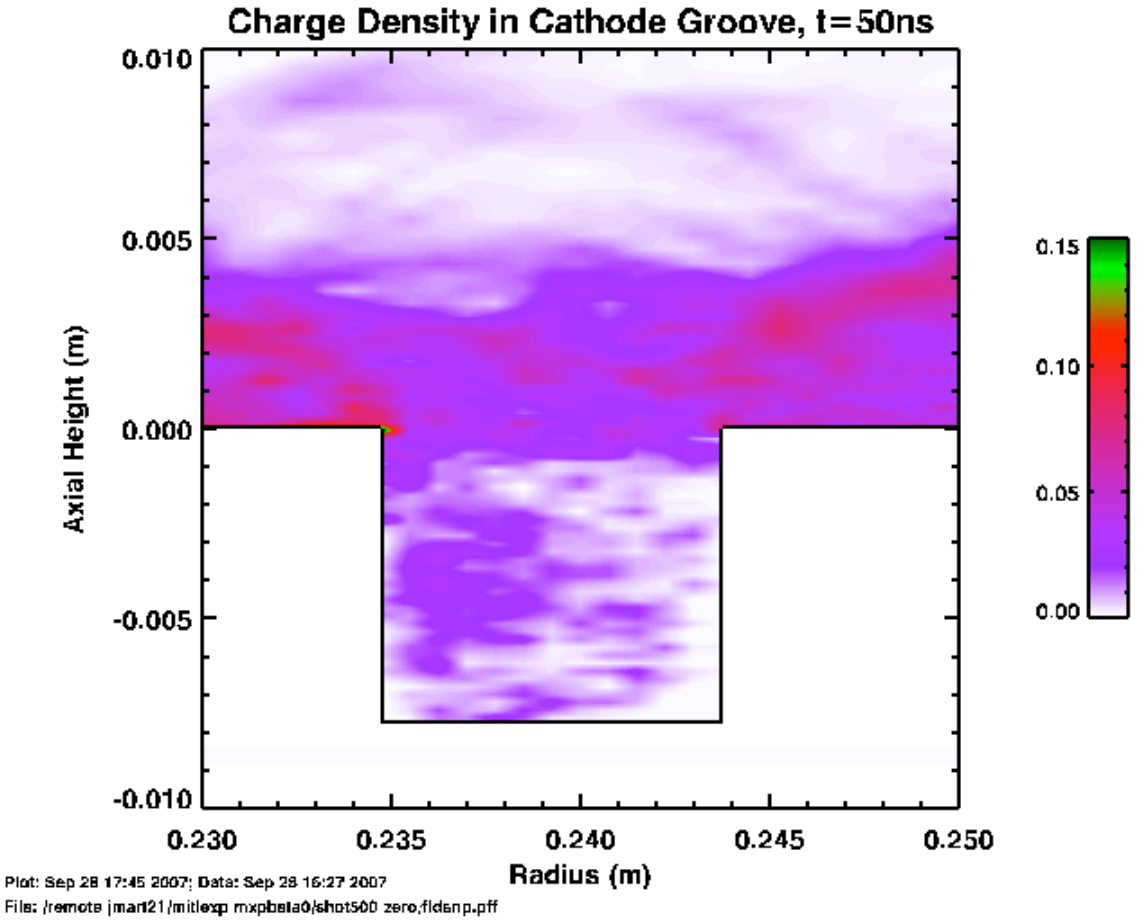

Figure 55. Charge density at the time of peak voltage (50 ns) for a 500 kV simulation with zero electron emission threshold. The groove has an electron density comparable to that near the cathode surface away from the grooves.

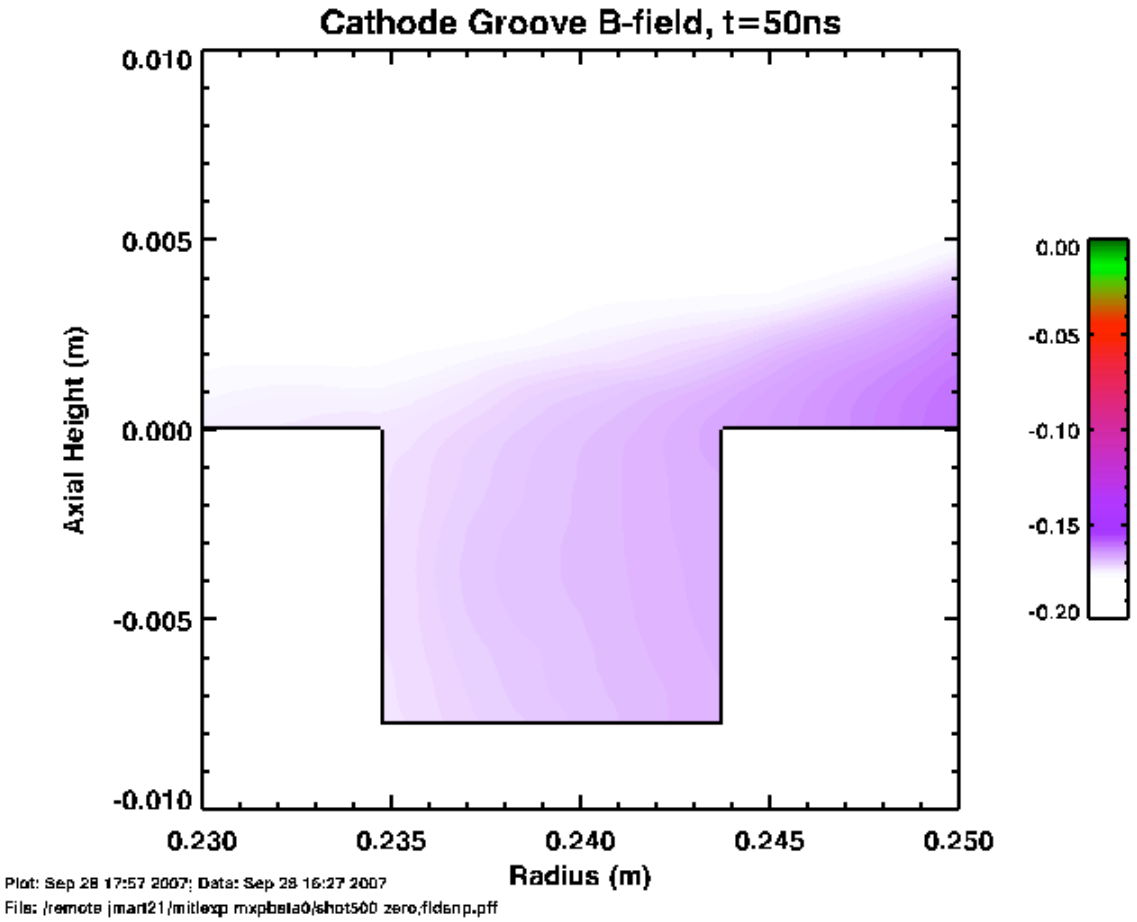

Figure 56. Magnetic field in a cathode groove at peak voltage (50 ns) in a 500 kV simulation with zero electron emission threshold. The rotating electrons in the groove do not alter the magnetic field significantly.

Conclusions

Simulations show that it is possible to tailor the impedance profile of a MITL to achieve a desired balance between inductance and electron flow at small radius. Comparison with high-resolution particle simulations shows at high voltage compared to the electron rest mass (much greater than 500 kV), a simple local pressure-balance model describes the MITL electron flow. Essentially, electron flow tends to operate at a value set by the local voltage, anode current, and local vacuum impedance. For smooth, but substantial, changes in local fractional electron flow up to $\frac{1}{I_e}\frac{\partial I_e}{\partial r}$ of 3.7 per meter, the flow is relatively stable and well approximated by the local pressure-balance equilibrium value. This simple model neglects gap closure. A tailored gap profile that reduces electron flow at small radius reduces the anode heating due to electron deposition. The parameter of fractional change in electron current per unit length is probably more useful for evaluating the limit of stable electron flow reduction than the change in vacuum impedance per unit length because vacuum impedance is not the only factor controlling electron flow.

The simulations also show that grooves in the cathode (comparable to the gap size) do not disrupt significantly the electron flow. The grooves quickly fill with electrons and become ignorable.

It is possible to measure electron flow directly by collecting electrons in a device that exploits the electron flow disruption of an abrupt impedance increasing transition.

The electron flow measured in the experiment is lower than that observed in simulations. This is due to a non-zero electric field at the cathode. The simulations maintain a particle density near the cathode at the value to cancel the applied electric field. This charge density results in the highest possible electron flow current. If electron emission is non-uniform, then the average cathode electric field is the same direction as the field at the anode. If the transmission line has excess electron charge (due to the rising current and slowing drift velocity with time and spatially in the direction towards the inductive load) that cannot return to the cathode then the electric field at the cathode will be reversed from the anode electric field. The measured electron flow current is about one-third of the electron flow current simulated by Quicksilver. This difference between simulation and experiment is significant and has not been observed in resistively terminated systems. [21, 30] The factor of three discrepancy is much more than can be attributed to experimental measurement error. The unique aspect of these experiments is that the load was purely inductive on these tests, and for that reason the electron energy gain is due to the rising magnetic field is significant. The experiments focused on times from the start of the pulse until peak current; during that time current is rising and voltage is falling, both tending to increase electron energy.

References

[1] F. Winterberg, "Magnetically insulated transformer for attaining ultrahigh voltages," *Rev. Sci. Instrum.*, vol. 41, pp. 1756-1763, 1970.

[2] J. M. Creedon, "Relativistic Brillouin flow in the high η/γ diode," *J. Appl. Phys.*, vol. 46, pp. 2946-2955, 1975.

[3] J. M. Creedon, "Magnetic cutoff in high-current diodes," *J. Appl. Phys.*, vol. 48, pp. 1070-1077, 1977.

[4] E. H. Hirsch, "The concept of magnetic insulation," *Rev. Sci. Instrum.*, vol. 42, pp. 1371-1372, 1971.

[5] A. W. Hull, "The effect of a uniform magnetic field on the motion of electrons between coaxial cylinders," *Phys. Rev.*, vol. 18, pp. 31-57, 1921.

[6] C. W. Mendel, Jr., D. B. Seidel, and S. E. Rosenthal, "A simple theory of magnetic insulation from basic physical considerations," *Laser and Particle Beams*, vol. 1, pp. 311-320, 1983.

[7] C. W. Mendel, Jr., D. B. Seidel, and S. A. Slutz, "A general theory of magnetically insulated electron flow," *Phys. Fluids*, vol. 26, pp. 3628-3635, 1983.

[8] F. Winterberg, "On the concept of magnetic insulation," *Rev. Sci. Instrum.*, vol. 43, pp. 814-815, 1972.

[9] K. D. Bergeron and J. W. Poukey, "Beam stability and current loss in magnetic insulation," *J. Appl. Phys.*, vol. 50, pp. 4996-5000, 1979.
[10] B. W. Church and R. N. Sudan, "A self-consistent quasistatic equilibrium for non-neutral diamagnetic electron vortices," *Phys. Plasmas*, vol. 2, pp. 1837-1845, 1995.
[11] B. W. Church and R. N. Sudan, "Nonlaminar multicomponent models for electron flow in positive polarity multigap accelerators," *Phys. Plasmas*, vol. 3, pp. 3809-3820, 1996.
[12] C. W. Mendel, Jr., J. A. Swegle, and D. B. Seidel, "Stability of magnetically insulated electron flow," *Phys. Rev. A*, vol. 32, pp. 1091-1097, 1985.
[13] J. Swegle and E. Ott, "Instability of the Brillouin-flow equilibrium in magnetically insulated structures," *Phys. Rev. Lett.*, vol. 46, pp. 929-932, 1981.
[14] L. E. Aranchuk, V. B. Babykin, A. S. Chernenko, and A. S. Chuvatin, "Passage of an intense electromagnetic pulse in a vacuum line with a plasma switch," *Sov. J. Plasma Phys.*, vol. 17, pp. 317-322, 1991.
[15] L. E. Aranchuk, E. I. Baranchikov, A. V. Gordeev, V. V. Zazhivikhin, V. D. Korolev, and V. P. Smirnov, "Magnetically self-insulated lines with ion leaks," *Sov. Phys. Tech. Phys.*, vol. 34, pp. 215, 1989.
[16] K. D. Bergeron, "Equivalent circuit approach to long magnetically insulated transmission line," *J. Appl. Phys.*, vol. 48, pp. 3065-3069, 1977.
[17] J. T. Crow and G. D. Peterson, "Recovery of electron sheath current in magnetically self-insulated transmission lines," *IEEE Trans. Plasma Sci.*, vol. PS-11, pp. 219-222, 1983.
[18] M. S. Di Capua and D. G. Pellinen, "Propagation of power pulses in magnetically insulated vacuum transmission lines," *J. Appl. Phys.*, vol. 50, pp. 3713-3720, 1979.
[19] M. S. Di Capua and T. S. Sullivan, "Magnetic insulation in short coaxial vacuum structures," presented at 2nd IEEE International Pulsed Power Conference, Lubbock, TX, 1979.
[20] J. Golden, T. J. Orzechowski, and G. Bekefi, "Magnetic insulation of an intense relativistic electron beam," *J. Appl. Phys.*, vol. 45, pp. 3211-3212, 1974.
[21] K. Hahn, J. Maenchen, S. Cordova, I. Molina, S. Portillo, D. Rovang*, et al.*, "Retrapping studies on RITS," presented at 14th IEEE International Pulsed Power Conference, Dallas, TX, 2003.
[22] T. P. Hughes, R. E. Clark, B. V. Oliver, T. D. Pointon, and W. A. Stygar, "Sheath-current retrapping in the Z MITLs," presented at 14th IEEE International Pulsed Power Conference, Dallas, TX, 2003.
[23] R. Kraft and M. W. McGeoch, "Experimental study of magnetic insulation," *Phys. Fluids*, vol. 30, pp. 1189-1200, 1986.
[24] C. W. Mendel, Jr., T. D. Pointon, M. E. Savage, and D. B. Seidel, "Losses at magnetic nulls in pulsed-power transmission line systems," *Phys. Plasma*, vol. 13, pp. 043105-1 - 043105-14, 2006.
[25] C. W. Mendel, Jr., J. P. Quintenz, S. E. Rosenthal, D. B. Seidel, R. Coats, and M. E. Savage, "Experiments on insulation of relativistic electron flows in oblique magnetic fields," *IEEE Trans. Plasma Sci.*, vol. 17, pp. 797-800, 1989.

[26] C. W. Mendel, Jr. and S. E. Rosenthal, "Modeling magnetically insulated devices using flow impedance," *Phys. Plasmas*, vol. 2, pp. 1332-1342, 1995.
[27] C. W. Mendel, Jr. and S. E. Rosenthal, "Dynamic modeling of magnetically insulated transmission line systems," *Phys. Plasmas*, vol. 3, pp. 4207-4219, 1996.
[28] P. A. Miller and J. C.W. Mendel, "Analytic model of Applied-*B* ion diode impedance behavior," *J. Appl. Phys.*, vol. 61, pp. 529-539, 1987.
[29] T. D. Pointon, W. A. Stygar, R. B. Spielman, H. C. Ives, and K. W. Struve, "Particle-in-cell simulations of electron flow in the post-hole convolute of the Z accelerator," *Phys. Plasmas*, vol. 8, pp. 4534-4544, 2001.
[30] S. Portillo, K. Hahn, J. Maenchen, I. Molina, S. Cordova, D. L. Johnson*, et al.*, "Initial experimental results of re-trapping studies on a large area diode on RITS-3," presented at 14th IEEE International Pulsed Power Conference, Dallas, TX, 2003.
[31] M. E. Savage, J. C. W. Mendel, T. W. Grasser, W. W. Simpson, and D. M. Zagar, "Time-resolved voltage measurements in terawatt magnetically insulated transmission lines," *Rev. Sci. Instrum.*, vol. 61, pp. 3812-3820, 1990.
[32] S. Shope, J. W. Poukey, K. D. Bergeron, D. H. McDaniel, A. J. Toepfer, and J. P. Vandevender, "Self-magnetic insulation in vacuum for coaxial geometry," *J. Appl. Phys.*, vol. 49, pp. 3675-3678, 1978.
[33] J. P. Vandevender, "Long self-magnetically insulated power transport experiments," *J. Appl. Phys.*, vol. 50, pp. 3928-3934, 1979.
[34] J. P. VanDevender, "Power flow for vacuum insulated inductive loads," presented at 3rd IEEE International Pulsed Power Conference, Albuquerque, NM, 1981.
[35] J. P. VanDevender and D. H. McDaniel, "Advanced power flow technologies for high current ICF accelerators," presented at 8th International Symposium on Discharges and Electrical Insulation in Vacuum, Albuquerque, NM, 1978.
[36] J. P. VanDevender, R. W. Stinnet, and R. J. Anderson, "Negative ion losses in magnetically insulated vacuum gaps," *Appl. Phys. Lett.*, vol. 38, pp. 229-231, 1981.
[37] P. C. Wheeler, "Inductive voltage divider," Lawrence Livermore National Laboratory UCID-20521, 1985.
[38] T. D. Pointon and M. E. Savage, "2-D PIC simulations of electron flow in the magnetically insulated transmission lines of Z and ZR," presented at 15th IEEE International Pulsed Power Conference, Monterey, CA, 2005.
[39] T. W. L. Sanford, J. A. Halbleib, J. W. Poukey, A. L. Pregenzer, R. C. Pate, C. E. Heath*, et al.*, "Measurement of electron energy deposition necessary to form an anode plasma in Ta, Ti, and C for coaxial bremsstrahlung diodes," *J. Appl. Phys.*, vol. 66, pp. 10-22, 1989.
[40] W. A. Stygar, T. C. Wagoner, H. C. Ives, P. A. Corcoran, M. E. Cuneo, J. W. Douglas*, et al.*, "Analytic model of a magnetically insulated transmission line with collisional flow electrons," *Phys. Rev. ST-AB*, vol. 9, pp. 090401, 2006.
[41] D. W. Kerst, "Acceleration of electrons by magnetic induction," *Phys. Rev.*, vol. 58, pp. 841, 1940.
[42] W. A. Stygar, R. B. Spielman, G. O. Allshouse, C. Deeney, D. R. Humphreys, H. C. Ives*, et al.*, "Design and performance of the Z magnetically-insulated

transmission lines," presented at 11th IEEE International Pulsed Power Conference, Baltimore, MD, 1997.

[43] G. E. Vogtlin and J. E. Vernazza, "Vacuum insulator failure measurements and improvement," presented at 7th IEEE Pulsed Power Conference, Monterey, Ca, 1989.

[44] J. P. Quintenz, D. B. Seidel, M. L. Kiefer, T. D. Pointon, R. S. Coats, S. E. Rosenthal*, et al.*, "Simulation Codes for Light-Ion Diode Modeling," *Laser and Particle Beams*, vol. 12, pp. 283-324, 1994.

[45] C. W. Mendel, Jr., S. E. Rosenthal, and D. B. Seidel, "Low-pressure relativistic electron flow," *Phys. Rev. A*, vol. 45, pp. 5854-5865, 1992.

[46] C. W. Mendel, Jr. and D. B. Seidel, "Flow impedance in a uniform magnetically insulated transmission line," *Physics of Plasmas*, vol. 6, pp. 4791-4793, 1999.

[47] A. L. Peratt and C. M. Snell, "Microwave generation from filamentation and vortex formation within magnetically confined electron beams," *Phys. Rev. Lett.*, vol. 54, pp. 1167-1170, 1985.

[48] P. A. Corcoran, J. W. Douglas, I. D. Smith, P. W. Spence, W. A. Stygar, K. W. Struve*, et al.*, "PBFA-Z vacuum section design using TLCODE simulations," presented at 11th IEEE International Pulsed Power Conference, Baltimore, MD, 1997.

[49] T. P. Hughes, R. E. Clark, B. V. Oliver, R. A. S. John, and W. A. Stygar, "Computational support for Z-machine," Mission Research Corporation, Albuquerque, NM June 2002.

[50] C. W. Mendel, Jr., "Conical Z-pinch gun," *J. Appl. Phys.*, vol. 42, pp. 5483-5491, 1971.

[51] D. Shiffler, M. Ruebush, M. Haworth, R. Umstattd, M. LaCour, K. Golby*, et al.*, "Carbon velvet field-emission cathode," *Rev. Sci. Instrum.*, vol. 73, pp. 4358-4362, 2002.

Appendix: Integrator calibration

Passive RC integrator calibration

In most cases, particularly for fast pulses, passive hardware integration is the most accurate way to record signals from derivative-responding monitors. This is because a hardware integrator will always get the correct final answer; with numerical integration missed features due to inadequate sample rate (aliasing) affect the rest of the waveform record.

This section describes our procedures for calibrating (determining the time constant) and droop-correcting passive integrators. The integrator time constant directly affects the monitor gauge factor, and the droop removal algorithms used.

Introduction

There are two types of passive integrators in broad use in pulsed-power data acquisition: the so-called "1 megohm" integrator uses the integrator near the high-impedance scope input (high input impedance compared to the cable impedance). The "50 ohm" integrator operates into 50 ohms, and so can be placed far from the digitizer. The only real differences are that 1 megohm integrators achieve the same time constant with less capacitance, and 50 ohm integrators have a rising input impedance for times approaching the time constant. In general then, 50-ohm units are best suited to fast signals, and 1-megohm units are better for slow signals. We will discuss both below.

The 1 Megohm integrator

Figure 57 shows the schematic for a 1-megohm integrator.

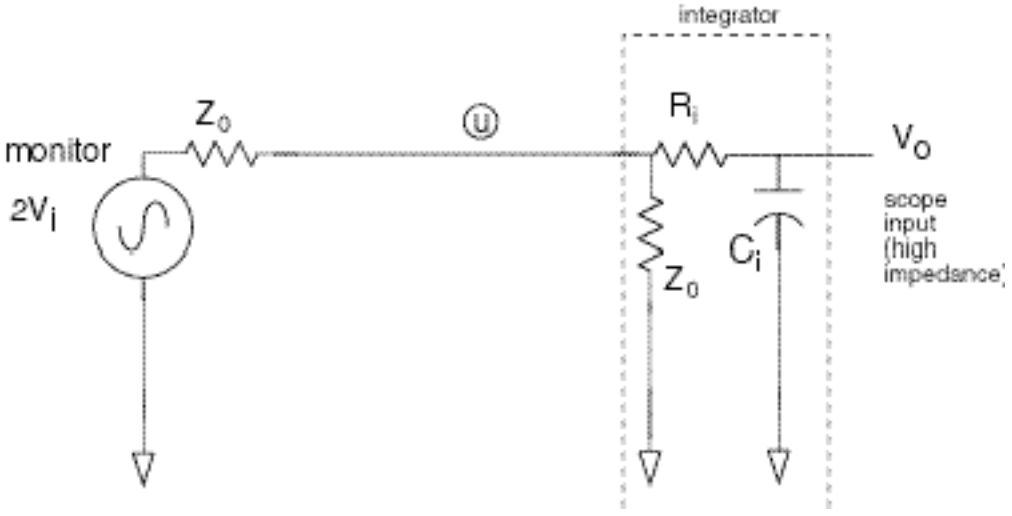

Figure 57. An integrator for use directly into a high-impedance digitizer.

The monitor (e.g., B-dot sensor) and cable is modeled by the voltage source (V_i) and the impedance Z_0 of the cable. The circuit equations are:

$$\frac{2V_i - u}{Z_0} = \frac{u}{Z_0} + \frac{u - V_0}{R_i} \tag{26}$$

and

$$u = R_i C \dot{V}_o + V_o, \tag{27}$$

where u is the voltage at the intermediate node, V_o is the output voltage recorded at the digitizer, R_i is the integrator resistor, and C_i is the integrator capacitor.

This circuit can be solved to give

$$\int V_i dt = V_o \left[C_i \left(R_i + \frac{Z_0}{2} \right) \right] + \int V_o dt \,. \tag{28}$$

For a system with the integrator time constant $\tau = C_i \left(R_i + \frac{Z_0}{2} \right)$ applied to the gauge factor G, the droop correction is $\frac{G}{\tau} \int V_o dt$. Thus, for a scaled signal $S(t)$, the droop-corrected data are

$$S_{corrected} = S(t) + \frac{1}{\tau} \int_{t_{start}}^{t} S(t') dt' \,. \tag{29}$$

To be useful, an integrator must be calibrated. Using a fast pulse for calibration allows quantifying the accuracy of the integrator as well as determining its time constant. Recording a signal that can be accurately recorded by the digitizer both before and after integration is a simple technique for determining the time constant.

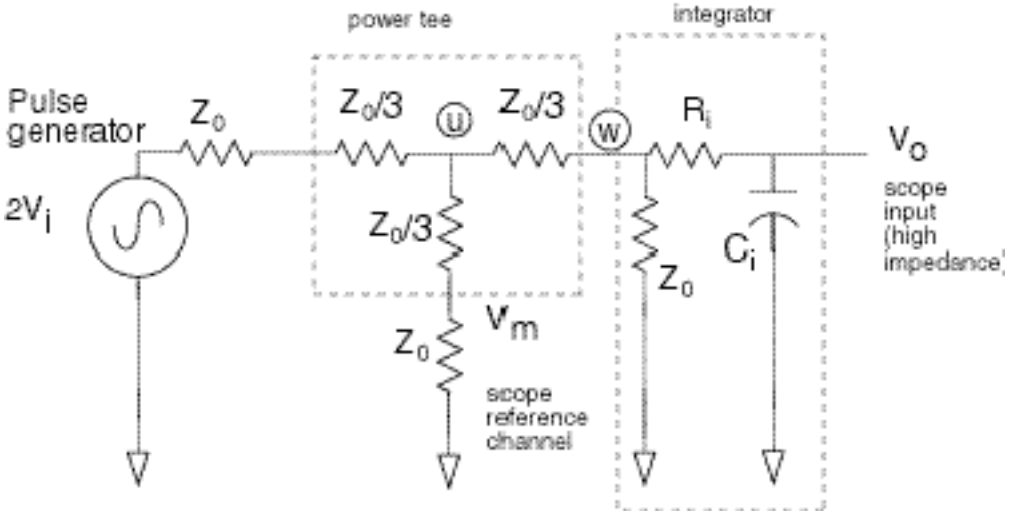

Figure 58. Calibration setup for 1-megohm integrators.

The circuit shown in Figure 58 can be analyzed with simple circuit equations.

$$\frac{2V_i - u}{Z_0 + \frac{Z_0}{3}} = \frac{u}{Z_0 + \frac{Z_0}{3}} + \frac{u - w}{\frac{Z_0}{3}} \tag{30}$$

$$\frac{u - w}{\frac{Z_0}{3}} = \frac{w}{Z_0} + \frac{w - V_o}{R_i} \tag{31}$$

$$\frac{w - V_o}{R_i} = C_i \dot{V}_o \tag{32}$$

$$V_m = \frac{3u}{4} \tag{33}$$

w is the voltage at the integrator input. These equations can be solved exactly to yield the integrator time constant as a function of V_m and V_o. This is:

$$\frac{\int_{t_{start}}^{t} V_m dt' - \int_{t_{start}}^{t} V_o dt'}{V_o} = \left(R + \frac{Z_0}{4} \right) C_i . \tag{34}$$

As is often the case with real data, the best means of evaluating this numerically is to compare the numerator to the denominator, or directly perform a least-squares fit. We will show later how this is applied. The observant reader will notice that the time constants differ slightly ($C_i\left(R_i + \frac{Z_0}{2} \right)$ in the droop correction calculations and $C_i\left(R_i + \frac{Z_0}{4} \right)$ in the calibration calculations). Since R_i must be much greater than Z_0 to maintain a proper termination, in general this difference can be ignored.

50 ohm integrators

The other common type of integrator is the 50-ohm unit. This integrator operates into 50 ohms, so the integrator does not need to be at the digitizer. Fast digitizers typically do not have a high impedance option, so this type of integrator must be used that case. The input impedance of this type integrator reaches $2Z_0$ at times much greater than the integrator time constant. For this reason, the monitor impedance should be matched to the cable, or equivalently, the cable double transit time should be greater than the recording window.

Figure 59 shows the schematic for a 50-ohm integrator.

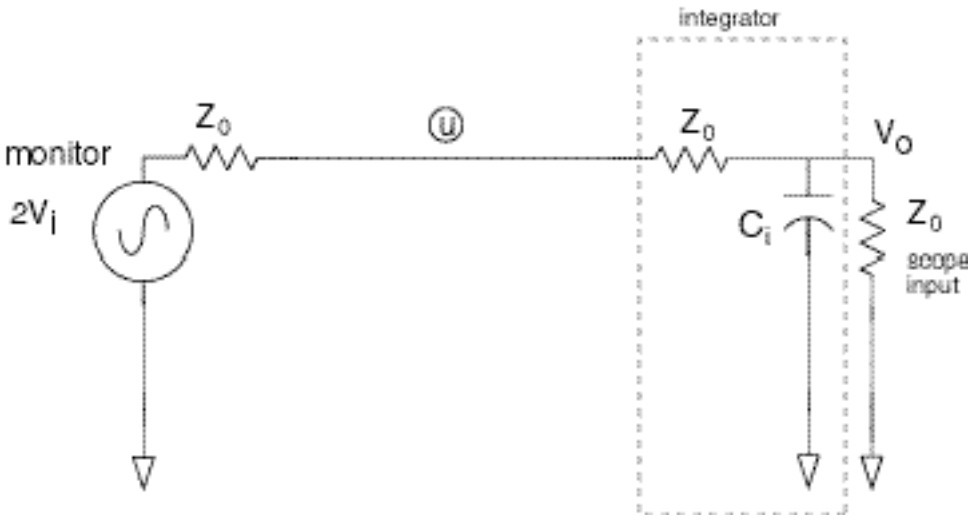

Figure 59. An integrator for 50-ohm digitizers.

The circuit of Figure 59 can also be analyzed easily. The equation is:

$$\frac{2V_i - V_o}{2Z_0} = \dot{V}_o C_i + \frac{V_o}{Z_0} \tag{35}$$

Solving for the integral of the detector voltage gives

$$\int V_i dt = V_o[C_i Z_0] + \frac{3}{2}\int V_o dt\,. \tag{36}$$

With the integrator calibration applied to the gauge factor, the droop correction is

$$S_{corrected} = S(t) + \frac{3}{2\tau}\int_{t_{start}}^{t} S(t')dt', \tag{37}$$

where

$$\tau = Z_0 C_i\,.$$

The 50-ohm integrator must also be calibrated. The manner of the calibration is the same as the 1-megohm integrator. Figure 60 shows the setup for calibrating 50-ohm integrators.

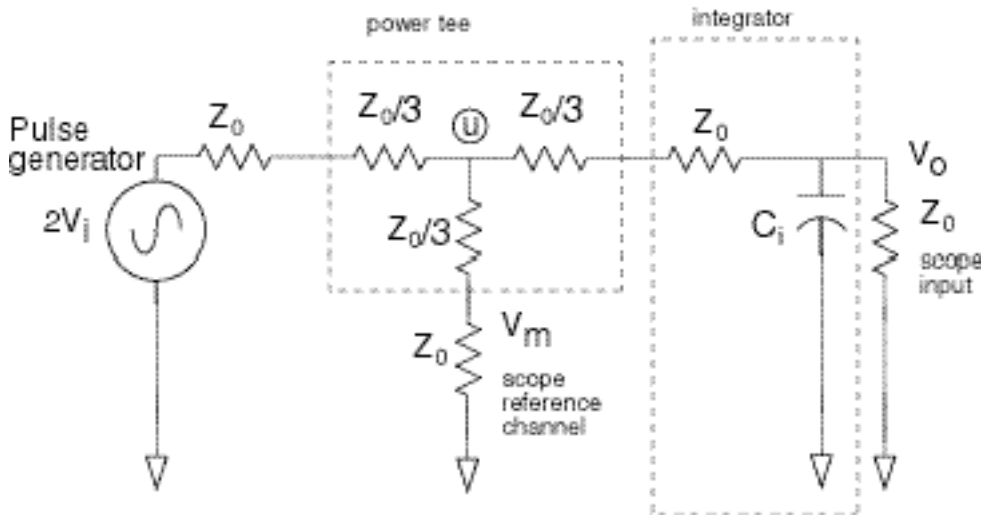

Figure 60. Calibration setup for 50-ohm integrators.

The analysis of this circuit is also straightforward.

$$\frac{2V_i - u}{\frac{4Z_0}{3}} = \frac{u}{\frac{4Z_0}{3}} + \frac{u - V_o}{\frac{4Z_0}{3}} \tag{38}$$

$$\frac{u - V_o}{\frac{4Z_0}{3}} = \frac{V_o}{Z_0} + C_i \dot{V}_o \tag{39}$$

$$V_m = \frac{3u}{4} \tag{40}$$

These equations can be solved exactly to yield the integrator time constant as a function of V_m and V_o. This is:

$$\frac{\int_{t_{start}}^{t} V_m dt' - \frac{7}{4}\int_{t_{start}}^{t} V_o dt'}{V_o} = C_i Z_0 . \tag{41}$$

Comparing equations (34) and (41), one can see the similarity. We can write the general calibration equation as

$$\frac{\int_{t_{start}}^{t} V_m dt' - k\int_{t_{start}}^{t} V_o dt'}{V_o} = \tau , \tag{42}$$

where k is 1 for the 1 megohm integrator, $7/4$ for the 50 ohm integrator, and τ is the integrator time constant used in the gauge factor and the droop correction function.

Application of the calibration formulas

As mentioned before, the time constant can be evaluated by direct evaluation of (42), or an iterative waveform comparison, or a direct least squares fit. Iterative waveform comparison deals best with possible time shifts between the signals. What we have done is to use an iterative routine to find the time shift between the signals, and then use a least squares fit equation.

After determining the time shift between the numerator and denominator, the numerator is shifted by this time value. The data arrays are then truncated to the same number of points. The following equations are evaluated:

$$\tau = \frac{\left\langle \left(\int V_o \right)^2 \right\rangle \langle V_o V_m \rangle - \left\langle V_o \int V_o \right\rangle \left\langle V_m \int V_o \right\rangle}{\left\langle V_o^2 \right\rangle \left\langle \left(\int V_o \right)^2 \right\rangle - \left\langle V_o \int V_o \right\rangle^2}, \tag{43}$$

and

$$k = \frac{\left\langle V_o^2 \right\rangle \left\langle V_m \int V_o \right\rangle - \left\langle V_o \int V_o \right\rangle \langle V_m V_o \rangle}{\left\langle V_o^2 \right\rangle \left\langle \left(\int V_o \right)^2 \right\rangle - \left\langle V_o \int V_o \right\rangle^2}, \tag{44}$$

where $\langle x \rangle$ is the mean value of the array x. Since the value of k is known from the integrator type, we use the value of k to estimate the accuracy of the calculation.

Figure 61 shows an example calibration of a Titan 1 megohm (nominal 2 μs) integrator.

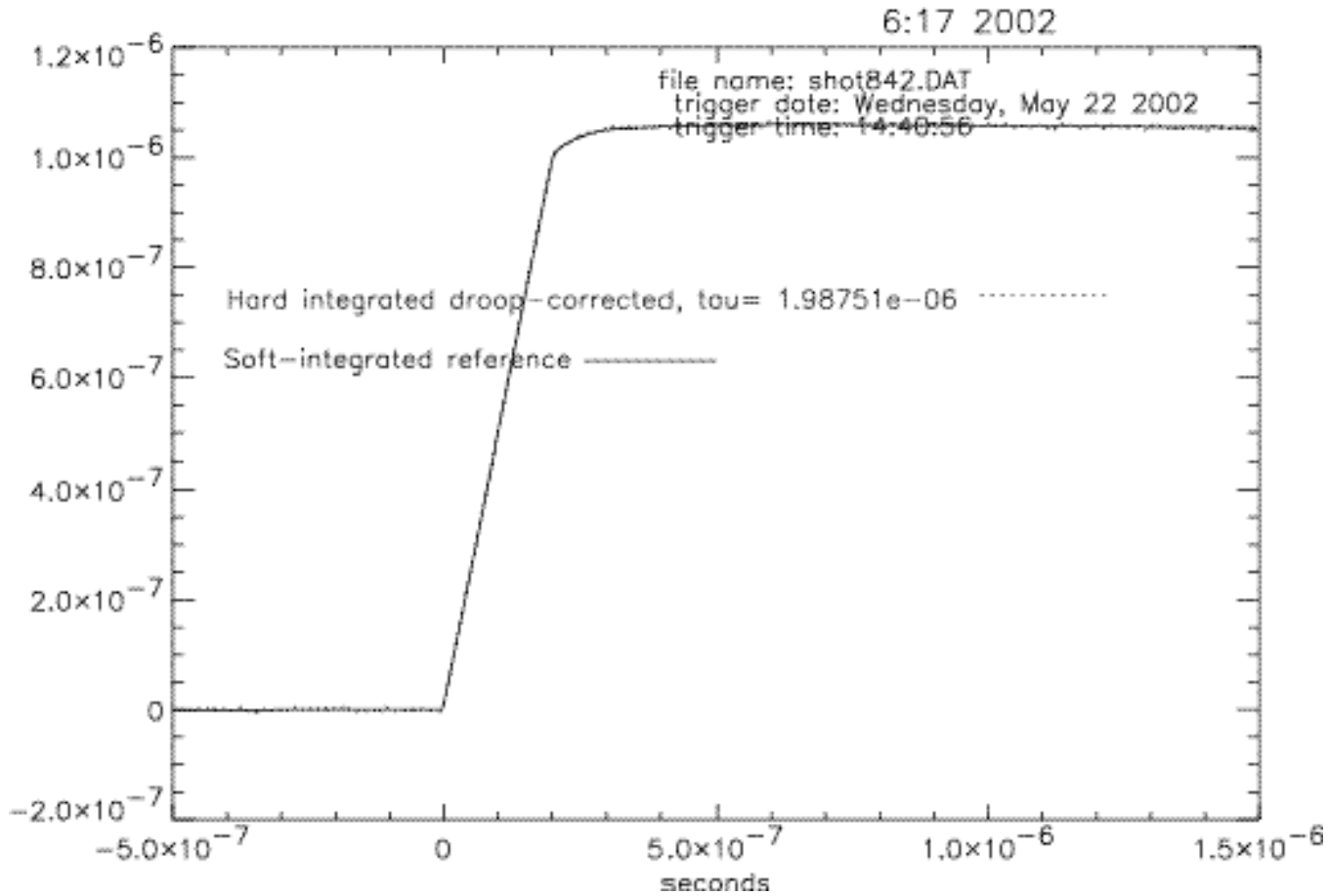

Notice: Time-shifting data by: 2.595e-09 seconds
Time constant is: 1.988e-06 seconds, B is: 0.981567
B is expected to be 1.00000 from the circuit, so you have a -1.84327 percent error level

Figure 61. Calibration results from a Titan 1 megohm integrator. This is an overlay of the numerically integrated signal and the scaled, droop-corrected integrator output. The input pulse is 5 volts from a Picosecond Pulse Labs pulser; data acquired on a Tektronix TDS684C.

Figure 62 shows calibration results on a 50-ohm integrator. This unit has a nominal 48 nF capacitance built from a large number of surface-mount capacitors. Notice in Figure 62 that the signals have a slope to the waveforms later in the pulse. This is due to the rising input impedance of the low-impedance integrator late in the pulse. In this calibration setup, the signal source (Picosecond Labs pulser) was not time-isolated from the integrator.

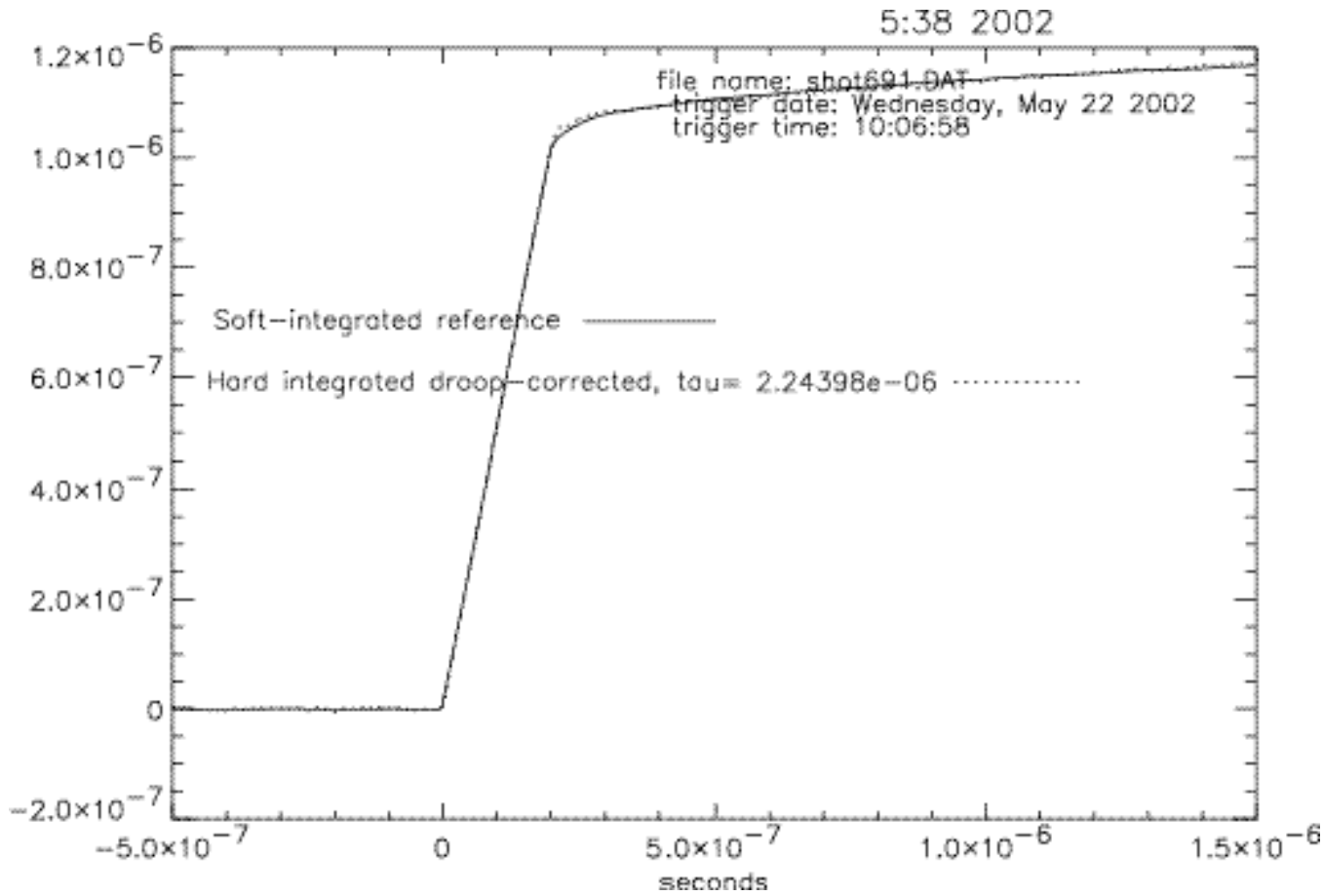

Notice: Time-shifting data by: -3.719e-10 seconds
Time constant is: 2.244e-06 seconds, B is: 1.77217
B is expected to be 1.75000 from the circuit, so you have a 1.26690 percent error level

Figure 62. Calibration results from a North Star 50 Ω integrator, nominal 2.4 μs.

Distribution:

15	MS 1194	M. Savage, 1671
1	MS 0899	Technical Library, 9536 (electronic copy)
1	MS 0123	D. Chavez, LDRD Office, 1011 (electronic copy)

Sandia National Laboratories